Author/s:
Li, Shuo

Title:
Study on air-sea CO2 gas exchange with wave breaking

Date:
2020

Persistent Link:
https://hdl.handle.net/11343/254281

Study on Air-sea CO_2 Gas Exchange with Wave Breaking

by
Shuo Li
https://orcid.org/0000-0002-9425-1040

Submitted in fulfilment of the requirements for the degree of

Doctor of Philosophy

Department of Infrastructure Engineering
THE UNIVERSITY OF MELBOURNE

Abstract

Atmospheric CO_2 is accumulating in recent decades due to excessive anthropogenic activities such as fossil fuel combustion, which intensifies global warming and affects the balance of carbon cycle. With more CO_2 in the air, ocean which acts as one of the largest carbon reservoirs absorbs about 26% of the human emissions of CO_2 to the atmosphere. The increased ocean inventory of anthropogenic carbon has caused the acidification of ocean water, making it critical to assess the CO_2 gas transfer process at air-sea interface. CO_2 gas transfer velocity (K_{CO_2}) is the main subject in the estimation of gas flux.

To date, K_{CO_2} is traditionally parameterized with wind speed, but it is the waves which produce the turbulence and bubbles that enhance the CO_2 intake. In our work, the new parameterization of $K_{CO_2}$with wave parameters is proposed through laboratory experiments, validated by field observation and applied to the estimation of the air-sea CO_2 flux over global ocean.

To investigate the direct relationship between CO_2 gas transfer and waves, laboratory experiments are conducted in a wind-wave flume. Three kind of waves are forced in the flume: monochromatic waves generated by a wavemaker, mechanically-generated monochromatic waves with superimposed wind forcing, and pure wind waves with 10-meter wind speed ranging from 4.5 m/s to 15.5 m/s. The wave parameters are found to be well correlated with K_{CO_2} while wind speed alone can not adequately describe K_{CO_2}. To reconcile the data sets, non-dimensional empirical formulae are established in which K_{CO_2} is expressed as a function of wave parameters as the dominant term and an enhancement factor to account for additional influence of the wind.

The parameterization is further validated by using field campaign data from different locations of open ocean and improved including considering the importance of bubble-mediated gas transfer at sea. The verified formula is able to collapse the results of both laboratory and field with reduced uncertainties.

The net air-sea CO_2 flux of global ocean is evaluated in a 33-year period from 1985 to 2017 by using our gas transfer parameterization. The results are in high agreement with previous studies, which is another evidence of the validity of the parameterization. A general increasing trend of global ocean net uptake of CO_2 is observed. The CO_2 flux in period 2017-2100 is also projected by using different CMIP6 forecast of future scenarios.

Preface

This thesis mainly comprises three parts of work during my PhD study on the air-sea CO_2 gas exchange under conditions of wave breaking.

The first study about laboratory experiments (chapter 4) was conducted in the University of Melbourne and then First Institute of Oceanography (FIO) in China. The latter experiment was performed in collaboration with Prof. QiaoFangli in FIO. The study was supported by the DISI Australia-China Centre through Grant ACSRF48199 and by the U.S. Office of Naval Research Grant N00014-17-1-3021. Prof. Qiao was jointly supported by the National Natural Science Foundation of China under grants 41821004 and the International cooperation project of the China-Australia Research Centre for Maritime Engineering of Ministry of Science and Technology, China under grant 2016YFE0101400.

The second study (chapter 5) was conceived on the basis of field observation data. Three field campaign data were collected and provided by Physical Sciences Division of NOAA Earth Systems Research Laboratory. Another field observation data was provided by Dr. Robyn Schofield at University of Melbourne from a joined field campaign by Commonwealth Scientific and Industrial Research Organization (CSIRO), Bureau of Meteorology (BOM) and the University of Tasmania (UTAS).

The third study (chapter 6) was planned based on the product of global ocean CO_2 partial pressure distribution provided by Dr. Steve D. Jones. The CMIP6 model data for future projections of air-sea CO_2 flux was offered by Dr.SongZhenya from FIO.

The rest of the thesis (chapter 1, 2, 3, 7) detailed the motivation, theory and methodology for this study.

Acknowledgment

I would like to show my respect to the Traditional Custodians of the Land, of Elders past and present, on which the University of Melbourne is landed, and where I enjoyed my PhD study. I also wish to acknowledge the Melbourne Research Scholarship which funded this PhD study.

In the past three years, I enjoyed the life and work in Melbourne. So many people here have inspired me both professionally and personally. First, I would like express my sincere gratitude to my supervisor Professor Alexander V. Babanin for the continuous support and professional guidance, for his patience, inspiration, encouragement when I was struggling in my project. His support made me enjoy the fun of research and accomplish the objectives of PhD study.

I also wish to thank the other members in my thesis committee, Prof. Ian Rober Young and A/Prof. Alessandro Toffoli, for their insightful comments and discussions. They helped me to extend my knowledge in the work and to learn how to communicate the research.

I would like to thank Dr. DaiDejun, JiangShumin, LiChao, Dr. Xinming from First Institute of Oceanography, who hosted me and helped me to go through the laboratory experiment. A special thanks is given to Dr. LiuQingxiang in our ocean engineering group for all the interesting discussions and his support. I also would like to thank the other colleagues for the precious time we spent together and the support during my study here. I want to thank my friends in Australia and back in China, their stories enriched my life and make the days more beautiful.

I dedicate this thesis and all the outcomes to my family, for their invaluable support in the past years. Every phone call made me motivated and kept me doing better.

Contents

List of Figures

List of Tables

Chapter 1
Introduction

The greenhouse gas carbon dioxide (CO_2) has been increasing since industrial revolution due to excessive anthropogenic activities and fossil fuel combustion. According to the "Keeling curve" measured at Hawaii island, the annual mean atmospheric CO_2 concentration increases from 315 ppm in 1958 to 405 ppm in 2017. The accumulation of CO_2 in the air is considered as one of the important environmental factors to boost global warming. Therefore, accurate evaluation of anthropogenic emissions and global carbon cycle has been of intensive scientific interest in recent years. Oceans which are dynamically exchanging CO_2 with atmosphere may act as sources or sinks. Overall, the ocean absorbs about 25%-48% of the total anthropogenic emissions (Sabine et al., 2004; Canadell et al., 2007; Doney et al., 2009). The estimation of ocean CO_2 uptake is still biased by the uncertainty of parameterization of gas transfer velocity. In spite of bulk researches on this subject, our perception of the gas transfer processes remains to be enhanced. CO_2 gas transfer velocity (K_{CO_2}) is traditionally parameterized with wind because wind speed can be utilized to scale most hydrodynamic processes at ocean surface. However, the wind-based gas transfer parameterization exhibits large variability for observations from field campaigns and laboratory experiments. This is because the ocean surface waves and wave breaking which directly restrain the CO_2 gas transfer rate are complicated in terms of scaling with wind speed. Wave breaking processes significantly increase the ocean surface turbulence and inject air bubbles (plunging breaker) into water column, which can not be exactly represented by wind speed alone. It is more intricate if we consider other factors such as surfactants, rain, current and ocean convection. Our study focuses on the direct dependence of CO_2 transfer velocity on waves and wave breaking. The gas transfer parameterization is developed, validated and used for estimation of global ocean air-sea CO_2 transfer. The following sections introduce the background for CO_2 transfer mechanisms,

experiments and observations, and estimation of CO_2 uptake by global ocean. The research objectives and thesis outline are also explained.

1.1 Air-sea CO_2 gas transfer

CO_2 gas exchange takes place at air-water interface when a gas concentration difference exists between air and bulk water. The gas flux is described as the multiplication of gas concentration difference and gas transfer rate. The latter is a function of kinetic forcing such as wind and waves at air-water boundary layer (Wanninkhof et al., 2009).

CO_2 is a slightly soluble gas so that the gas transfer resistance lies in the water side, that is, the mixing level in water determines the efficiency of CO_2 transfer. Molecular diffusion is the dominant mechanism for a tranquil water body. So the gas flux is quantified with the measurement of liquid mass diffusivity and gas concentration gradient. The mechanism is complicated if there is turbulence in water with resulted mixing rate several orders higher than that of molecular diffusion. The fluid parcels in the bulk water keep renewing the surface forced by turbulence. Based on the estimated surface renewal rate (Higbie, 1935; Danckwerts, 1951), gas transfer velocity can be calculated with reasonable assumptions. However, the surface renewal rate is an empirical parameter which results in uncertainty in estimating gas transfer rate. The turbulent dissipation rate which is widely used for characterizing energy dissipation is also found appropriate to describe gas transfer rate (Lamont and Scott, 1970; Zappa et al., 2001). Meanwhile, semi-empirical models for gas exchange rate are also developed in which the water surface wind speed is used as a proxy for water side turbulence. In the ocean, the surface hydrodynamic processes such as wave and current are deeply connected with wind velocity (e.g. Donelan et al., 1985). The consistent form of wind-based gas transfer model is presented in plentiful previous researches (e.g. Jahne et al., 1979; Wanninkhof, 1992; Wanninkhof et al., 2009; Krall and Jähne, 2014). By comparing the results from various studies, biases of predictions at high wind speed emerge due to the complexity of wave state and the biases can not be reconciled. Therefore, gas transfer models related with waves are increasingly considered in expressing gas transfer. Although the detailed physical mechanism about waves and gas transfer is still unclear, efforts have been made to use wave parameters (e.g. the wind-sea Reynolds number) directly in the empirical formula (Zhao et al., 2003; Woolf, 2005;

Zhao and Xie, 2010; Brumer et al., 2017a). The models comprising wave parameters enable us to close the gaps in previous measurements. Nonetheless, the challenge still exists in developing sophisticated and stable models to illustrate physical mechanisms related with waves.

The CO_2 gas exchange can be explored in different ways including laboratory experiment and field observation. In laboratory, researchers investigate the relationship between gas transfer and turbulence, wind or waves (Jähne et al., 1987; Ocampo-Torres et al., 1994; Asher et al., 1995). The mass balance for gas in the wind-wave flume is usually evaluated to compute gas exchange rate. Specifically, the tank water is generally supersaturated with CO_2 to ensure a concentration difference at air and water side. The main advantage of laboratory experiments is that the environmental forcing is precisely controlled and the CO_2 flux is evident enough to be measured. However, the limitation of laboratory experiment is also obvious in view of the fetch limit of wave flume and fresh water instead of sea water. Field observation at open ocean is another pathway to observe CO_2 flux. Delicate instruments for observing gaseous CO_2 have been developed for field campaigns. There are several field campaigns specifically designed for air-sea gas exchange such as: the Gas Experiment series (GASEX98,GASEX01) in 1998 and 2001 (McGillis et al., 2001, 2004), Southern Ocean Gas Experiment (SOGASEX) in 2008 (Edson et al., 2011), High Wind Gas Exchange project (HIWINGS) in 2013 (Blomquist et al., 2017). The gas flux, gas partial pressure and environmental wind and wave forcing were evaluated during those cruises. The past field observations largely enhanced our understanding of CO_2 exchange mechanism in relation with different conditions of wind and wave.

The motivation of building CO_2 transfer models is to estimate the global ocean CO_2 uptake. As one of the greenhouse gases, CO_2 in the atmosphere is critical in affecting global temperature change. The global carbon system was generally balanced in pre-industrial period between land, atmosphere and ocean. But the fast development of human society which is supported by fossil fuel combustion generates a huge burden on original carbon system because of the excessive anthropogenic CO_2 emissions into air. Ocean provides an important sink for gaseous CO_2 absorbing about 26% of anthropogenic emissions (Pachauri et al., 2014). The ocean inventory of inorganic carbon has been accumulating (Khatiwala et al., 2013) through air-sea gas exchange. Although it is almost certain that ocean is storing the emitted CO_2 in the past decades, the historical trend of global ocean uptake of CO_2 still can not be determined due to the large uncertainties in the

estimation of gas flux. Moreover, the general trend of global warming might decrease the capacity of ocean in storing CO_2 and the impact is yet to be precisely quantified (Takahashi et al., 1993). Researchers try to estimate the ocean CO_2 uptake using products collected from ship measurements (Landschützer et al., 2014; Rödenbeck et al., 2014), model simulation (Friedlingstein et al., 2019). The former method is based on large quantities of field measurements of ocean CO_2 concentration and a proper way to construct global CO_2 distribution while the latter method can give comprehensive estimation of land, ocean and air carbon content although the detailed physical, chemical and biological mechanisms are still obscure.

1.2 Research Objectives

The present work aims to investigate the air-sea CO_2 transfer and its dependence on wind and waves. The advanced parameterization with waves for gas transfer velocity is desired. Additionally, the global ocean uptake of atmospheric CO_2 by applying our gas transfer formula is expected to be well estimated with reduced uncertainties. Therefore, the specific objectives of our study can be outlined as,

1. Design experiments to measure CO_2 concentration effectively in laboratory.
2. Investigate the CO_2 gas exchange and its dependence on wind and wave forcing in the wave flume.
3. Develop effective parameterization of CO_2 gas transfer velocity in terms of wind and wave.
4. Study CO_2 gas transfer in the open ocean through field observations.
5. Validate and improve our parameterization from laboratory by employing field measurements.
6. Evaluate the global ocean CO_2 flux utilizing our parameterization.
7. Reproduce the historical track of annual CO_2 uptake by global ocean. Project the future trend based on the model simulation of CO_2 concentration.

1.3 Structure of the thesis

The thesis consists mainly three phases of work: building CO_2 transfer parameterization through laboratory work, field study and validation of the formula, estimation of global ocean CO_2 flux. The chapters are outline as follows:

Chapter 2–Theory This chapter details the theories related with our study including the gas transfer mechanisms, models for gas transfer rate, previous laboratory experiments, wave and wave breaking theories and researches on CO_2 flux over global ocean.

Chapter 3–Methodology This chapter outlines the methodology for our laboratory experiments and field study. The laboratory preparation, experimental setup and data processing are introduced. The method of processing field campaign data is also presented.

Chapter 4–Dependence of CO_2 transfer on wave breaking in laboratory This chapter include the analysis and results of laboratory experiments. New parameterization for transfer velocity in terms of wind and wave is established.

Chapter 5–Improved parameterization of CO_2 transfer based on field campaign observation This chapter comprises the results from field observation. Our parameterization from laboratory experiments is validated and improved through utilizing field data. The advantages of our formula are discussed.

Chapter 6–Evaluation of CO_2 uptake by global ocean This chapter is about the estimation of global ocean CO_2 flux with our formula. The historical trend as well as the projections are presented.

Chapter 7–Conclusions and Future Research This chapter summarizes the main conclusions of present work and discusses the future study to improve current work.

Chapter 2

Theory

2.1 Introduction

In this chapter, the theory about air-sea gas transfer and wave breaking used in our study is elaborated. CO_2 is an important greenhouse gas and can react with water molecule and further dissociate into ions in the carbonate system (see section 2.2). The mechanism of CO_2 gas transfer has been an essential scientific subject for decades. Multiple models for the gas transfer rate (section 2.3) have been developed to describe the dependence on molecule diffusion, turbulence induced by wind and waves and other influencing factors (e.g. rain, current, surfactants). The previous laboratory experiments are outlined in section 2.4, which provide theoretical support for our laboratory work. In this study, the relationship between gas transfer and waves is the main subject. So the relevant wave theories are introduced in section 2.5. The previous studies on CO_2 uptake by global ocean are also summarized in section 2.6.

2.2 Mechanisms of CO_2 gas transfer

2.2.1 Chemistry of CO_2 in water

Carbon dioxide (CO_2) is a sparingly soluble gas with a density about 50% higher than that of dry air. When dissolved in water, CO_2 reacts quickly with water molecule (H_2O), forming carbonic acid (H_2CO_3) which further dissociates into carbonate (CO_3^{2-}) and bicarbonate ions (HCO_3^-) as,

$$CO_2(aq) + H_2O \overset{K}{\rightleftharpoons} H_2CO_3 \overset{K_1}{\rightleftharpoons} H^+ + HCO_3^- \overset{K_2}{\rightleftharpoons} 2H^+ + CO_3^{2-} \tag{2.1}$$

where K, K_1 and K_2 are equilibrium constants. $CO_2(aq)$ represents the dissolved aqueous state CO_2. H_2CO_3 is unstable as an intermediate product in the reaction chain. The chemical reaction of water and CO_2 is reversible so that the carbonate system is always in dynamic equilibrium according to the change of environmental parameters (e.g. temperature, pH, pressure). The constants are dependent on water temperature, surface pressure, salinity and can be estimated as follows:

$$K = \frac{[H_2CO_3]}{[CO_2(aq)]} \tag{2.2}$$

$$K_1 = \frac{[H^+][HCO_3^-]}{[H_2CO_3]} \tag{2.3}$$

$$K_2 = \frac{[H^+][CO_3^{2-}]}{[HCO_3^-]} \tag{2.4}$$

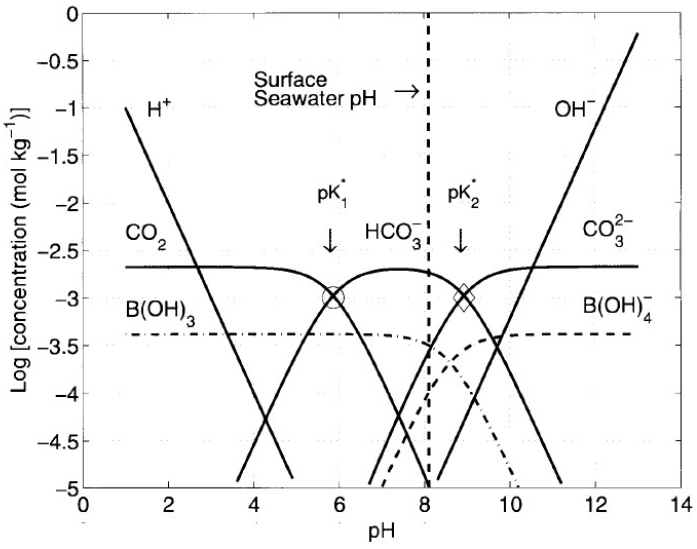

Figure 2.1: Bjerrum plot about carbonate system change with pH (Zeebe and Wolf-Gladrow, 2001). The reversible reaction of water and CO_2 is adjusted by pH of water. It should be noted that the carbon ions are converted to aqueous state CO_2 for pH less than 4.

The term total Dissolved Inorganic Carbon (DIC) is employed to describe the summation of constituents $CO_2(aq)$, H_2CO_3, HCO_3^- and CO_3^{2-} in water. Partial pressure of CO_2 (pCO_2) is also frequently used to denote the total $CO_2(aq)$ and H_2CO_3 particles in water although the amount of H_2CO_3 is usually negligible compared with $CO_2(aq)$. pH which represents the concentration of H^+ ions in water can effectively change the ratio of components in equation 2.1.

The relationships in the carbon system are demonstrated through Bjerrum plot (Zeebe and Wolf-Gladrow, 2001) in figure 2.1. The pH of ocean surface water lies at around 8, where the carbon ions (HCO_3^- and CO_3^{2-}) dominate in the system. With the increase of H^+ concentration (drop of pH), the carbon ions tend to transform into aqueous state CO_2. It is worth noting that when pH is below 4, $CO_2(aq)$ is the dominant form, so the DIC and partial pressure are close to each other.

2.2.2 air-water CO_2 transport mechanisms

Gas transfer process that occurs at air-water interface is driven by partial pressure difference at both sides. For soluble gas, the air side diffusion or turbulence restrains the gas exchange rate while for slightly soluble gas, the gas transfer resistance lies in the thin boundary layer at water surface. The molecular diffusion dominates in this layer for tranquil water body, and Fick's law can be used to describe the gas flux:

$$F = -D\frac{\partial \varphi}{\partial z} \sim -D\frac{\Delta \varphi}{\delta} \tag{2.5}$$

where the gas concentration (φ) is assumed homogeneous at horizontal directions. F denotes the gas flux which equals to the product of gas diffusivity D and concentration gradient vertically. δ is the thickness of diffusion layer in which the CO_2 concentration is assumed vertically linearly distributed. The thickness of the layer is inversely proportional to the turbulence intensity near surface. As diffusion layer at water surface hinders gas exchange, strong turbulence can effectively disrupt the diffusion layer and hence promote gas transfer. $\Delta\varphi$ is the gas concentration difference in diffusion layer and bulk water below. The heterogeneous distribution of CO_2 concentration is the driving force for gas exchange, so gas flux is further defined as,

$$F = k\Delta C, \tag{2.6}$$

where k is the gas transfer velocity and affected by both turbulence and diffusivity. $\Delta C = C_W - C_0$ represents the gaps of gas concentration in bulk water (C_W) and boundary layer at water surface (C_0). Usually, C_0 is conveniently adapted to gas concentration in air (C_a) at air-water interface as,

$$C_0 = \alpha C_a \tag{2.7}$$

where α is dimensionless Ostwald solubility coefficient. K is usually theoretically expressed as a main function of turbulent dissipation rate (ε) and kinematic viscosity (υ) as,

$$K = aD^n f(\varepsilon, \upsilon) = aSc^{-n} g(\varepsilon, \upsilon) \tag{2.8}$$

where a is a constant, Sc is Schmit number which is defined as ratio of kinematic viscosity and mass diffusivity ($Sc = \upsilon/D$), n is a ratio factor whose value varies for different conditions (e.g. $2/3$ for smooth water surface and $1/2$ for wavy water surface (Jähne et al., 1987)).

The gas flux can be derived by incorporating equation 2.7 into equation 2.6,

$$F = k(C_w - \alpha C_a) \tag{2.9}$$

For the situation that atmospheric CO_2 is absorbed by ocean (αC_a is bigger than C_w), F is mathematically negative. Another form of equation to describe gas flux is also commonly used, in which air-sea gas concentration is adapted to gas partial pressure in water (p_w) and air (p_a)

$$F = kL(p_w - p_a) \tag{2.10}$$

where $L(= \alpha(RT_w)^{-1})$ is the solubility of gas in water with unit $mol \cdot m^{-3} \cdot Pa^{-1}$. R is ideal gas constant ($8.314 m^3 \cdot Pa \cdot K^{-1} \cdot mol^{-1}$), T_w is temperature of water (unit K).

Liss (1973) described gas exchange at air-water interface in terms of separate air and water side parameters,

$$F = k_g(C_g - C_{sg}) = k_l(C_{sl} - C_l) \tag{2.11}$$

where k_g, C_g, C_{sg} refer to air side gas transfer velocity, gas concentration in bulk air and in boundary layer, respectively. The k_l, C_l, C_{sl} refer to the same variables accordingly but in water side. When the gas equilibrium is reached at air-water interface, C_{sg} and C_{sl} are linked through Henry's law constant (H) as,

$$C_{sg} = HC_{sl}, \tag{2.12}$$

By substituting equation 2.12 into equation 2.11 and eliminating C_{sg}, C_{sl}, the equation 2.11 can

be rewritten as,

$$F = K_g(C_g - HC_l) = K_l(\frac{C_g}{H} - C_l) \tag{2.13}$$

where the K_g and K_l are related with gas transfer velocity and given by,

$$\frac{1}{K_g} = \frac{1}{k_g} + \frac{H}{k_l}, \frac{1}{K_l} = \frac{1}{k_l} + \frac{1}{Hk_g} \tag{2.14}$$

The reciprocal of K_g and K_l denote the gas transfer resistance in air and water, respectively. The total resistance (R_t) which is the summation of resistance in air (R_g) and water (R_l) can be expressed as,

$$R_t = R_l + R_g = \frac{1}{K_l} + \frac{1}{K_g} \tag{2.15}$$

For sparingly soluble gas transfer such as CO_2, k_l is less than k_g by a few orders of magnitude in equation 2.14 so that R_g in equation 2.15 is negligible. Therefore, K_l is approximately equal to $1/R_t$. In our case of CO_2 gas transfer, it is reasonable to assume that the water side transfer velocity is equal to the total transfer velocity.

2.3 Models of gas transfer velocity

2.3.1 Stagnant film model

Combining equation 2.5 and equation 2.6, gas transfer velocity K can be expressed as,

$$K = \frac{D}{\delta} \tag{2.16}$$

which is the foundation of stagnant film model. The diffusive layer in this model is assumed to be stationary and remain unchanged, which is unrealistic when strong turbulence presents near water surface. Bolin (1960) employed the data of global ^{14}C flux at air-sea interface to obtain the effective stagnant film thickness of about 35 μm

2.3.2 Surface renewal model

To account for the contribution to gas exchange from turbulence which is more effective than molecule diffusion, surface renewal model is developed by assuming that turbulent eddies continuously and randomly renew the laminar sublayer near water surface. Considering one-dimensional Fick's second law,

$$\frac{\partial \varphi}{\partial t} = D\frac{\partial^2 \varphi}{\partial^2 z} \tag{2.17}$$

where the gas concentration φ is assumed homogeneous horizontally. By using initial condition $\varphi(z,0) = c_w$ and boundary condition $c(0,t) = c_{sw}$, the equation 2.17 can be solved and combined with equation 2.5, so the gas flux is given by,

$$F = D\frac{\partial \varphi}{\partial z}|_{z=0} = (c_{sw} - c_w)\sqrt{\frac{D}{\pi t}} \tag{2.18}$$

where t is the surface renewal period which denotes the time scale for eddies to circulate between surface and bulk water. Between the periodic replacements by turbulence, gas flux is still dominated by molecular diffusion. Thus, diffusivity D still exists in equation 2.18 while diffusion layer thickness disappears compared with stagnant film model. The gas transfer rate k is proportional to $\sqrt{D/\pi t}$ once the estimation of t is decided (e.g. Higbie, 1935).

Danckwerts (1951) assumed that the period of eddies staying at surface is changing with depth. Instead, the mean surface renewal rate s is a constant which is determined by the distribution of lifespan of surface eddies as,

$$\Theta(\theta) = se^{-s\theta} \tag{2.19}$$

where θ is the age of a specific eddy near water surface, Θ is the distribution of eddy lifetimes. After integration over lifetime of eddies in equation 2.19, the transfer velocity is derived as,

$$k = (Ds)^{\frac{1}{2}} \tag{2.20}$$

which is the same with k in equation 2.16 when δ takes $\sqrt{D/s}$. $\sqrt{1/s}$ represents the characteristic eddy renewal time at water surface.

The development of models can be further advanced by investigating time scale parameter which may be related with eddy size. Fortescue and Pearson (1967) believed that large-scale

turbulent eddies dominated the surface fluid motion. The transfer velocity k is proportional to $(DV/l)^{1/2}$ where l is the length scale of large eddy elements and V is the root mean turbulent intensity. Lamont and Scott (1970), however, argued that very small scale turbulent motion was effective in modeling gas transfer. In their parameterization (equation 2.21), the k is determined by turbulent dissipation rate (ε) and kinematic viscosity (ν) by a power of 0.25.

$$k \propto (\varepsilon\nu)^{\frac{1}{4}} Sc^{-\frac{1}{2}} \tag{2.21}$$

The relationship between gas transfer velocity and near surface turbulence, $k \sim \varepsilon^{\frac{1}{4}}$, is supported by coastal measurements in several studies (Zappa et al., 2007; Tokoro et al., 2008)

2.3.3 Models with wind speed

Wind is one of the main driving forces responsible for water surface boundary hydrodynamic processes. Considering that most hydrodynamic processes can be scaled with wind speed, empirical models are thus developed based on wind forcing.

Deacon (1977) developed a semi-empirical model to calculate gas transfer velocity at smooth water surface. The computed results match well with laboratory measurements at low wind speeds (Jahne et al., 1979) and the model does not depend on surface renewal time. The k is expressed as,

$$k = 0.082(\rho_a/\rho_w)^{\frac{1}{2}} Sc^{-\frac{2}{3}} u_* \tag{2.22}$$

where ρ_a/ρ_w is density ratio of air and water, Sc is Schmit number, u_* is the friction velocity of the surface air flow. The model is based on smooth surface which is physically unrealistic when waves are forced by wind. The gas transfer velocity tend to increase non-linearly with high wind speeds at a rough surface with waves. Jähne et al. (1987) demonstrated that with low wind speed, the gas transfer could be modeled by assuming a rigid wall at water surface where k is proportional to $Sc^{-\frac{2}{3}}$. At high wind speed, a free surface boundary condition should be considered and the resulted k is proportional to $Sc^{-\frac{1}{2}}$.

Liss and Merlivat (1986) considered the sea surface with conditions of smooth, rough and wave breaking based on the observations in lake (Wanninkhof et al., 1985) and laboratory experiments in a wind-wave tunnel. They proposed a formula in which gas transfer rate k_w was linearly related

with wind speed in separate ranges,

$$k_w = \begin{cases} (0.17U_{10})(Sc/600)^{-\frac{1}{2}} & U_{10} \leq 3.6m/s \\ (2.85U_{10} - 9.65)(Sc/600)^{-\frac{1}{2}} & 3.6m/s < U_{10} \leq 13m/s \\ (5.9U_{10} - 49.3)(Sc/600)^{-\frac{1}{2}} & U_{10} > 13m/s \end{cases} \tag{2.23}$$

The understanding of gas transfer is enhanced with the development of study methods. Early researches usually employed indirect method with the measurements of tracer's (e.g. ^{14}C, ^{222}Rn) concentration change in atmosphere and ocean. Watson et al. (1991) for the first time used the ratio of dual tracers' concentration (SF_6 and ^3H_e) change to estimate gas transfer coefficient k and the method was proved to be quite efficient. Later, the tracer method was widely adopted by field and laboratory study.

Wanninkhof (1992) employed carbon isotope ^{14}C concentration measurements originated from atomic bomb explosion and found that gas transfer velocity was proportional to quadratic wind speed. They proposed a dependence of gas transfer rate on long-term average wind speed (U_{10av}) as well as on short-term wind speed (U_{10}),

$$k_w = \begin{cases} (0.39U_{10av}^2)(Sc/600)^{-\frac{1}{2}} \\ (0.31U_{10}^2)(Sc/600)^{-\frac{1}{2}} \end{cases} \tag{2.24}$$

Based on the same data set, Wanninkhof and McGillis (1999) revised the parameterization by considering cubic wind speed in the formula for high wind condition,

$$k_w = \begin{cases} (1.09U_{10av} - 0.333U_{10av}^2 + 0.078U_{10av}^3)(Sc/600)^{-\frac{1}{2}} \\ (0.0283U_{10}^3)(Sc/600)^{-\frac{1}{2}} \end{cases} \tag{2.25}$$

Nightingale et al. (2000) reported the experiments in North Sea using dual tracer technique. The resulted formula consists of a combination of linear and quadratic wind speed,

$$k_w = (0.333U_{10} + 0.222U_{10}^2)(Sc/660)^{-\frac{1}{2}} \tag{2.26}$$

Similarly, Ho et al. (2006) conducted an experiment in Southern Ocean for which dual gas tracer technique was employed. The k_w was obtained at high wind speed (up to 16 m/s) and a clearly

quadratic relationship was found,

$$k_w = 0.266U_{10}^2(Sc/660)^{-\frac{1}{2}} \tag{2.27}$$

Sweeney et al. (2007) utilized a database of dissolved inorganic radiocarbon ^{14}C and the global mean wind field from NCEP/NCAR reanalysis data to propose a gas transfer velocity formula for global ocean CO_2 flux,

$$k_w = 0.27U_{10}^2(Sc/660)^{-\frac{1}{2}} \tag{2.28}$$

The revised formula successfully produced the estimation of CO_2 uptake by global ocean with reduced gaps compared with previous studies.

Water surface heat flux has been applied as another kind of tracer because the temperature can be measured with high frequency and precision. Jähne et al. (1989) managed to estimate the heat flux with infrared method and found the relationship between gas and heat transfer rate. Although the infrared method is frequently used in gas transfer experiments to observe wave breaking and turbulence, the mechanism between heat flux and gas transfer is still in debate.

With the development of observation instruments, the air side gas concentration can be measured in high frequency. A new method named eddy covariance technique is developed for direct estimation of gas flux,

$$F = \overline{w'c'} \tag{2.29}$$

where w is vertical wind velocity, c is the gas concentration at air near interface, prime denotes the fluctuation of variables, overbar denotes the mean of $w'c'$. The vertical components of wind, gas concentration need to be measured in high frequency for the computation of fluctuations. Because of the small signal-to-noise ratio, high sampling rate (usually higher than 2 Hz) and high precision are required during measurements. Therefore, this method is suitable for conditions when there is a significant difference of air-sea gas concentration to ensure a large signal of c'. Moreover,when deploy the related instruments in field, cautions should be paid to the influence of water vapor interference and platform motion.

Several field campaigns specifically for gas exchange at open ocean were conducted in the past decades, in which the gas flux was directly estimated using the covariance method based on the high-frequency measurements on ship. In 1998, the gas experiment (GASEX-98) was conducted

in Atlatic ocean where the sea is known as a sink region (gas dissolves from air into the sea) for atmospheric CO_2. McGillis et al. (2001) analyzed the GASEX-98 data and found that cubic wind speed could better describe gas transfer velocity by assuming that the gas transfer rate is dominated by breaking waves,

$$k_w = (3.3 + 0.026U_{10}^3)(Sc/660)^{-\frac{1}{2}} \tag{2.30}$$

where the k_w is not zero when wind speed vanishes and is corrected with Schmidt number for sea water at 20^oC ($Sc = 660$). The gas flux estimation in GASEX-98 showed a general agreement with traditional isotope method. However, many recent researches (Prytherch et al., 2010a; Edson et al., 2011) suggested that special corrections are needed for the flux estimation.

Another campaign on gas experiment at year 2001 (GASEX-01) was conducted in eastern equatorial Pacific Ocean which is known as a source region (gas escape from the sea to air) for gaseous CO_2 with relatively low wind speed. McGillis et al. (2004) presented the measurements of gas flux for GASEX-01. They suggested a revised formula for gas exchange rate,

$$k_w = (8.2 + 0.014U_{10}^3)(Sc/660)^{-\frac{1}{2}} \tag{2.31}$$

Prytherch et al. (2010a) reported the measurement from a field campaign in the North Atlantic. The calculated gas flux from direct covariance method was further corrected for water vapor cross-talk by using the so-called "PKT" method. The wind speed during the cruise was up to 19.6 m/s, and a cubic dependence of transfer velocity on wind speed was presented,

$$k_w = (5.3 + 0.034U_{10}^3)(Sc/660)^{-\frac{1}{2}} \tag{2.32}$$

In 2008, the Southern Ocean Gas Exchange (SOGASEX) program was carried out for the measurements of air-sea mass, momentum and heat fluxes at Southern Ocean. Edson et al. (2011) successfully estimated the gas flux by applying a spectral method for the correction of gas flux which was consistent with results by using "PKT" correction. A cubic dependence of transfer velocity on wind speed was presented which is close to formula 2.32,

$$k_w = (5.4 + 0.029U_{10}^3)(Sc/660)^{-\frac{1}{2}} \tag{2.33}$$

More recently in 2013, the High Wind Gas Exchange Study (HIWINGS) was conduced at north Atlantic Ocean. The main purpose was to enhance the understanding of air-sea interaction at high wind speed with large waves and whitecap coverage. The gas flux (CO_2 and DMS) was measured with installation of water-vapor drying section and the flux was corrected properly by Blomquist et al. (2017). The observational data from cruise SOGASEX and HIWINGS are also used in this study in chapter 5.

The covariance method is also applicable on fixed observational platform on/off the coast. For example, Jacobs et al. (1999) observed CO_2 gas flux in North Sea on a platform off the coast through eddy covariance technique. Combined with the measured gas partial pressure, a quadratic relationship with wind speed was obtained,

$$k_w = 0.31U_{10}^2(Sc/660)^{-\frac{1}{2}} \tag{2.34}$$

Weiss et al. (2007) estimated the gas flux through eddy correlation system on a platform in Baltic Sea. The computed relationship of gas transfer velocity is,

$$k_w = (0.46U_{10} + 0.365U_{10}^2)(Sc/660)^{-\frac{1}{2}} \tag{2.35}$$

If the sampling frequency is not high enough for direct estimation of gas flux, an optional method of eddy accumulation can be used (Wanninkhof et al., 2009). The gas flux is determined by gas concentration difference at upward and downward air flow, C_{up} and C_{down}, respectively. The gas flux is expressed as,

$$F = b_x\sigma_w(C_{up} - C_{down}), \tag{2.36}$$

Where σ_w represents the standard deviation of vertical wind velocity, b_x depends on the length scales of turbulence. The vertical component of the wind velocity and the gas concentration can be measured with relatively low frequency. Zemmelink et al. (2004) applied the technique to measure the gas flux at Pacific Ocean and obtained the transfer velocity although a high scatter was also reported.

Wanninkhof et al. (2009) conducted a comprehensive review of gas transfer theory and observation techniques. It was suggested that the wind speed with magnitude of power from 1-3 should be used in the gas transfer parameterization to scale different level of impact from hydrodynamic

processes (e.g. wave and wave breaking) accompanied with low to high wind forcing,

$$k_w = (3 + 0.1U_{10} + 0.064U_{10}^2 + 0.011U_{10}^3)(Sc/660)^{-\frac{1}{2}} \tag{2.37}$$

In summary, although coefficients in the above mentioned equations vary according to specific observations, the gas transfer rate could generally be described as $aU_{10}^n Sc^{-\frac{1}{2}} + c$, where a, n and c are constants. The wind-based parameterization exhibits large variations especially in the high wind speed region by comparing different data sets. Therefore, wind speed alone may not be adequate to predict gas transfer velocity considering the importance of non-linear processes such as wave breaking and the breaking induced turbulence and bubbles under the condition of high wind-wave state.

2.3.4 Models with wave parameters

For CO_2 gas transfer, the efficiency mainly depends on the degree of water side resistance which decreases with more turbulent processes. In the presence of waves, the turbulence is induced by wave-orbital motion and by wave breaking (e.g. Babanin et al., 2011). The latter also produces bubble clouds which dramatically increase the water-air contact area and are transported down into the water column.

Considering the water surface waves, Jähne et al. (1987) found that the mean square slope of waves was an appropriate parameter to describe the gas transfer velocity. In addition, the dependence of gas transfer rate on Schmidt Number (Sc), which is the ratio of fluid kinematic viscosity and mass diffusivity, changed from $Sc^{-\frac{2}{3}}$ to $Sc^{-\frac{1}{2}}$ due to the wavy surface. Bock et al. (1999) conducted experiments in wind-wave flume and verified that the mean square slope of short waves was well correlated with gas transfer rate. Zappa et al. (2001, 2004) employed infrared technique to detect micro-wave breaking in wave tank and found that the gas transfer velocity scaled well with fractional area coverage of micro-breakers. Frew et al. (2004) examined the impact of wind stress and waves on gas transfer through field observation. They found that the parameterization with mean square slope could better explain the variance of data than by using wind stress.

At high wind speed, Monahan and Spillane (1984) assumed that breaking waves dominated the

gas transfer for slightly soluble gas and expressed the transfer velocity by splitting the contribution from non-breaking area and wave breaking area:

$$k = k_m(1 - W) + k_w W \tag{2.38}$$

where k_m and k_w denote the gas transfer rate at non-breaking surface and breaking surface, respectively. W is the whitecap coverage. Asher et al. (1995) further split the term k_w into two parts: gas transfer contributed by turbulence due to wave breaking (k_t) and bubble-mediated gas exchange (k_b). So equation 2.38 can be rewritten as,

$$k_w = \{k_m + (k_t - k_m W)\} + k_b W \tag{2.39}$$

Considering that the whitecap coverage can be better characterized by a breaking-wave parameter R_B than by wind speed, Zhao et al. (2003) attempted to correlate gas transfer velocity (k_w) with R_B through whitecap coverage (W) as,

$$k_w = 687.9W^{0.58},\ W = 3.88 \times 10^{-7} R_B^{1.09} \tag{2.40}$$

where $R_B = u_*^2/\nu\omega_p$, u_* is the wind friction velocity, ν is kinematic viscosity of air, ω_p is the peak wave angular frequency. R_B is regarded as a wind-sea Reynolds number and interpreted to represent the turbulence intensity generated by breaking waves. Similarly, another parameter R_H which also takes the form of Reynolds number is proposed (Woolf, 2005; Zhao and Xie, 2010) as,

$$R_H = u_* H_s/\nu \tag{2.41}$$

where H_s is significant wave height. The wind-sea Reynolds numbers R_B and R_H are composed empirically to consider the impact of both wind and sea state. The relationship between gas transfer (CO_2 and DMS) and the wind-sea Reynolds numbers was further evaluated by Brumer et al. (2017a) with observations from different field campaigns. The CO_2 transfer rate is expressed as,

$$k_{660} = 2.04 \times 10^{-4} \times \left(\frac{u_* H_s}{\nu_w}\right)^{0.88} \tag{2.42}$$

$$k_{660} = 9.05 \times 10^{-3} \times \left(\frac{u_*^2}{\nu_w \omega_p} \right)^{0.69} \tag{2.43}$$

where k_{660} denotes the gas transfer velocity corrected by Schmidt number for sea water at 20^oC ($Sc = 660$), ν_w is kinematic viscosity of sea water. It is found that the Reynolds numbers perform better than wind-only gas transfer parameterization in collapsing the observational data sets with reduced uncertainty.

Woolf (2005) split transfer velocity into two parts as in equation 2.38 and described the gas transfer contributed by breaking waves through whitecap coverage,

$$k_w = 1.57 \times 10^{-4} u_* (Sc/600)^{-\frac{1}{2}} + 850W \tag{2.44}$$

where W could be further related with wind-sea Reynolds number R_H. The first term on the right of the equation is adopted from Jähne et al. (1987), denoting the gas transfer rate related with non-breaking waves.

Bubble clouds that are produced by breaking waves have critical influence on poorly soluble gas transfer at air-sea interface. Based on field observation, Bell et al. (2017) analyzed the data sets for DMS (soluble gas) and CO_2 gas transfer over a range of wind speed up to 21 m/s. With higher whitecap coverage which is related with bubble population at high wind speed, CO_2 gas transfer is more enhanced than DMS transfer. The behavior of bubbles has been recognized in two ways: for small bubbles that are forced into water, they rise slowly and may be totally dissolved before resurface; for large bubbles, they increase the air-water contact area and usually rise fast to burst at water surface. Memery and Merlivat (1985) investigated the effect of single bubble and proposed a simple model to account for bubble-mediated gas transfer velocity (k_b),

$$k_b = -\frac{\int\int w(\partial\Psi/\partial z) Q dr dz}{c - SP_a} \tag{2.45}$$

where w is the bubble rising velocity, $\partial\Psi/\partial z$ is the bubble size distribution along depth, Q is the total gas flux through bubbles depending on bubble radius r and location depth. c is the concentration of gas in water, S is gas solubility and P_a is the partial pressure of gas in bubbles which are over pressured in water. Similarly, Woolf and Thorpe (1991) suggested that the net gas transfer of bubbles depended on bubble size, depth, concentration of gas, composition of bubbles and time

history of each bubble. A numerical model was constructed considering single bubble dynamics and surrounding water motion. Keeling (1993) studied the bubble population and provided a parameterization which comprised in-gassing and out-gassing processes through bubble interface. The gas transfer caused by bubbles is described as,

$$F_b = k_b^{in} S P_a - k_b^{out} S P_w \tag{2.46}$$

where P_a and P_w are gas partial pressure in air and water, respectively. The k_b is proportional to solubility and diffusivity in $S^{-0.3}D^{-0.35}$. The study revealed that bubbles began to play an important role when wind speed exceeded 10 m/s. In addition, the role of large-size bubbles was emphasized. Asher et al. (1996) conducted experiments at wave tank and yielded an empirical model to predict k_b from bubble plume coverage, diffusivity and solubility (α). k_b is proposed as,

$$k_b = a/\alpha + bSc^{-x}\alpha^{-y} \tag{2.47}$$

where a, b, x, y are constants in model which are determined by bubble population.

Based on the model from Woolf and Thorpe (1991), Woolf (1997) combined the gas transfer of bubbles (k_b) and non-breaking waves (k_s) (Jähne et al., 1987). The total flux (F_t) is given by,

$$F_t = (k_s + k_b)[C_w - SP_a(1+\Delta)] \tag{2.48}$$

where C_w is the gas concentration in water, S is the gas solubility, P_a is the gas partial pressure in air, Δ denotes the extra pressure in bubbles. k_b is suggested as,

$$k_b = 9.4 \times 10^{-3} U_{10}^{3.41} \alpha^{-1} [1 + (14\alpha Sc^{-1/2})^{-\frac{1}{1.2}}]^{-1.2} \tag{2.49}$$

It should be noted that the quasi-cubic wind speed is used as a proxy for bubble effect.

Stanley et al. (2009) used the measurements of five types of noble gas exchange which was influenced by both molecular diffusion and bubbles. The total gas flux is divided as flux at unbroken surface F_s, small-bubble (completely dissolved bubbles) devoted gas flux F_c, large-bubble

(partially dissolved bubbles) devoted gas flux F_p,

$$F_t = F_s + F_c + F_p \tag{2.50}$$

The corresponding gas transfer velocity for the flux constituents are scaled with wind speed,

$$\begin{cases} k_s = 8.67 \times 10^{-7} U_{10}^2 (Sc/660)^{-1/2} \\ k_c = 9.1 \times 10^{-11} (U_{10} - 2.27)^3 (\frac{P_a}{RT}) \\ k_p = 2.3 \times 10^{-3} (U_{10} - 2.27)^3 \alpha (\frac{D_i}{D_o})^{\frac{2}{3}} (\frac{P_b - P_w}{RT}) \end{cases} \tag{2.51}$$

in which D_i is diffusion coefficient, D_0 is a constant, P_a, P_b and P_w are gas partial pressure in air, bubbles and bulk water, respectively. Similar with other studies (e.g. Wanninkhof et al., 2009), the bubble effect is represented with cubic wind speed. Following the same framework in equation 2.50, Liang et al. (2013) developed another set of parameterization for gas transfer velocity in the model,

$$\begin{cases} k_s = \frac{u_a^*}{r_w + r_a} (Sc/660)^{-1/2} \\ k_c = 5.56 (u_w^*)^{3.86} \\ k_p = 5.5 (u_w^*)^{2.76} (Sc/660)^{-2/3} \end{cases} \tag{2.52}$$

where u_a^* and u_w^* are friction velocity at air and water side, respectively. r_a and r_w refer to gas exchange resistance in air and water side, respectively. The description of k_s is adopted from the NOAA (National Oceanic and Atmospheric Administration) COARE (Coupled Ocean-Atmosphere Response Experiment) model (Fairall et al., 2003, 2011). The COARE model was originally developed based on the cool skin model through adapting work of Soloviev and Schlüssel (1994). The gas transfer parameterization as an extension in the model comprises the mechanisms for both air side and water side gas transfer. The latter is specifically split into molecular-turbulent affected gas transfer terms and bubble-mediated gas transfer terms.

2.3.5 Other influencing factors on gas transfer

Apart from wind and waves, several other factors also affect gas transfer efficiency. Surfactants at sea surface could inhibit gas exchange by attenuating the growth of short waves (Frew et al., 2004) and decrease the wind friction velocity. Tsai and Liu (2003) found that surfactants at ocean

surface could reduce global CO_2 uptake by 20%. However, surfactants at CO_2 source area of ocean may also hinder the gas exchange so that the net global uptake could be increased (Asher et al., 1997). Rain drop is another force that can induce sea surface turbulence thus promote gas transfer. Ho et al. (2004) concluded that rain can remarkably increase gas transfer rate because of the strengthened surface energy dissipation and bubbles. Turk et al. (2010) estimated the enhanced gas flux due to rain at western equatorial Pacific and found that rain could dilute the sea water so that the source region could turn into sink region. Ocean current is thought to be another parameter to promote gas exchange. Zappa et al. (2003) found that tidal current at low wind speed was correlated with gas transfer velocity. The importance of convection at ocean surface layer was also recognized in McGillis et al. (2004). The gas transfer velocity that was correlated with convection difference for daytime and night exhibited a diurnal cycle at equatorial ocean.

2.4 Laboratory experiments on gas transfer

In the laboratory, the dynamic forcing such as wind and waves can be well controlled and measured. Hence, laboratory experiment in wind wave flume provides an appropriate way to investigate the gas exchange. Traditionally, mass balance technique is used in the experiments. By exerting a gas concentration change in water as a perturbation, the particular gas in air and water will equilibrate again. During this interval, the mass concentration change with time will be measured for further computation of the gas transfer velocity. The theory can be briefly describe as

$$F = \partial M / \partial t A^{-1} \tag{2.53}$$

where F is the gas flux of a water column, M is the mass of particular gas, A is the water surface area. This method is typically accomplished by monitoring the gas concentration in water.

Ocampo-Torres et al. (1994) measured gas exchange in a 32-meter long wind wave tunnel with wind speed varied from 1 to 24 m/s. In the experiment, infrared analyzer was used for measurements of CO_2 and water vapor. Tank water was supersaturated with CO_2 gas (evasion experiments) and the CO_2 concentration decrease in water was monitored. CO_2 transfer velocity was calculated as,

$$\frac{\partial C_a}{\partial t}\frac{V_a}{A} = -\frac{K_{CO_2}}{H}(C_a - C_g) \tag{2.54}$$

$$\frac{\partial C_g}{\partial t}\frac{V_w}{A} = -K_{CO_2}(C_g - C_a) \tag{2.55}$$

where C_g and C_a are CO_2 concentration in equilibrated gas and air, respectively. H is Henry's law parameter, V_a and V_w are volume of air and water in the flume, respectively, A is area of air-water interface. A revised Henry's law constant was reported for computing gas concentration. By comparing CO_2 and water vapor transfer, it was indicated that at high winds, poorly soluble gas ventilation at air-water interface could be much more enhanced than that of soluble gas. Equation 2.55 will be used in our laboratory experiment in chapter 4.

Wanninkhof et al. (1995) conducted experiments at an outdoor surf pool. The CO_2 transfer rate was given by,

$$k = \frac{-h\partial DIC/\partial t}{S(PCO_{2w} - PCO_{2a})} \tag{2.56}$$

where h is water depth, S is solubility of gas. The DIC was measured by a coulometer after injecting acid into water sample. Partial pressure (pCO_{2w}, pCO_{2a}) was measured through a equilibration system. The role of bubbles induced by wave breaking was discussed and it was suggested that bubble effect should be included in parameterization of gas transfer.

Rhee et al. (2007) investigated the dependence of gas exchange on wind and waves in a large wind wave tunnel. Various types of gas were used and their transfer velocities were estimated. In particular, the gas transfer with wind forced waves and mechanically generated waves superimposed with wind were examined. They found that gas transfer with pure wind waves was generally consistent with the description of surface renewal model. For mechanically generated waves superimposed with wind, interestingly, DMS gas transfer rate was found suppressed which might be due to the attenuation of wind-wave related microbreaking modulated by mechanical waves.

Iwano et al. (2013) performed gas transfer experiment in laboratory with hurricane wind speed (U_{10} up to 70 m/s). In the experiment, DIC was measured by using a total organic carbon meter (model TOC-V-CSH), the pH was measured to calculate partial pressure of CO_2. Gas exchange velocity was found largely promoted when the wind speed was higher than 33 m/s. By comparing with proposed gas transfer models in previous studies, the results agreed well for low to moderate wind speeds while equation 2.37 from Wanninkhof et al. (2009) gave a good prediction at high wind speed. Krall et al. (2019) performed comprehensive lab experiments in which the highest wind speed is extended to 85 m/s. 12 trace gases were tested together with situations of fresh

water and sea water in the wave flume. A dramatic increase of gas transfer was observed at wind speed exceeding 33 m/s for both fresh water and sea water. Bubble enhanced gas transfer was not significant and was observed only effective for low-solubility tracers.

2.5 Waves and wave breaking at ocean surface

The energy dissipation due to wave breaking is a most essential subject of surface wave dynamics, relevant for the gas exchange. The importance of wave breaking on air-sea interaction has been discussed in Melville (1996) and Babanin et al. (2011). Due to the energy loss, wave breaking enhances intensity of the under-surface turbulence by up to 3 orders of magnitude, it produces bubbles and may spend up to 50% of energy loss on work against the buoyancy forces acting on these bubbles. Wave growth and ultimately its breaking are connected with the wind, hence there is correlation between gas transfer rate and wind speed. But this is by far not a direct connection and reason for the breaking is non-linear evolution of waves (or wave superposition), not the wind (Babanin et al., 2011).

2.5.1 Theory of wave modulational instability

Benjamin and Feir (1967) theoretically and experimentally studied the stability of a stable wave train with small disturbances. With sideband (or noise) imposed on the carrier wave, the disturbance is amplified with the propagation of waves. This phenomenon is called modulational instability or Benjamin & Feir instability. The prerequisite of the instability is derived as

$$0 < \hat{\delta} \leq \sqrt{2} \tag{2.57}$$

where $\hat{\delta} = \delta\omega/\epsilon\omega_0$, $\delta\omega$ is perturbation frequency, ϵ is the steepness of carrier waves which is the product of wave amplitude and wavenumber, ω_0 is the carrier wave frequency. The growth rate $(d(\ln a)/d(kx))$ of initial sideband amplitude with wave propagation distance is predicted as,

$$\beta = \epsilon^2\hat{\delta}(2-\hat{\delta}^2)^{1/2} \tag{2.58}$$

Tulin and Waseda (1999a) conducted systematic laboratory experiment to investigate instability of non-linear deep water waves with wide range of initial steepness and sideband frequency. Modulational effect for non-breaking and breaking waves are presented. Without wave breaking, the energy shifting is observed reversible among wave components with spectrum recovered although some energy transfer into discretized high frequency constituents. For waves that break during propagation, the energy shifting is found irreversible. The wave energy which originally lies in carrier wave is divided and roughly half shifted to lower sideband. Waseda and Tulin (1999b) explored wind effects on modulational instability of deep water waves. It was reported that wind forcing could alter the sideband growth for the cases with seeded sideband and change the modulational frequency for unseeded cases (natural modulation).

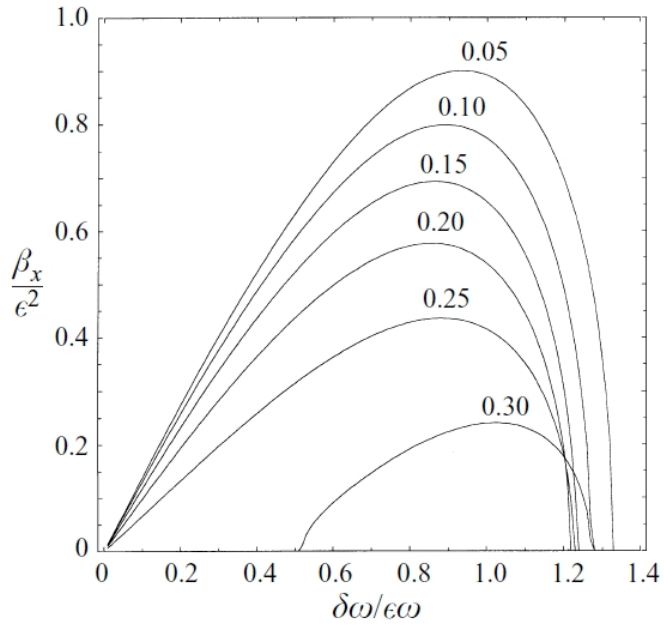

Figure 2.2: Initial sideband growth rate (β_x) and its dependence on wave steepness (ϵ) and frequency (ω) (Tulin and Waseda, 1999a).The steepness of carrier wave ϵ ranges from 0.05 to 0.30.

For non-linear wave groups, the non-linear Schrödinger equation was found to be able to describe the evolving modulated waves (Zakharov, 1968). One of the widely used solution to this non-linear equation was presented by Krasitskii (1994). Based on this solution, Tulin and Waseda (1999a) depicted the initial growth rate and its dependence on sidebands as in figure 2.2. β_x is initial growth rate of sideband. The steepness of carrier wave ϵ ranges from 0.05 to 0.30. $\delta\omega/\epsilon\omega_0$

is the modulational frequency.

Babanin et al. (2007) investigated the two-dimensional monochromatic waves in deep water. Wave breaking and its dependence on initial modulational steepness (IMS) were discussed. Moreover, it was concluded that the position of breaking onset and breaking probability can be predicted through figure 2.3. With the increase of IMS, the resulted breaking distance and reverse of the breaking probability both decrease.

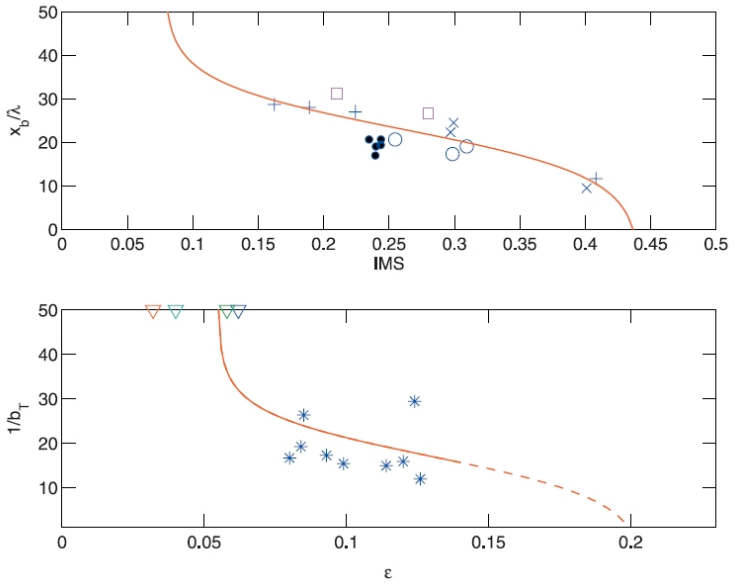

Figure 2.3: The top figure shows that the breaking position which is normalized by wave length varies with initial modulational steepness (IMS); The bottom figure shows that the reverse of breaking probability is correlated with peak spectral steepness ϵ (Babanin et al., 2007).

Numerical modelling is another effective way to study the evolution of non-linear waves. The model used in our study is Chalikov-Sheinin (CS) model (Chalikov and Sheinin, 1996). This model is characterized by a surface-following coordinate system and simplified evolutionary equations which are approximated by using Fourier expansion. It is efficient and accurate for the simulation of 1D gravity, gravity-capillary waves as well as waves in presence of wind forcing. The detailed description of solution to evolutionary equations and simulations can be referred to previous studies (Chalikov and Sheinin, 1996, 2005; Chalikov and Rainchik, 2011).

2.5.2 Theory of wave breaking

Wave breaking is a strong hydrodynamic process which can significantly promote transfer of sparingly soluble gas. The parameter which is commonly used to describe wave breaking is whitecap coverage for extensive breaking. For wave statistics, breaking probability (b_T) and breaking severity (S) are also frequently mentioned. The breaking probability is defined as the number of breaking events of dominant waves per dominant wave period (T_d) when they pass through a fixed point (Banner et al., 2000; Babanin et al., 2001). It is described as

$$b_T = \frac{nT_d}{t} = \frac{n}{N} \tag{2.59}$$

where n is the number of breaking crests, t is total time and $t = NT_d$, N is the total number of dominant waves with period T_d passing a fixed point. Breaking severity is defined as the energy loss for waves in the breaking process. It can be used for analysis of individual and spectral waves. The wave energy per unit area is described as (Young, 1999),

$$E(f) = \frac{1}{8}\rho_w g H(f)^2 \tag{2.60}$$

where ρ_w is the water density, g is gravitational acceleration, wave height ($H(f)$) is a function of wave frequency(f). So the energy loss for breakers is given as,

$$E_S(f) = s(f)E(f) \sim s(f)H(f)^2 \tag{2.61}$$

where the loss of energy (E_S) and breaking severity (s) are functions of wave frequency. The breaking severity can also be parameterized as

$$s = \frac{\epsilon_{after}^2}{\epsilon_{before}^2} \tag{2.62}$$

where ϵ_{after} and ϵ_{before} represent peak wave steepness after and before breaking, respectively. There is still scientific debate on the quantity of wave breaking severity. Further studies on wave breaking induced energy loss in laboratory and open ocean can be referred to previous studies (Babanin et al., 2010, 2011; Galchenko et al., 2010, 2012)

2.6 Air-sea CO_2 flux over global ocean

The global carbon balance has been a prevailing topic in the past decades because the excessive anthropogenic emission of CO_2 into atmosphere is responsible for many global environmental issues (e.g. climate change, ocean acidification). The "Keeling curve" for atmospheric CO_2 is showed

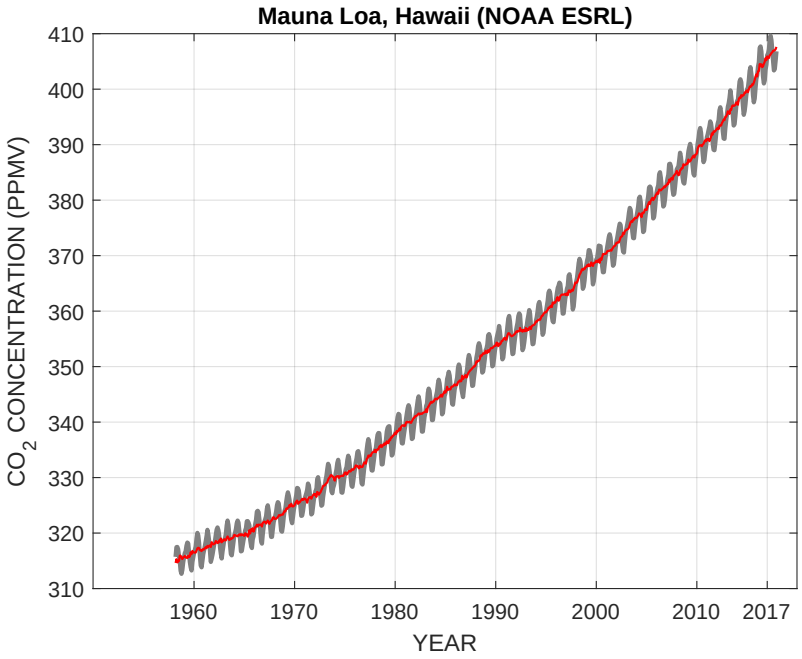

Figure 2.4: Trend of atmospheric CO_2 measured at Mauna Loa, Hawaii island from 1958 to 2017. Grey line represents the seasonal cycle, red line denotes monthly mean.

in figure 2.4. The monthly mean CO_2 concentration (red curve) at Hawaii is obviously increasing from about 320 ppm in 1960 to about 400 ppm in 2017. The emission of anthropogenic CO_2 from forestry, fossil fuel combustion and cement production is accumulating in the atmosphere, which further causes the rise of global temperature and ocean acidification. Ocean is dynamically exchanging CO_2 with atmosphere in the carbon system with a net sink CO_2 flux from air to sea and absorbing about 26% of the anthropogenic CO_2 emissions (Pachauri et al., 2014). To date, the accurate estimation of the global ocean CO_2 uptake is still in debate.

To compute the CO_2 flux over global ocean, transfer velocity parameterization (see section 2.3) and global CO_2 partial pressure distribution are needed. Takahashi et al. (2009) employed the global CO_2 gas transfer formula 2.63 (Sweeney et al., 2007) to evaluate the global ocean CO_2

uptake in reference year 2000,

$$k_w = 0.26U_{10}^2 \cdot (660/Sc)^{\frac{1}{2}} \tag{2.63}$$

The water side CO_2 partial pressure pCO_{2w} database in the study consists of 3 million measurements from shipboard equilibration system. Without considering the impact of El Niño events and by taking into account of the pre-industrial steady state ocean source (riverine transportation) flux of $0.4 \pm 0.2 PgC/yr$, the estimated global ocean net flux for year 2000 is $-2.0 \pm 1.0 PgC/yr$. The riverine CO_2 transportation into ocean of $0.4 \pm 0.2 PgC/yr$ is supported by several researches (Sarmiento and Sundquist, 1992; Bender et al., 2005; Jacobson et al., 2007). However, recent studies (Resplandy et al., 2018) argued that the riverine carbon flux should vary from $0.45 - 0.78 PgC/yr$. In addition, it should be noted that the uncertainty of the total net flux in Takahashi et al. (2009) is about 50%, which is due to the uncertainty of gas transfer velocity parameterization (equation 2.63), scatter of wind speed product and limited coverage of pCO_{2w}. The global pCO_{2w} has been constructed in different ways based on the scattered measurements from ship cruises. Surface Ocean CO_2 Atlas (SOCAT) database is frequently used, with the latest version comprising 28.2 million points of observations from 1957 to 2020 for the global oceans and coastal seas. Based on the SOCAT dataset, Rödenbeck et al. (2014) employed a diagnostic data-driven scheme to construct annual global pCO_{2w} distribution and analyzed the interannual anomalies of air-sea CO_2 gas exchange. Landschützer et al. (2016) employed the SOCAT data and a neural network-based data interpolation method (Landschützer et al., 2014) to estimate the decadal variations of ocean CO_2 sink. Denvil-Sommer et al. (2019) developed a new feed-forward neural network model and reconstructed the global pCO_{2w} distribution. Friedlingstein et al. (2019) systematically assessed the global carbon budget through summarizing results from multiple global models for the better understanding of global carbon cycle. The ocean uptake of CO_2 from model was underestimated compared with results based on pCO_{2w} measurements (e.g. the product of Landschützer et al. (2016)).

Chapter 3
Methodology

3.1 Introduction

In this chapter, the methodology for lab experiments (section 3.2 and 3.3) and field data processing (section 3.4) are introduced. The first experiment is conducted in a small wave flume in laboratory of the University of Melbourne (UoM). The flume has dimensions of $14m \times 0.5m \times 0.4m$ (length$\times$width$\times$water depth) with a piston wave maker at the start and a wave beach downstream. The wave maker is programmed and controlled by computer to generate monochromatic waves. To measure CO_2 concentration in water, significant effort is made to install a detection system for CO_2 partial pressure and total dissolved inorganic carbon (DIC). The system is successfully installed and validated in laboratory and used for a preliminary experiments on CO_2 transfer with wave breaking. Although the experiment is stopped after several measurements, the results are still encouraging and the framework is used for later experiments in the big wave flume. The section 3.2 details the system setup and validation, wave breaking generation and data analysis procedures.

The second experiment is conducted in laboratory of First Institute of Oceanography (FIO) in China. The wave flume is 45 m long, 1.8 m high and 1 m wide with water depth of 1.2 m in the experiment. Various situations of wave breaking (monochromatic wave breaking, wind forced wave breaking, monochromatic waves superimposed with wind) are generated with synchronized measurements of CO_2 concentration. The experimental setup inherits the framework of the former experiment in the small wave tank in UoM. With the bulk measurements in the wave flume, the dependence of CO_2 transfer rate on wave breaking is revealed. The detailed experimental setup and data processing are outlined in section 3.3.

After the laboratory experiments, field observations from ship campaigns are employed to validate and improve the formula of gas transfer velocity developed in laboratory. Observational data sets from four field campaigns at different locations of ocean are used, including High Wind Speed Gas Exchange Study (HIWINGS) in 2013, Southern Ocean Gas Exchange experiment (SOGASEX) in 2008, CAPRICORN project in 2016 and DYNAMO project in 2011. The four campaigns are carried out in separate seas which are north Atlantic Ocean (HIWINGS), Southern Ocean (SOGASEX, CAPRICORN) and tropical Indian Ocean (DYNAMO), respectively. Detailed information about the campaigns and data processing are introduced in section 3.4.

3.2 CO_2 gas transfer with wave breaking in the small wave tank

3.2.1 CO_2 detection system setup and validation

Equation 2.56 is to be used to calculate CO_2 gas exchange rate in our experiment. Therefore, DIC and partial pressure of the carbonate system in fresh water need to be measured. With the development of CO_2 monitors, CO_2 concentration in air can be measured with high precision and frequency (e.g. Licor series, Picarro). For dissolved CO_2 in water, some models are designed (e.g. CO_2-PRO, TOC-V-CSH) to measure partial pressure or DIC. Based on the previous studies (Schuster et al., 2009; Bandstra et al., 2006; Hales et al., 2004), a programmed gas-water equilibration system is installed to automaticly measure CO_2 partial pressure and DIC alternatively. A contactor (model G541 by Liqui-cel Corp.) with hollow fiber membrane inside is used to degas sample water in the system. Within the contactor, lumenside (inner of hollow fiber membrane) and shellside are divided by gas-permeable membrane which only allows gas (CO_2, water vapor, Nitrogen) molecules to go through. In the experiment, water sample is pumped into lumenside and get equilibrium with circulated air through shellside, and the equilibrated gas is monitored by CO_2 detector Picarro (model G2301). The stabilized Picarro measurements of equilibrated gas sample represent the CO_2 partial pressure in water. For DIC measurement, small amount of hydrochloric acid (HCl) is added into water sample to change water pH so that the (bi)carbonate ions are converted into dissolved gaseous CO_2 (see section 2.2.1).

The Picarro used in our experiments is a greenhouse gas analyzer with high precision ($<$ $0.15 ppm$ for 5 seconds average). It is characterized with Cavity Ring-Down Spectroscopy (CRDS)

technology which is capable of measuring CO_2, CH_4, water vapor with parts-per-billion sensitivity and low drift. It also incorporates temperature and pressure control as well as the correction of water vapor in measuring CO_2. Its operating range for CO_2 is 1-1000 ppm (highest precision at 300-500 ppm) with measurement interval of 5 seconds. It needs to be calibrated with standard gases of varied CO_2 concentration before experiment.

In the CO_2 detection system, water and air samples are delivered by using pumps. In addition, solenoid valves are installed to control water and gas flow direction. To run the system automatically, Arduino-based electrical circuit is designed and programmed to control the running of pumps and valves. The sketch of pipeline structure is shown in figure 3.1. The water flow starts

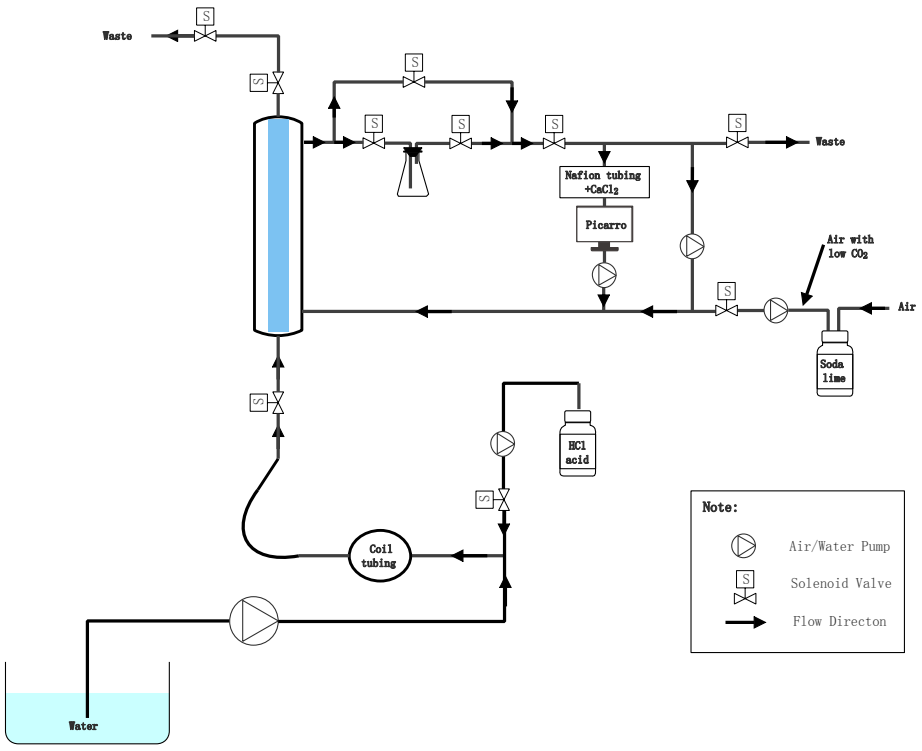

Figure 3.1: Pipeline structure of CO_2 detection system for the experiment in small wave tank.

from the wave tank at bottom left of sketch and forced by a water pump. The water sample is directly delivered to the coil tubing (for partial pressure measurement) or mixed with HCl acid first (for DIC measurement). The coil tubing ensures the fully mixing of acid and water sample.

The pH of water after mixing with HCl acid is controlled around 3 to ensure that the carbon ions are converted into dissolved aqueous CO_2 (see figure 2.1). The solenoid valves at two ends of the contactor are controlled to be open until enough water sample filled the lumenside volume (70 ml). Meanwhile, the devices at right side of figure 3.1 start by drawing air in through soda lime. Most of the CO_2 in air sample is captured by soda lime which is necessary for generating background gas with low CO_2 content for Picarro. Lim et al. (2017) conducted experiments on measuring CO_2 using Picarro and Licor series detectors. They found that background gas affects the accuracy of of Picarro, that is, the air which is mainly the mix of Nitrogen and Oxygen is suitable for Picarro while Nitrogen only as background gas causes deviation of CO_2 measurement. Hence, the air with most CO_2 removed is used as background gas in our experiment. The air flow is then delivered into the shellside (140 ml) of the contactor for the equilibrium between water and air. There are two pipelines connected to the shellside outlet of the contactor. The upper line is used for partial pressure measurement and the lower line with a flask is used for DIC measurement. The purpose of the design of using flask is to increase volume so that the CO_2 concentration could be "diluted" because equilibrated gas samples for DIC contain much CO_2 and is out of guaranteed range of Picarro. Picarro is equipped with an air pump and installed together with a drying section composed of nafion tubing and Calcium Chloride. The characteristic of nafion tubing is the penetration of water vapor only so that gas sample is dried before going to Picarro. Although water vapor correction is integrated in Picarro, vapor in the gas stream still influence the accuracy (Chen et al., 2010) and the bias can be limited by installing a drying section. At the right of Picarro, an air pump in another pipeline runs in parallel which is used to speed up the mixing of gas in the system. At the top of contactor, the wasted water sample is delivered out after each measurement.

Running procedures

To illustrate the running procedures, a simplified sketch with flow direction for air and water is presented in figure 3.2. For CO_2 partial pressure measurement,

1. The background gas (air with low CO_2 content) is inhaled into gas pipelines and room B (shellside) of contactor in figure 3.2. Then the inlet and outlet of gas pipelines (denoted as red crosses on gas tubing) are locked by valves so that the air is circulated among room B, Picarro and the air pump. The Picarro is used to observe CO_2 concentration continuously

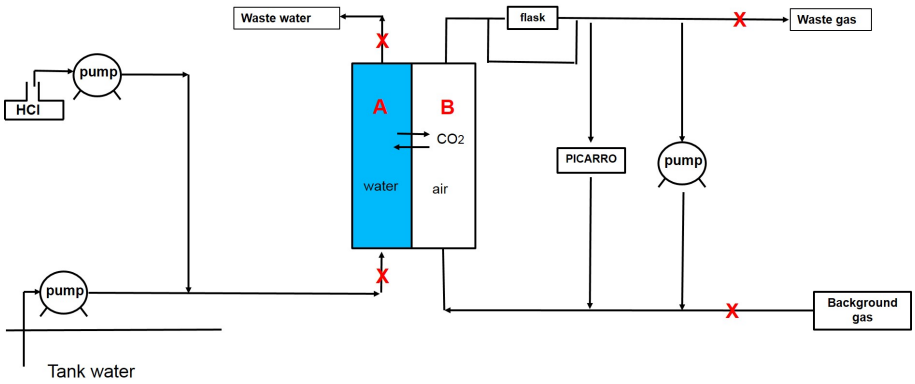

Figure 3.2: Simplified sketch of CO_2 measuring system

while the air pump works to promote air mixing. After about two minutes when the air is well mixed, CO_2 concentration detected by Picarro in closed air loop will stabilize and is measured as C_{a1}.

2. Proper amount of water sample with unknown CO_2 concentration (C_w) is delivered into room A (lumenside) of contactor in 3.5 seconds and then locked by valves. The equilibrium of water and air samples is gradually reached with the running of air mixing pump.

3. Three minutes is usually enough for the equilibrium. The stabilized CO_2 concentration is again measured by Picarro as C_{a2}.

4. In the end, water sample is emitted out. Room A is rinsed 3 times with fresh water in preparation for next measurement. The gas in the room B and other tubing is also discharged.

For DIC, the procedures are similar with partial pressure measurement except that

1. Water sample is acidified before being delivered into room A.

2. A 2-liter flask is connected in the air loop. This setup is based on the fact that about 3 times more CO_2 is generated in DIC measurement than the CO_2 amount for partial pressure experiment. Considering the guaranteed range of Picarro, extra space in the closed air loop can dilute CO_2 concentration.

A record of Picarro for one measurement of partial pressure is shown in figure 3.3. The blue curves in the red boxes denote the stabilized concentration which are C_{a1} and C_{a2}, respectively. At

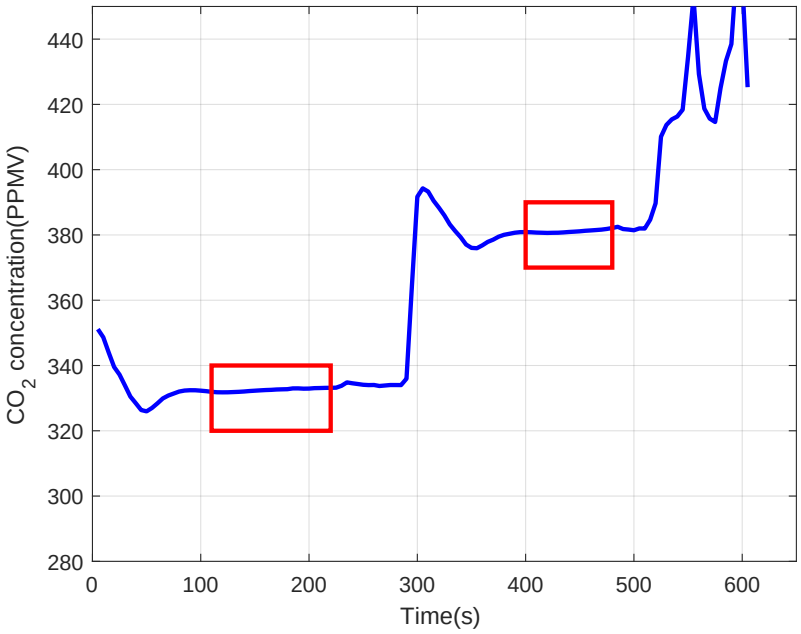

Figure 3.3: One measurement by Picarro in experiment.

the moment of equilibrium, the state of CO_2 in water and air follows Henry's law (Henry, 1803) which is

$$\frac{C_w}{C_a} = H \tag{3.1}$$

where H is nondimentional Henry's law parameter, C_w and C_a are gas concentration in water and air, respectively. In this experiment, the equation is adapted as

$$\frac{C_w + \frac{\Delta C_a}{V_{con}} \times \frac{V_a}{V_w}}{\frac{C_{a2}}{V_{con}}} = H \tag{3.2}$$

where C_w $(mol \cdot m^{-3})$ is unknown original CO_2 concentration in water sample. ΔC_a (ppm) is equal to $C_{a1} - C_{a2}$. V_{con} is the constant volume for gas under certain temperature and pressure(e.g. 25 ^oC, 101kpa). $V_{con} = R(T + 273.15)/P$, R is the gas constant (8.3144598 $J \cdot mol^{-1} \cdot K^{-1}$), T is temperature, P is pressure. V_a is the volume for air loop including space of contactor (room B), tubing, Picarro and pumps. V_w is the volume of room A (70 ml) in contactor. H can be computed as

$$H = H_{CO_2} R(T_w + 273.15) \tag{3.3}$$

where H_{CO_2} is Henry's law constant for which 3.4×10^{-4} is adopted in this research (Sander, 2015).

Validation of CO_2 detection system

In equation 3.2, C_{a1}, C_{a2}, V_{con}, V_w and H can be directly measured or computed. But V_a can not be directly estimated because the volumes of Picarro and pumps in the air loop are unknown. Thus, experiments which go through the procedure for partial pressure measurement are conducted to quantify V_a. The equation 3.2 can be simplified as,

$$C_w A + \frac{V_a}{V_w} \cdot B = H \tag{3.4}$$

where A and B represent the combination of the known parameters. To do the experiments, a bulk of fresh water is prepared and exposed to air to reach equilibrium. Another optional choice is using a bulk of sodium bicarbonate ($NaHCO_3$) solution with known concentration. By measuring the partial pressure of the fresh water (no gas exchange) for multiple times, parameters A, B and H can be computed through Picarro records and linearly fitted to produce the unknown value of $\frac{V_a}{V_w}$ and C_w. The computed parameters A and B are shown in figure 3.4 together with the coefficient

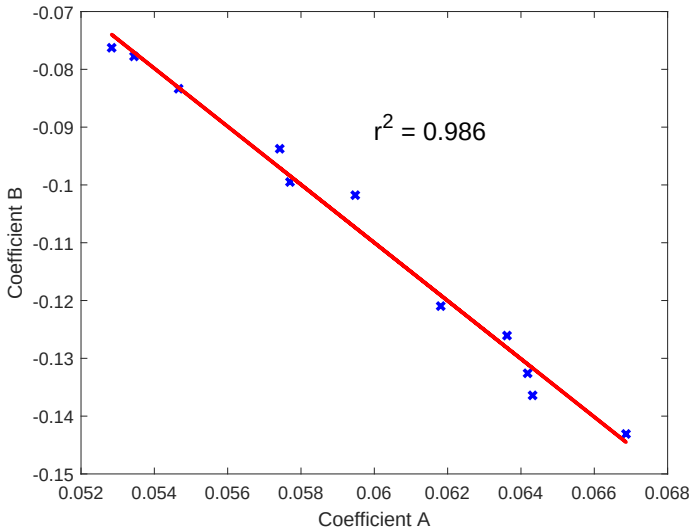

Figure 3.4: Distribution of parameters A and B based on measurement

of determination (r^2). We report that V_a for partial pressure experiment is 309.5 ml while V_a is

2909.5 ml for DIC measurement considering the connection of the flask.

In order to test the precision and accuracy of the system, calibration is carried out using gravimetrically prepared $NaHCO_3$ solution. $NaHCO_3$ powder is mixed with MilliQ water which originally contains no carbon in it. Therefore, the $NaHCO_3$ concentration is precisely controlled. Moreover, before using the solution, nitrogen gas is pumped through the solution for 2 hours to remove possibly dissolved CO_2 during the manufacturing of $NaHCO_3$ solution. Following the procedure of measuring DIC, $NaHCO_3$ is mixed with HCl and release CO_2. The measured $NaHCO_3$ concentrations using equation 3.4 are compared with the reference values obtained through gravimetric analysis in table 3.1. The results of two tests agreed well with theoretical

	Test 1 ($\mu mol/L$)	Test 2 ($\mu mol/L$)
Gravimetric analysis	254.1	244.4
CO_2 system	256.6	244.5

Table 3.1: Comparison of the measured $NaHCO_3$ concentrations by the CO_2 system and gravimetric analysis

values. Further experiments with a bulk of $NaHCO_3$ solution (355.1mg $NaHCO_3$ powder mixed with 18 liters of water) is conducted. The theoretical carbonate concentration is 221.43 $\mu mol/l$ and the mean of measurements is 218.04 $\mu mol/l$ with root mean square error (rmse) of 4.72 $\mu mol/l$. The deviation of the measurement is about 2%, showing that the CO_2 detection system is robust enough for our experiments.

3.2.2 Experimental setup

The preliminary experiment on CO_2 exchange is conducted by generating monochromatic waves in a small wave flume in laboratory of the University of Melbourne. The experimental setup is demonstrated in figure 3.5 while the CO_2 detection system is also employed as in figure 3.1. In preparation, the tank water is saturated with CO_2 gas to ensure a CO_2 partial pressure difference between water and air. CO_2 would escape from water into air during the generation of waves. An obstacle (box with dimensions of 40 cm $\times$ 22 cm $\times$ 29 cm for length $\times$ width $\times$ height) is horizontally placed (front side faces incoming waves) inside the tank to reduce water depth so that every single incoming wave breaks here. Sinusoidal waves are generated by a piston wave

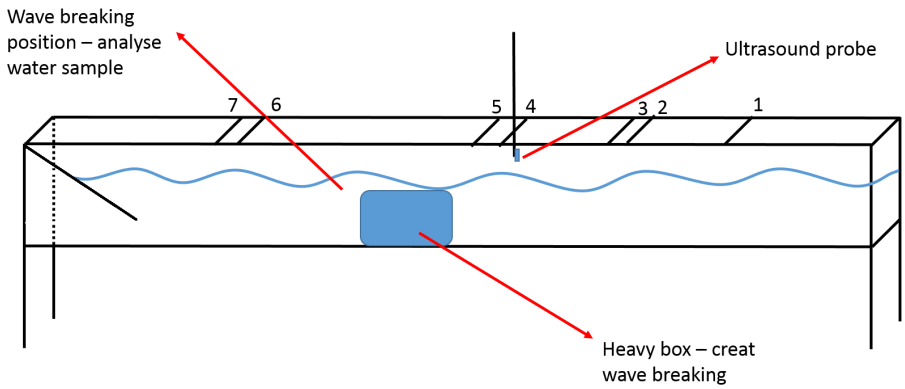

Figure 3.5: Experimental setup in the laboratory of UoM. Ultrasound probe 1 to 7 are deployed along the wave propagation. An obstacle is placed between probe 5 and 6 for an abrupt change of water depth, which induces the wave breaking.

maker. The wave signal is detected by 7 ultrasound wave probes (UltraLab ULS Advanced by General Acoustics) employed along the wave tank. The acoustic probe is able to detect the surface elevation by sending and receiving ultrasound signal. Probe 1-5 are put upstream of wave breaking position while Probe 6 and 7 are put downstream of the obstacle. Meanwhile, thermometers are used to measure air and water temperature. Two groups of experiments are conducted according to the setup of wave input. The sinusoidal waves in the first experiment have a frequency of 1.5 Hz and wave amplitude about 3 cm. When the waves pass by the obstacle, there is tiny wave breaking with few bubbles on surface. The water sampling spot for CO_2 analysis is downstream near the obstacle where the wave breaking induced turbulence and bubbles would promote gas transfer. CO_2 concentration is simultaneously measured during the generation of wave breaking. The first experiment lasts for about 1 hour. The second group of experiment is similar with the first group except that the sinusoidal waves are generated with frequency of 1.9 HZ and amplitude of about 4 cm. Both the breaking rate and breaking induced energy loss are increased. The second experiment lasts for about 2.5 hours. The results of the experiments are presented in chapter 4.

3.3 CO_2 gas transfer with wave breaking in the big wind-wave flume

3.3.1 Numerical simulation of non-linear waves

Before the experiments, numerical simulations of wave propagation is necessary since wave breaking due to modulational instability is to be generated in the flume. Chalicov-Sheinn (CS) model is used to simulate three wave trains with one-side-band perturbation. For each wave train, a sinusoidal carrier wave and one sideband are superposed. As the wave train propagates, it becomes unstable (in the modulation) and CS model will stop running when the waves break. In figure 3.6, left column denotes snapshots of 3 initial wave trains while right column denotes the last snapshots of the wave shape before breaking. It is obvious that the modulated waves become steeper and evolve to breaking state in the end.

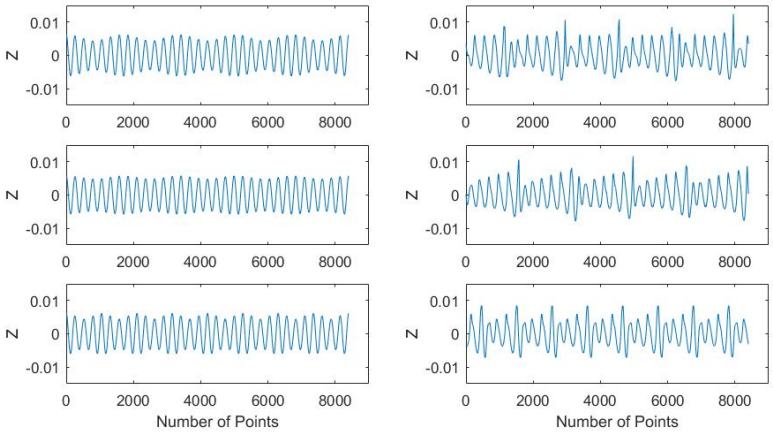

Figure 3.6: The snapshots of initial wave trains (left column) and modulated waves (right column) prior to breaking onset from the Chalicov-Sheinn (CS) model. The initial signal is composed of a sinusoidal carrier wave and a seeded sideband. The modulated waves before breaking at the right column are steep. The Z (surface elevation) and number of points (time) are non-dimensional model parameters and not comparable to dimensional values of real waves.

The initial carrier wave for the three wave trains are the same, with wave numer of 32, frequency of 1.5 HZ, steepness of 0.17. It should be noted that the numbers in the model are non-dimensional, thus they need to be transformed through factors in the model before being applied to real situation. The sideband for three wave trains and the resulted dimensional breaking distance are listed in table 3.2. The breaking distance can be predicted and controlled by changing sideband frequency and steepness. The simulations are employed to assess the wave input parameters for

laboratory experiment so that the wave breaking could happen and the breaking distance is suitable for the wave flume.

	Wave number ($/m$)	Steepness	Breaking distance (m)
1	37	0.034	21.45
2	37	0.017	31.49
3	40	0.034	17.99

Table 3.2: The sideband wave number, steepness and the resulted dimensional breaking distance for three simulations

3.3.2 Experimental setup

With the help of CS model simulation, wave input parameters are selected and tested so that the modulated wave trains start to break around a fixed position but with different breaking probability and severity.

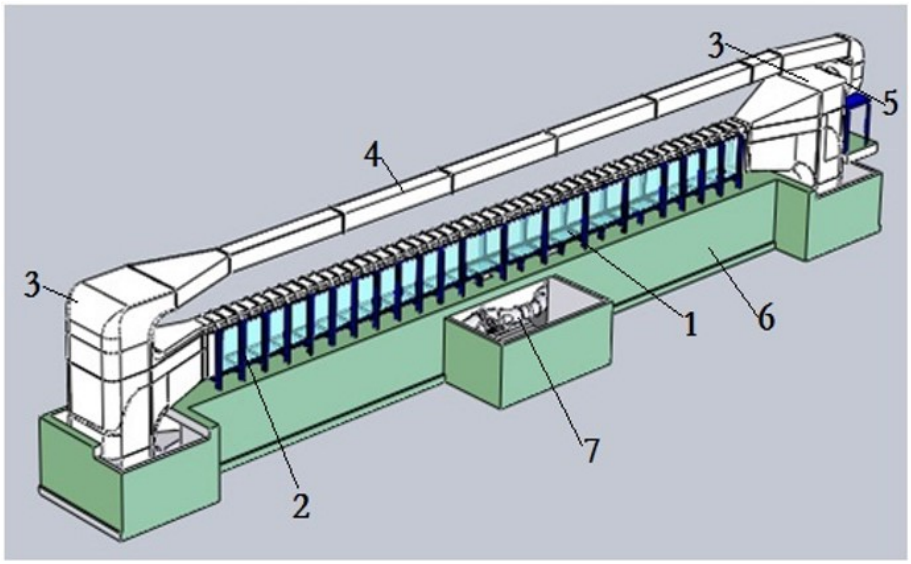

Figure 3.7: The diagram of the wind wave flume in the laboratory of FIO. 1–Glasses; 2–Wavemaker; 3–Plenum chamber; 4–Wind channel; 5–Wind fan; 6–Tank foundation; 7–Water channel.

The facility for experiments is a wind-wave flume (figure 3.7), 45 m long, 1.8 m high and 1 m wide available at First Institute of Oceanography in China. The tank is filled with tap water up to 1.2 m. The wind fan is installed above the wave tank with a closed air channel. A mechanical

wavemaker is located upstream. It is programmable and able to generate waves that are steep enough to lead to wave breaking. At the downstream end of wave tank, a beach is designed for damping wave energy (more than 95%) to prevent the reflection of waves.

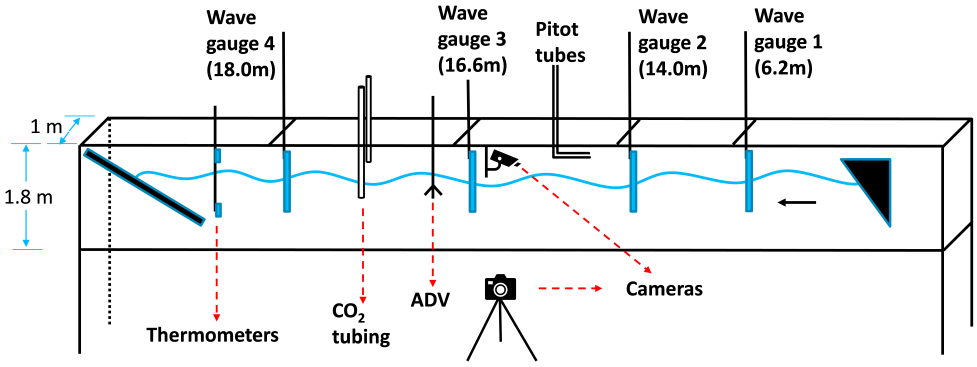

Figure 3.8: Schematic showing the deployment of probes along the wave tank. There are four resistance-type wave gauges at 6.2 m, 14.0 m, 16.6 m, 18.0 m from the wavemaker on the right. Close to wave gauge 3, a set of Pitot tubes, one ADV and sampling tubing for CO_2 analysis are installed. Outside the wave tank, a Canon camera and a video camera are used to record waves. At the downstream rear of wave tank, a pole attached with two thermometers is placed for the measurement of air and water temperature, respectively. A wave beach is installed to damp the wave energy.

Various sensors are employed along the wave tank to measure physical and chemical variables. Water surface elevation is measured by 4 resistance-type wave gauges (figure 3.8) with 50 Hz sampling rate located at 6.2 m, 14.0 m, 16.6 m and 18.0 m away from the wavemaker. A vertical array of 5 Pitot tubes is located about 10 cm before wave gauge 3 and arranged evenly (5 cm spaced) with the lowest one at about 15 cm above the free water surface. It takes 100 milliseconds for the computer to record wind speed at each tube. An acoustic Doppler velocimeter (ADV) is collocated with wave gauge 3 to measure turbulence in the water, although the data is not used in the present work. 50 cm downstream of wave gauge 3, tubing for taking water and air samples in the flume is installed, and further connected to the CO_2 analysis devices. Two thermometers are placed at the rear of wave tank for air and water temperature measurements, respectively. Air conditioners in the lab are always running during experiments so that temperature is homogeneous in the wave tank. A Canon digital camera and a video camera are employed outside the wave tank to record wave breaking processes. In addition, the water acidity index (pH) and air pressure in the lab are also recorded during the experiments. It should be mentioned that the water surface is cleaned

from potential oil film by blowing gentle wind for 5 minutes and capturing oil at downstream wave beach.

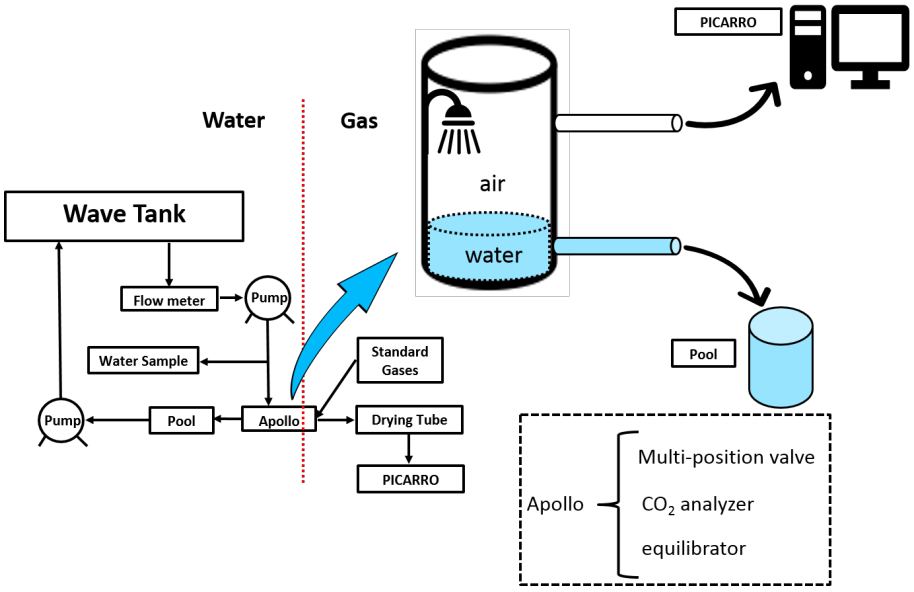

Figure 3.9: The measurement of CO_2 by Apollo system. The water sample is pumped out of tank and showered at equilibrator of Apollo in which the air and water exchange CO_2 and reach equilibrium. The equilibrated gas sample is further analyzed by Picarro. The wasted water sample is then delivered back to the end of wave tank. Multi-position valves in Apollo are switched for ambient air and gas sample measurements in Picarro alternatively. The drying section is installed to remove water vapor for Picarro. The standard gases with CO_2 concentration of 400.0 ppm, 600.7 ppm, 799.2 ppm, and 1000.6 ppm are used to calibrate Picarro.

The instrument for CO_2 analysis is the Apollo pCO_2 system (model AS-P2 by Apollo SciTech, USA) in figure 3.9, which incorporates an air-water equilibrator and Picarro G2301 CO_2 analyzer with high precision($< 0.15ppm$ and $< 0.05ppm$ for 5-second and 5-minute measurement, respectively). Water is delivered at a rate of 2.5 L/min into equilibrator to contact with air stream. After reaching equilibrium, the water is returned to the rear of tank and the equilibrated gas is analyzed by Picarro as the water side partial pressure pCO_{2w}. The multi-position valve on Apollo is set up so that Picarro could analyze equilibrated gas samples and ambient air in lab alternatively. Meanwhile, Apollo is programmed to collect data of both pCO_{2w} and pCO_{2a} from Picarro. An air dryer is installed to remove water vapor in the gas stream before going to Picarro. Standard gases with CO_2 concentration of 400.0 ppm, 600.7 ppm, 799.2 ppm, and 1000.6 ppm are used to calibrate Picarro analyzer. In the flume, an air-water pCO_2 gradient is created to ensure the

evasion of CO_2 from water into air for all the experiments. Figure 3.10 shows the measurements

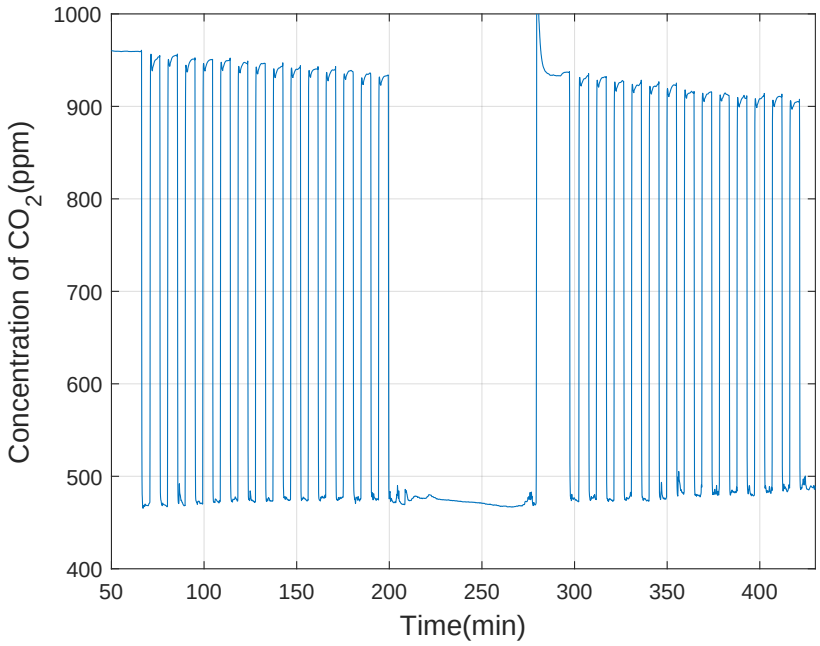

Figure 3.10: The measurements of air and water side CO_2 concentration in two groups of experiments from Picarro in Apollo system. The upper envelope represents the measurements of CO_2 concentration in equilibrated gas samples, i.e. the level of water side CO_2 partial pressure. The bottom envelope represents the CO_2 concentration in air samples in the wind-wave flume. The total time length for one group of experiment is about 2 hours comprising segments of CO_2 measurements in water and air.

of Picarro in two groups of experiments. In each experiment, the total time length is about 2 hours. The measurement of CO_2 concentration in air and water costs about 10 minutes for one cycle. The upper envelope of measurements is the CO_2 concentration in equilibrated gas samples, i.e. the level of water side CO_2 partial pressure. CO_2 concentration in water is always decreasing because of the evasion of CO_2 from water into air. The bottom envelope denotes the air side CO_2 concentration in the wind-wave flume. Wind tunnel in the experiments is not completely sealed so that the air side CO_2 change is not evident. The CO_2 measurements are used for the computation of gas flux and transfer rate.

Case No.	f_0 (Hz)	a_0 (m)	ε_0	f_+ (Hz)	a_+ (m)	BFI	f_{fan} (Hz)	U_{10} (m/s)	H_b (m)	U_{wb} (m/s)	b_T	U_{wm} (m/s)	H_s (m)	K_{600} $(10^{-6}m/s)$
A1	1.2	0.035	0.20	1.32	0.010	0.95	0	0	0.15	0.60	0.092	0.32	0.13	1.065
A2	1.2	0.052	0.30	1.33	0.006	1.36	0	0	0.18	0.70	0.103	0.48	0.19	1.386
A3	1.0	0.050	0.20	1.10	0.024	0.95	0	0	0.25	0.82	0.073	0.40	0.19	1.280
A4	1.3	0.029	0.20	1.43	0.007	0.95	0	0	0.10	0.36	0.101	0.30	0.12	0.748
A5	1.1	0.041	0.20	1.21	0.014	0.95	0	0	0.23	0.81	0.090	0.35	0.16	1.492
A6	0.9	0.061	0.20	1.04	0.035	0.60	0	0	0.30	0.90	0.069	0.43	0.22	1.713
A7	1.1	0.033	0.16	1.24	0.019	0.59	0	0	0.15	0.53	0.111	0.31	0.14	1.206
A8	1.1	0.051	0.25	1.24	0.014	0.94	0	0	0.20	0.72	0.111	0.42	0.19	1.396
A9	1.0	0.055	0.22	1.11	0.023	0.95	0	0	0.24	0.76	0.098	0.42	0.20	1.663
A10	0.9	0.055	0.18	1.02	0.039	0.61	0	0	0.29	0.87	0.120	0.40	0.21	2.946
B1	0.9	0.055	0.18	1.02	0.039	—	25	11.21	0.29	0.85	0.121	0.46	0.24	4.790
B2	0.9	0.055	0.18	1.02	0.039	—	15	6.77	0.28	0.82	0.122	0.42	0.22	1.946
B3	1.1	0.041	0.20	1.21	0.014	—	20	9.14	0.20	0.74	0.087	0.40	0.18	2.997
B4	1.1	0.041	0.20	1.21	0.014	—	30	13.43	0.24	0.88	0.086	0.52	0.22	4.101
B5	1.0	0.055	0.22	1.11	0.023	—	20	8.85	0.26	0.86	0.098	0.46	0.22	3.898
B6	1.0	0.055	0.22	1.11	0.023	—	30	13.43	0.27	0.88	0.096	0.55	0.25	6.974
C1	—	—	—	—	—	—	10	4.46	0.02	0.21	0.239	0.15	0.02	0.092
C2	—	—	—	—	—	—	15	6.88	0.03	0.29	0.371	0.22	0.04	0.280
C3	—	—	—	—	—	—	20	9.19	0.04	0.34	0.488	0.27	0.05	0.670
C4	—	—	—	—	—	—	25	11.12	0.05	0.38	0.559	0.31	0.07	0.999
C5	—	—	—	—	—	—	30	13.25	0.07	0.44	0.665	0.39	0.09	—
C6	—	—	—	—	—	—	35	15.44	0.09	0.51	0.732	0.45	0.12	2.743

Table 3.3: Experimental parameters of all cases. A1 to A10 are the monochromatic wave experiments with mechanically-generated waves. B1 to B6 are the coupled wave experiments (mechanically-generated waves superimposed with wind). C1 to C6 represent the experiments with wind forced waves.

3.3.3 Data processing

The experimental parameters are listed in table 3.3. In case A1-A10, wave packets generated by a wavemaker are unstable (Banner et al., 2000) and set to break after passing wave gauge 2. Based on A10, A5 and A9, the same mechanically-generated waves are superimposed with different wind forcing in B1-B6, in order to compare with A cases in terms of wave breaking and the resulted gas transfer rate. Case C1-C6 have the waves forced by wind only. The initial wave signal of mechanical waves in A1-B6 is the combination of a carrier sinusoidal wave with frequency f_0, amplitude a_0, wave number $k_0 = (2\pi f_0)^2/g$, where g is gravitational acceleration, steepness $\varepsilon_0 = a_0 k_0$, and a resonant sideband with frequency f_+, amplitude a_+ (10% to 30% with respect to a_0). The Benjamin-Feir Index (BFI) is used to evaluate the instability of wave trains. $BFI = \varepsilon_0/(\Delta k/k_0)$, where Δk is the wave number difference between carrier wave and sideband. An example of modulation of wave groups in experiment A1 at wave gauge 1-4 is showed from top to bottom in figure 3.11. The wave signal at wave gauge 2 is significantly modulated compared with wave form at gauge 1. The steep waves propagating after wave gauge 2 tend to break before gauge 3 where the breaking events are recorded by videos.

The wind fan frequency (f_{fan} in table 3.3) in B1-C6 is set up beween 10 Hz to 35 Hz for varied wind forcing. The drag coefficient c_d is computed to be 0.0013 for case C6 with a clear logarithmic wind profile. Because a wind-dependent c_d has very slight influence on the coefficients of final formulae, constant c_d (=0.0013) is used here to correct the wind speed to 10-meter reference (U_{10}) and to compute wind friction velocity. Because an evident decrease of the wave height after the breaking can be observed, the records of wave gauge 3 and 4 are used to recognize the breakers after shifting the time frame of each measurement. An example of identified breakers in experiment A1 is showed in figure 3.12. The steep wave crest breaks at gauge 3 (star on red line) and losts much of its energy when reaches gauge 4 (green line). The video records of the wave breaking situation at gauge 3 are also employed to validate the recognition of breakers. By choosing the breaking events that happened upstream nearest the CO_2 sampling tubing, the mean wave height of the breakers (H_b) measured at wave gauge 3, before the breaking, is used as the proxy of wave height of the breaking onset. Similarly, mean orbital velocity of the breakers (U_{wb}) is computed following the linear wave theory. For young wind waves (C1-C6), the breaking events are identified by using the criterion for ultimate steepness ($\varepsilon \leq 0.44$) of individual waves subject to

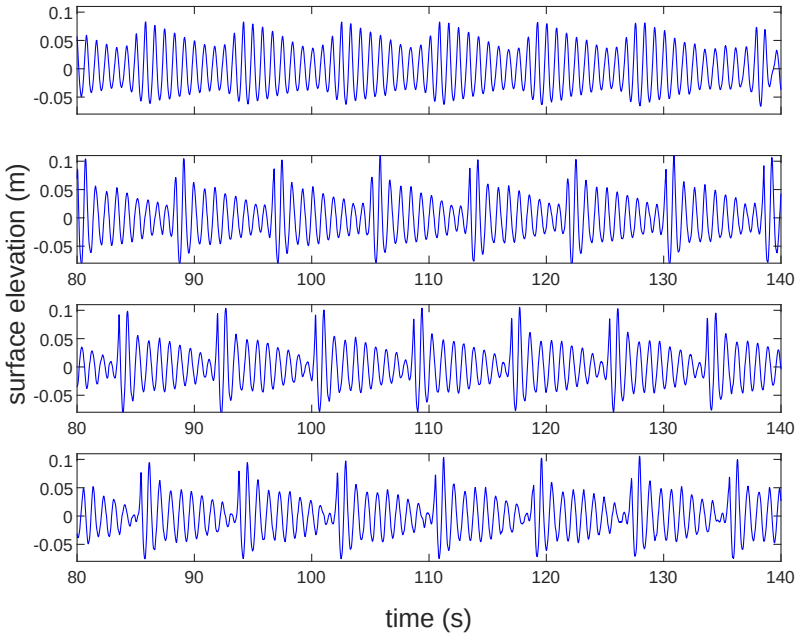

Figure 3.11: Surface elevation measured by wave gauge 1-4 (top panel to bottom panel) in experiment A1. The wave group modulate itself along the wave propagation and waves with high steepness tend to break around wave gauge 3.

modulational instability (Babanin et al., 2007, 2010). Breaking probability (b_T) is then estimated based on the proportion of breakers. Significant wave height H_s and mean orbital velocity U_{wm} of all waves at wave gauge 3 are also computed. Plunging or spilling breakers are observed for mechanically-generated waves in A1-B6. For fetch-limited wind waves in C1-C6, the transition from small breakers without bubble injection to breakers with bubbles are observed when the wind speed varies from low to high.

The method to calculate gas transfer rate K_{CO_2}, following Ocampo-Torres et al. (1994), is adopted in our work:

$$\frac{\partial C_g}{\partial t}\frac{V_w}{A} = -K_{CO_2}(C_g - C_a), \tag{3.5}$$

where C_g and C_a are CO_2 concentration detected by Picarro in equilibrated gas and in air, respectively. Here, V_w and A refer to the water volume and surface area that are involved with the gas exchange process. So V_w/A identifies the height of water column, which is related to the depth of turbulent mixing layer. Thomson et al. (2016) suggested that the turbulence could be transported down to wave trough due to orbital motion, and in our work the depth of upper mixing layer is

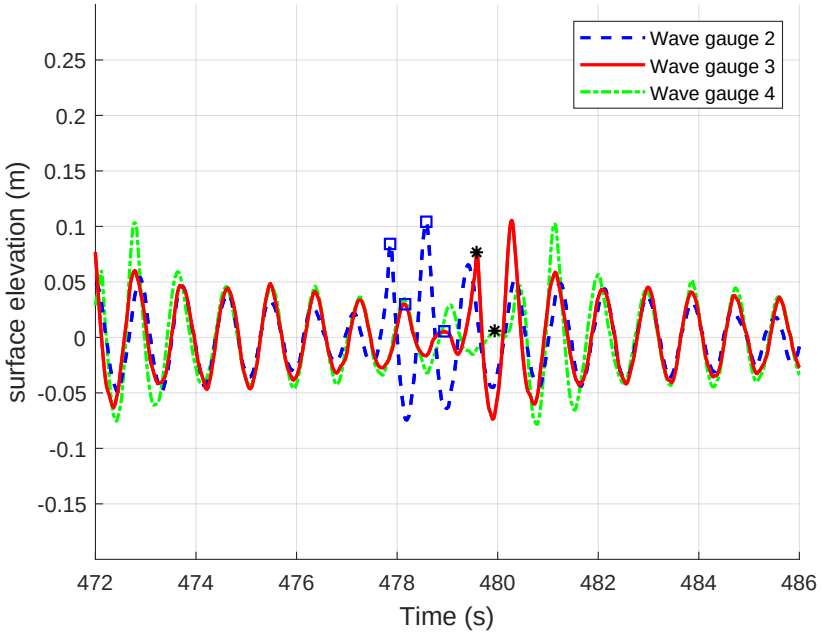

Figure 3.12: Breaking waves identified by comparing measurements between wave gauges after shifting the time frame of each measurement. The wave crest marked with star on the red line (wave gauge 3) is the breaker near CO_2 sampling position. The feature of breakers around wave gauge 3 is used to correlate with gas exchange rate.

scaled with H_b. The calculated K_{CO_2} is further corrected to 20^oC of fresh water with Schmidt number $Sc_{600} = 600$ in order to eliminate the thermal effect on gas transfer.

$$\frac{K_{CO_2}}{K_{600}} = \left(\frac{Sc_{co_2}}{Sc_{600}}\right)^{-0.5} \tag{3.6}$$

where K_{600} represents the corrected transfer velocity in table 3.3, Sc_{co_2} is the Schmidt number of water in laboratory. The power of Sc is empirically determined to be -0.5 for wavy surface (Jähne et al., 1987). The results of experiments are discussed in chapter 4.

3.4 Field projects on CO_2 gas exchange

3.4.1 Introduction of field campaigns

Project CAPRICORN is part of Voyage IN2016_V02 on RV Investigator from 14 March to 16 April, 2016 in Southern Ocean. The track of the cruise is showed in figure 3.13(a). The whole project is conducted by several organizations including the Commonwealth Scientific and Industrial Research Organization (CSIRO), Bureau of Meteorology (BOM) and the University of Tasmania (UTAS). The Southern Ocean is one of the key research regions in the global climate system by soaking up atmospheric CO_2 and affecting global air-sea heat fluxes. Thus, enhanced understanding of the dynamic processes occurring in this region related with ocean mixing, waves, gas exchange, clouds is essential for assessment of climate variability. The whole voyage provides an integrated view that covers ocean mixing physics, chemistry of ocean nutrients and biological production. The project CAPRICORN aims to improve our knowledge of the regional atmospheric system and ocean surface energy budget in order to upgrade the estimations of those physical properties from satellite and global models. The air-sea CO_2 flux during the cruise is obtained through eddy covariance method as introduced in section 2.3.3 by measuring atmospheric CO_2 via Licor-7500 NDIR analyzer. The air and water side CO_2 partial pressure are also measured by Picarro (model g2301) analyzer and equilibrator system, respectively. The wind, waves and other meteorological parameters used in this study are recorded simultaneously by various sensors as in table 3.4.

System	Measurement	Sampling frequency
Sonic anemometer	3-axis velocity	10 HZ
SCS	sea, P_{CO_2}, and ship met data	1/5s
Ship motion system	ship acceleration, rotation, roll, pitch, yaw	10 HZ
Temperature, Pressure, Humidity sensors	SST, air temperature, pressure, RH	1/min
GPS	ship location and speed components	1 HZ
Open path NDIR (Licor-7500)	CO_2, vapor	10 HZ
Close path CRDS (PICARRO)	CO_2, vapor	1/5s
Lidar wave altimeter	wave height	10 HZ

Table 3.4: The systems and measurement of parameters in the project Capricorn 2016

The High Wind Gas Exchange Study (HIWINGS) (figure 3.13(b)) is conducted on RV Knorr at Labrador Sea from 10 October to 14 November in 2013. The campaign is conceived to investigate air-sea interaction at high wind speeds including gas, heat, momentum transfer. The international cooperative teams successfully deployed direct measurements of trace gas ($CO2$ and

DMS) fluxes with environmental sea state observations. The region at that period is subject to high wind speeds, frequent storms and a well-known sink for atmospheric $CO2$ with large air-sea partial pressure gradient. The observations of wind-sea state and gas exchange at boundary layer during storms are accomplished by choosing optimal positions. More detailed information for measurements, instruments and operations during the project can be referred to previous publications (Blomquist et al., 2017; Brumer et al., 2017b). In this study, the CO_2 hourly gas transfer rate provided by Blomquist et al. (2017) is utilized for further analysis.

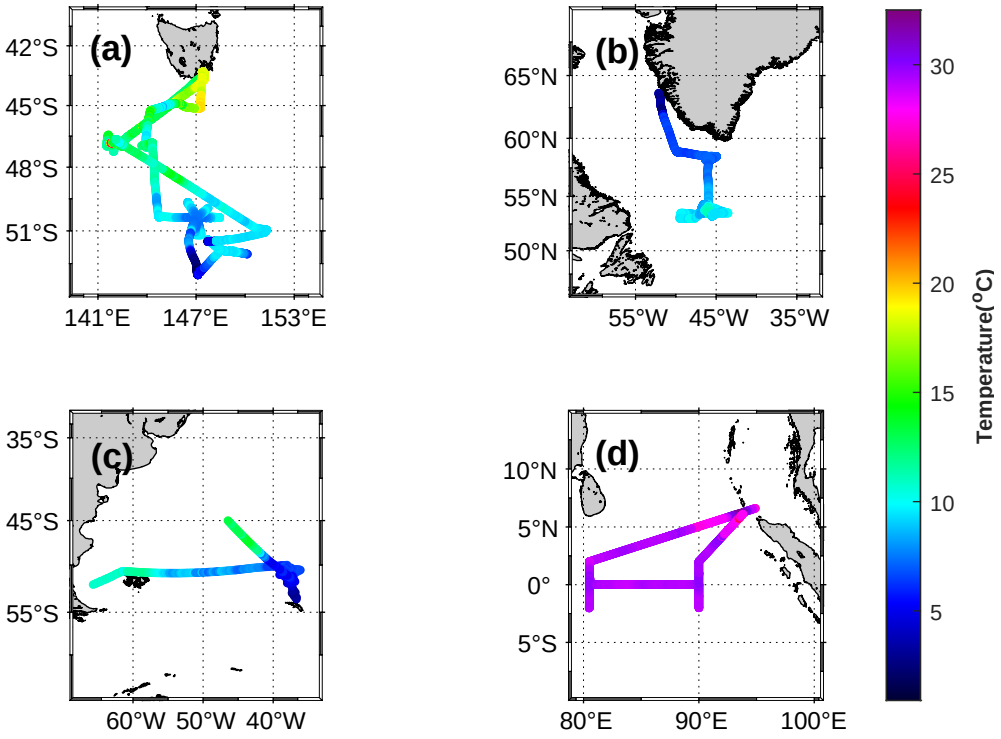

Figure 3.13: Map of four field campaigns and SST along the tracks. (a) The track for CAPRICORN 2016 in Southern Ocean close to Australia. (b) The cruise of HIWINGS 2013 in north Atlantic ocean. (c) The SOGASEX 2008 in Southern ocean near South America. (d) The cruise of DYNAMO 2011 in equatorial Indian Ocean.

The Southern Ocean Gas Experiment (SOGASEX) is conducted at Southern Ocean during February to April in 2008 on board of the NOAA ship Ronald H. Brown (RHB) with cooperation of multiple institutions and labs. The cruise is designed to investigate gas transfer ($CO2$ and

DMS) and heat fluxes which are controlled by physical, chemical and biological processes at boundary layer. The region (figure 3.13(c)) is selected for large air-sea $CO2$ partial pressure difference to ensure a large enough signal-to-noise ratio with representative wind speeds and waves of the Southern Ocean. The measurements of marine parameters and deploy of instruments are introduced in Edson et al. (2011). The CO_2 transfer rate of the campaign obtained from previous researches (Edson et al., 2011; Brumer et al., 2017a) is used in the present work.

System	Measurement	Sampling frequency
Sonic anemometer	3-axis velocity	10 HZ
SCS	sea, and ship met data	1 HZ
Ship motion system	ship acceleration, rotation, roll, pitch, yaw	10 HZ
Temperature, Pressure, Humidity sensors	SST, air temperature, pressure, RH	1/min
GPS	ship location and speed components	10 HZ
Open path NDIR (Licor-7500)	CO_2, water vapor	10 HZ
Close path NDIR (Licor-7200)	CO_2, water vapor	10 HZ
CO_2 equilibrator system	Underway sea surface P_{CO_2}	1/10 min
Lidar wave altimeter	wave height	10 HZ

Table 3.5: Measurements and systems in the project DYNAMO in 2011

DYNAMO program (figure 3.13(d)) is conducted in tropical Indian Ocean between 2011-2012 with the motivation to advance the understanding of global climate change related with Madden Julian Oscillation (MJO). Comprehensive parameters in the ocean and atmosphere are measured and the data used in this study are listed in table 3.5. In this region, ocean is the source for atmospheric CO_2 with high SST. Air-sea CO_2 flux is estimated by using Licor-7500 measurements in the present work. Abundant previous publications (e.g. Blomquist et al., 2014; De Szoeke et al., 2015) detailed the operation and achievements.

The tracks of the four cruises cover different oceans with varied SST and source/sink for air-sea gas fluxes. In the present study, the CO_2 gas fluxes for project CAPRICORN and DYNAMO are calculated by using Licor-7500 data. With air-sea CO_2 partial pressure, the gas transfer velocity can be estimated. The bulk meteorological data and ocean wave measurements of the four campaigns are also processed. The combined data sets will be used to validate our parameterization developed in laboratory.

3.4.2 Field data processing

The observational data sets from the four field campaigns are corrected and averaged in this section. All the measurements related with meteorology (atmospheric pressure, humidity, tempera-

ture), ocean (surface elevation, SST, salinity), and CO_2 gas exchange (CO_2 partial pressure, water vapor) need to be corrected for various interferences, such as the impact of ship motion (roll, pitch and heave). Moreover, the data with different frequencies are averaged to 10-minute segments. The CO_2 records are averaged with 50% overlap (5 minutes) yielding 11 pieces in one hour. The gas transfer velocity, wave breaking probability, wind-sea Reynolds number and wind speed are computed after the measurements being corrected. Eventually, the 10-minute segments are averaged for hourly results to reduce the variability.

Determination of air-sea CO_2 transfer

Eddy Covariance method is a direct and reliable way to estimate air-sea gas flux (Wanninkhof et al., 2009) which is introduced in section 2.3.3. The CO_2 flux (F_c) can be expressed as,

$$F_c = \overline{\rho_a} \cdot \overline{w'c'} \tag{3.7}$$

where w is vertical component of wind speed, c is CO_2 mixing ratio in air, ρ_a is the dry air density. The prime denotes the fluctuations of parameters. The over bar means the average of parameters. The CO_2 analyzers Licor-7500, Licor-7200 and Picarro can provide high frequency CO_2 measurement in air which can be used to estimate CO_2 fluxes. However, different procedures to analyze the data are implemented according to the varied instruments. Licor-7500 is an open path analyzer which is deployed outside of the lab (e.g. starboard) together with sonic anemometer for wind speed on ship and can provide direct measurements of fluctuations of sea surface CO_2. Despite the advantage, quality of Licor-7500 data suffers from the impact of severe ocean environment and water vapor cross talk due to the contamination of optical part of the device in the direct exposure to the atmosphere over ocean. Licor-7200 and Picarro are close path analyzers which are allocated inside of the lab on ship and take samples from outside through tubes. The signals from close path analyzers are usually stable and clean with the installation of water vapor filter. However, the problems such as time lag and spectral attenuation (loss of high frequency) still exist for close path analyzers. Another difference between the gas analyzers is that Licor-7500/7200 are both infrared gas analyzers (IRGA) while Picarro is equipped with cavity ring-down spectroscopy (CRDS) technology to elevate the precision. The CO_2 fluxes for SOGASEX and HIWINGS are

obtained from previous studies (Edson et al., 2011; Blomquist et al., 2017) through measurements of Licor-7500 and Picarro, respectively. Licor-7500 records during the project CAPRICORN and DYNAMO are processed for gas flux estimation in the present work.

CO_2 analyzer fixed on the ship is sensitive to the ship motion such as roll and pitch. Hence, the measurements comprise the motion interference. There are multiple ways from previous studies (McGillis et al., 2004; Prytherch et al., 2010b; Edson et al., 2011) to correct the platform motion interference. For the IRGA data, the linear regression approach is effective (Blomquist et al., 2014) by eliminating the correlation between c' and residual ship motion with respect to 3-axis platform velocity and acceleration.

The water vapor in gas sample which is analyzed in the IRGA cause dilution effects resulting in underestimated CO_2 concentration. Open path IRGA (Licor-7500) can be substantially affected in the moist air while close path analyzers (Licor-7200, Picarro) installed with drying section are barely influenced by moisture. The water vapor measurement from Licor-7500 is corrected to the same level as specific humidity which is computed by using air temperature, pressure and relative humidity data from T/RH sensors. It should be mentioned that the atmospheric pressure data need to be corrected for ship heave movement (Miller et al., 2010). The dilution correction (Webb et al., 1980) is then applied to the Licor-7500 CO_2 data as in equation 3.8,

$$X_c = \frac{X_{raw}}{1 - \frac{q \cdot m}{m_v}} \tag{3.8}$$

where X_c and X_{raw} are mass concentration of CO_2 given as mole fraction after and before correction, respectively. q is the specific humidity of water vapor, m and m_v are molecular weights of moist air and water vapor, respectively. m is computed as ,

$$m = \frac{\rho \cdot R \cdot T}{P} \tag{3.9}$$

where ρ is moist air density, R is ideal gas constant (8.314 $Pa\ m^3\ mole^{-1}\ K^{-1}$), T and P are air temperature and pressure, respectively. The equation 3.8 is further expanded into equation 3.10 considering the influence from environmental temperature and vapor (Webb et al., 1980; Miller

et al., 2010; Fairall et al., 2000).

$$F_c = \overline{w'\rho_c'} + (1+\mu\sigma)\frac{\overline{\rho_c}}{\overline{T}}\overline{w'T'} + \mu\frac{\overline{\rho_c}}{\overline{\rho_a}}\overline{w'\rho_v'} \tag{3.10}$$

where ρ_c, ρ_v and ρ_a denote density for CO_2, vapor and dry air, respectively. $\mu = M_a/M_v$ is the ratio of molecular weight of dry air and vapor, $\sigma = \rho_v/\rho_a$ is the ratio of density of vapor and dry air. The second and third term in equation 3.10 imply the corrections required with respect to temperature and water vapor interference.

The IRGA also provides real-time quality control flag (AGC) for evaluation of the degree of environmental impact (e.g. fog condensed water drops on optical devices) on the records. The data with good quality is marked with flag value under 65 while increased number indicates bigger uncertainty. Additionally, the anomalous CO_2 measurements which are out of 3 standard deviations in 10-minute segments are also filtered for subsequent corrections.

The corrections mentioned above is usually sufficient for Licor-7200 with vapor dryer. However, for Licor-7500, there is also perturbation of humidity cross-talk. The impact has been discussed in previous studies (Edson et al., 2011; Prytherch et al., 2010a) and can be solved by using so-called "PKT method" or spectral method. The PKT method in Prytherch et al. (2010a) offers a way to dynamically adjust CO_2 gradients to remove the dependence on relative humidity (RH) so that the overestimated gas flux could be corrected. On the other hand, Edson et al. (2011) provides a way to eliminate the water vapor cross-talk in the spectra and a good agreement is obtained in comparison with the results of PKT method by using a spectral correlation coefficient. In our study, PKT correction is employed to correct the Licor-7500 data.

The vertical wind speed is calculated from the observed wind components by sonic anemometer. The raw data is processed for streamline wind velocity and relative wind velocity after removing the effect of ship speed measured by GPS. With corrected CO_2 and wind speed, the gas flux can be calculated through equation 3.7. Following criteria are applied to the gas fluxes for quality control: (1) $|\Delta pCO_2|$>20ppm, (2) RH<90%, (3) relative wind direction within $\pm 75^\circ$. The first requirement for high air-sea partial pressure difference rejects the records that out of the detection limit with low signal to noise ratio. The level of 20 ppm is set up for project CAPRICORN and DYNAMO while the threshold for SOGASEX is 40 ppm by Edson et al. (2011). The second criterion filters the measurements in high humidity conditions such as fog induced condensation

and rain that may contaminate optics on instrument. The wind direction criterion removes the measurements that might be polluted by ship exhausts. The 10-minute segments of gas fluxes are further averaged to hourly mean results. For the project CAPRICORN, minimum 4 valid pieces of segments are required in one hour (total 11 pieces) to reduce the scatter.

The air-sea CO_2 partial pressure difference is obtained in laboratory on ship by using underway equilibration system. The partial pressure data is further processed to fugacity at air-sea interface through temperature and pressure difference between equilibrator and sea surface, which is discussed in Pierrot et al. (2009).

With gas flux and partial pressure, CO_2 gas transfer velocity can be computed in (3.11),

$$K_{CO_2} = \frac{F_c}{\alpha \cdot (pCO_{2w} - pCO_{2a})} \tag{3.11}$$

where α is solubility of CO_2, pCO_{2w} and pCO_{2a} are partial pressure in water and air, respectively. The calculated K_{CO_2} is further corrected to the situation of 20^oC of sea water with Schmidt number $Sc_{660} = 660$ in equation 3.12 to eliminate the thermal effect,

$$\frac{K_{CO_2}}{K_{660}} = \left(\frac{Sc_{co_2}}{Sc_{660}}\right)^{-0.5} \tag{3.12}$$

where K_{660} represents the corrected CO_2 transfer velocity, Sc_{co_2} is the Schmidt number of sea water. The magnitude of power of Sc is set to be 0.5 for wavy water surface. Schmidt number Sc is defined as the ratio of kinematic viscosity (ν) and mass diffusivity (D). Sea water viscosity is computed following the equation 22 in Sharqawy et al. (2010) and Thermodynamic Equation Of Seawater - 2010 (TEOS-10). The mass diffusivity for liquids is proportional to T/μ by using Stokes-Einstein equation, where T is temperature, μ is dynamic viscosity.

Determination of wave property

The Riegl laser altimeter is deployed during the campaigns to obtain ocean surface wave information. The altimeter is usually mounted on the jackstaff of ship at a certain height and tilt angle. The raw data comes with frequency of 10 HZ. The records are divided into 10-minute segments and piecewise interpolated to fill invalid measurements. For each 10-minute segment, it is rejected

if the number of invalid measurement points is more than 3000 or the original signal length is less than 5900 points (6000 total). Because of the tilt angle of altimeter and the interference of ship motion, the surface elevation need to be recalculated as (3.13),

$$\eta = z - L \cdot [\sin(\theta) \cdot \sin(\alpha) + \cos(\theta) \cdot \sqrt{1 - (\sin^2 \alpha - \sin^2 \varphi)}] \tag{3.13}$$

where z is the summation of Riegl height and heave of ship, L is the observed distance to surface, θ is the forward tilt of the laser altimeter, α is the pitch Euler angle and φ is the roll Euler angle. Although corrections are applied, the signal may still be out of range. Each 10-minute segment is filtered with 3.5 standard deviations.

Based on the analysis of surface elevation records, individual waves are recognized through upcrossing points with respect to the mean water surface. By employing the characteristics of wave breaking (Babanin et al., 2010; Toffoli et al., 2010), waves with steepness ϵ ($= ak$, a is wave amplitude, k is wave number) bigger than 0.44 are recognized as breakers. The breaking probability (b_T) is then estimated as the ratio of the number of breakers and all waves. Other wave parameters such as wave height and orbital velocity are computed through the analysis of 1-dimensional spectra. The significant wave height H_s is equal to $4 \cdot \sqrt{m_0}$, where m_0 is zero-order spectral moment. The mean orbital velocity T_{02} is computed as $\sqrt{m_0/m_2}$, where m_2 is second order spectral moment. Additionally, the 10-meter wind speed and wind friction velocity (including the wind gust) are obtained from COARE (version 3.5) model (Fairall et al., 2011) output in the analysis of campaign data. The wind friction velocity may be varied due to different choices of the drag coefficient. In the present work, the wind speed component in our gas transfer parameterization behaves as an enhancement factor which is much less than the dominant terms of waves. Therefore, the uncertainties of wind estimation could barely influence the results

Chapter 4

Dependence of CO_2 gas transfer on wave breaking in laboratory

4.1 CO_2 gas transfer with wave breaking in the small wave tank

Following the experimental setup in the small wave tank in section 3.2, the results are analyzed in this section. The CO_2 concentration change in water is measured, i.e. the partial pressure and

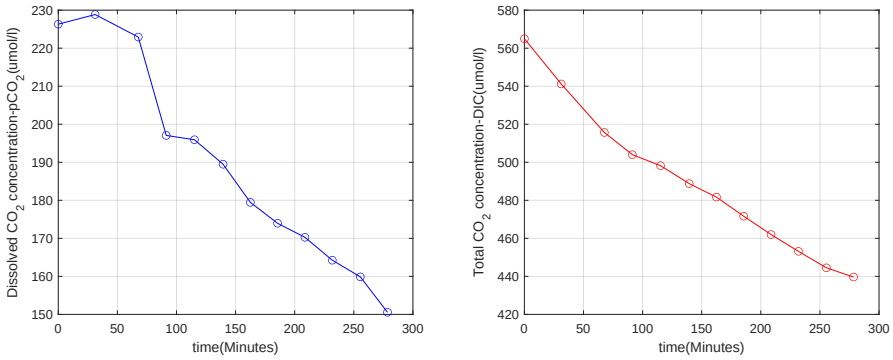

Figure 4.1: CO_2 partial pressure (left) and DIC (right) change in the water of small wave tank during the experiment

DIC in uniform unit of $\mu mol/L$. A decreasing trend in figure 4.1 is found for both DIC and partial pressure. With the wave breaking, DIC drops from 560 $\mu mol/L$ to 440 $\mu mol/L$ while CO_2 partial pressure of water decreases from 230 $\mu mol/L$ to 150 $\mu mol/L$. The gas transfer rate (k) can be evaluated as,

$$k = \frac{-h\partial DIC/\partial t}{S(pCO_{2w} - pCO_{2a})} \tag{4.1}$$

where h is water depth, S is the CO_2 solubility. pCO_{2w} and pCO_{2a} are CO_2 partial pressure in water and air, respectively. With the wave input frequency of 1.5 HZ and amplitude of 3 cm (first group of experiments), the CO_2 transfer velocity is estimated to be 5.29$\pm$0.77 cm/hr. After the wave input is changed to the second type with 1.9 HZ for frequency and 4 cm for amplitude, the gas transfer rate increases to 6.23$\pm$0.55 cm/hr. The standard error of the mean for the gas transfer rate of two groups are 14% and 8%, respectively, showing that the designed experimental instruments perform well in detecting the gas fluxes. The system error is reduced by setting up enough time for the equilibrium between air and water samples. Nonetheless, the temporal resolution is limited by enlarged sampling intervals (about 8 minutes). The CO_2 detection system can also be installed for field observations with sufficient time span.

	T_{02} (s)	Hs (cm)	steepness
wave(1.5 HZ), probe4	0.62	4.03	0.067
wave(1.9 HZ), probe4	0.44	5.26	0.174

Table 4.1: Waves parameters at probe 4 for two groups of experiments

The mean wave period (T_{02}), significant wave height (H_s) and wave steepness ($= H_s/L$, $L = 9.81/(2\pi \cdot T_{02}^2)$) are computed in table 4.1. The gas exchange rate should be correlated with the power of energy loss of breaking which is controlled by breaking rate (related with T_{02}) and mean energy loss of breakers (related with input H_s). In the experiments, the shallow water depth on the top of obstacle induces breaking of every incoming wave. The second group of experiments has higher CO_2 transfer rate than that of the first group because of the bigger input wave frequency and wave height.

The preliminary experiments in small wave tank demonstrate that the gas transfer rate change with different wave breaking conditions. The CO_2 detection system is also proved to be efficient in the application. To study the detailed dependence of gas transfer rate on wave breaking parameters (e.g. breaking probability, strength and breaking induced bubbles), more experiments need to be conducted. The scale of wave breaking in the flume with limited size is small, so the bubble effect in the experiment may not be evident. Moreover, the wave breaking is artificially forced by reducing the water depth. In the open ocean, the mechanism of waves evolving to breaking state is the superposition of wave components, which is a non-linear process (Babanin et al., 2010). The interaction between superimposed wind and waves at different fetch is also yet to be understood.

4.2 A new parameterization for CO_2 gas transfer velocity

In this section, the parameterization of CO_2 gas transfer is investigated based on the computed gas transfer rate and wave parameters from the experiments in big wind-wave flume of FIO laboratory. Compared with cases of monochromatic wave experiments (A5, A9, A10), significant wave height (H_s) and gas transfer rate (K_{600}) in B1-B6 become bigger due to the superimposed wind while breaking probability (b_T) tends to reduce with the coupled wind. Wind forcing can slow down the modulation of unstable waves and decrease the number of breakers (Babanin et al., 2010; Galchenko et al., 2012). Compared with cases B1-B6, C1-C6 clearly have smaller K_{600} due to the weak wave states although the wind speeds in B1-B6 and C1-C6 are in the same range.

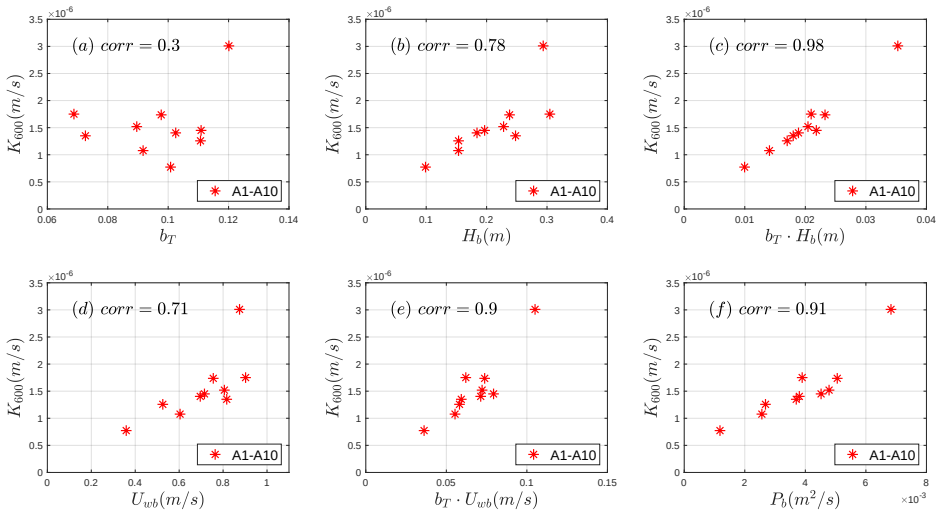

Figure 4.2: CO_2 gas transfer velocity of monochromatic wave experiments versus (a) wave breaking probability, (b) mean wave height of breakers, (c) product of breaking probability and mean wave height of breakers, (d) mean wave orbital velocity of breakers, (e) product of breaking probability and mean wave orbital velocity of breakers, (f) mean energy loss per unit of time of the breakers

In the monochromatic wave experiments (A1-A10), the dependence of K_{600} on b_T is weak (figure 4.2(a)), correlation between K_{600} and H_b is better (figure 4.2(b)), but the correlation coefficient between K_{600} and the product $b_T \cdot H_b$ in figure 4.2(c) is 98%. K_{600} is also found correlated with U_{wb} ($corr = 71\%$), and again the correlation coefficient is improved as 90% after multiplying b_T to U_{wb} in figure 4.2(e). The results can be explained as that b_T determines the frequency of occurrence of the water mixing events by breakers, while higher wave height and greater orbital

motion imply more turbulence in breaking events. In figure 4.2(f), K_{600} is also well correlated with the rate of energy loss (P_b) within experimental periods defined by

$$P_b = \frac{\sum (H_{b1}^2 - H_{b2}^2)}{\Delta t} \tag{4.2}$$

where H_{b1} and H_{b2} are the wave height before and after wave breaking, respectively. Δt is the time length of each experiment. P_b contains the information of wave breaking probability and average breaking strength. The energy loss due to breaking is passed to the turbulence whose production rate should be relevant to $b_T \cdot H_b$ and $b_T \cdot U_{wb}$. The results of experiments A1 to A10 demonstrate that wave breaking can enhance CO_2 gas flux without wind, and wave properties are directly relevant to the CO_2 gas transfer rate.

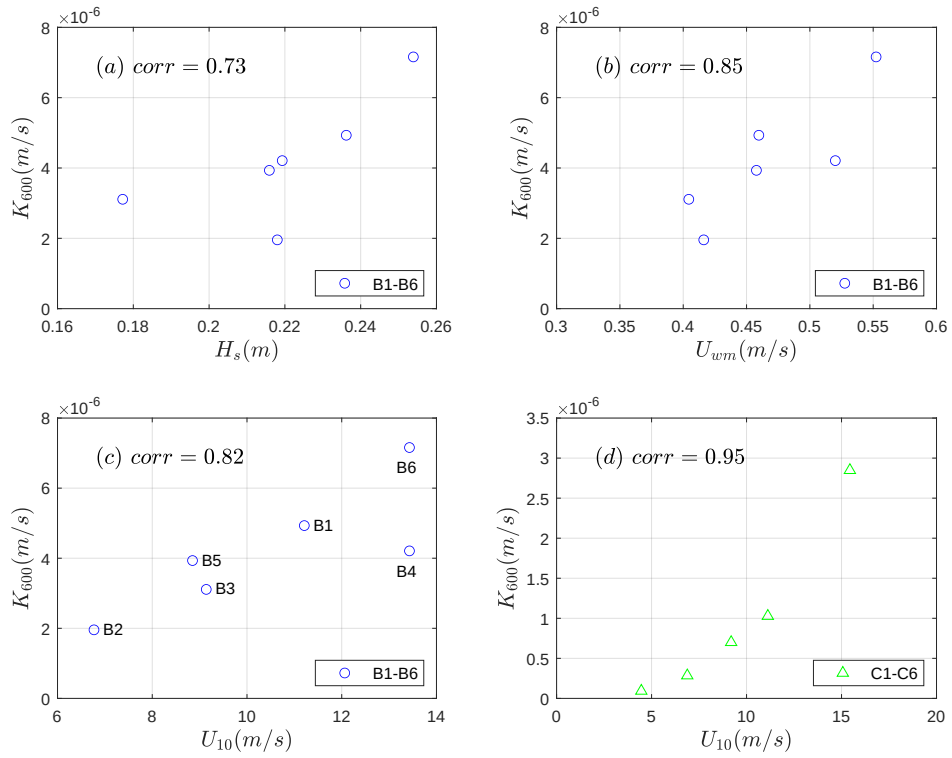

Figure 4.3: CO_2 transfer velocity in coupled wave experiments versus (a) significant wave height, (b) mean wave orbital velocity, (c) 10-meter wind speed. CO_2 gas transfer velocity in wind wave experiments versus (d) 10-meter wind speed

In the coupled wave experiments (B1-B6), CO_2 gas transfer velocity shows good correlation

with significant wave height (figure 4.3(a)), mean wave orbital velocity (figure 4.3(b)). The superimposed wind not only adjusts the wave breaking (e.g. breaking probability) but also ripples the smooth surface of non-breaking waves, which implies that the energy transfer from wind into waves. As a result, statistical parameters H_s and U_{wm} which are computed based on all waves, rather than breaking wave parameters (H_b or U_{wb}), are in good correlation with K_{600}. The 10-meter wind speed is also well correlated with the K_{600} (figure 4.3(c)). But experiments with similar U_{10} can lead to different K_{600} (e.g. B4 and B6 in panel(c)), which demonstrates the uncertainties of the wind-based parameterization.

In the wind wave experiments (C1-C6), K_{600} has a quadratic relation with wind speed (figure 4.3(d)). Similar high correlations are also found between K_{600} and wave parameters such as wave height and orbital velocity because waves at a fixed fetch grow with the increased wind forcing. From the figure 4.3(c) and (d), wind speed is a good parameter to describe gas exchange within each kind of experiment but can not collapse the two data sets.

From the correlation analysis, CO_2 exchange velocity is determined by water-side turbulence which is related with breaking probability, turbulence originated from each breaking event and turbulence of non-breaking waves affected by wind. The wind plays an indirect role by transferring energy into waves and direct but insignificant role by creating turbulence beyond water surface. An appropriate parameterization for CO_2 exchange velocity should be able to unify all data sets and physically reasonable. First, considering that the waves are of a different order at open ocean (i.e. to avoid the dependence on the dimensional wave parameters), K_{600} is scaled with the mean orbital velocity (U_{wm}) of waves through (4.3),

$$\tilde{K} = \frac{K_{600}}{U_{wm}} \tag{4.3}$$

where $\tilde{K}$ is a non-dimensional gas transfer velocity and directly related with waves. Meanwhile, K_{600} is found in a good correlation with wave height and orbital velocity in figure 4.2 and 4.3. Therefore, wave Reynolds number is used to denote the turbulence intensity in water. R_{HW} in equation (4.4) is the multiplication of breaking wave height and orbital velocity, and then divided by ν_w which is the viscosity of water. R_{HW} highlights the effect of breaking waves based on the analysis of experiments A1-A10 in figure 4.2. R_M in equation (4.5), on the other hand, consists of significant wave height, mean orbital velocity and ν_w. R_M is developed by considering the

statistical parameters based on all waves from the analysis of B1-B6 in figure 4.3.

$$R_{HW} = \frac{H_b \cdot U_{wb}}{\nu_w} \tag{4.4}$$

$$R_M = \frac{H_s \cdot U_{wm}}{\nu_w} \tag{4.5}$$

Wind speed is also scaled as in equation (4.6), following the method introduced in Lenain and Melville (2017).

$$\tilde{U} = \frac{U_*}{\sqrt{g \cdot H_s}} \tag{4.6}$$

where $\tilde{U}$ is the non-dimensional wind speed, U_* is the wind friction velocity, g is gravitational acceleration. It should be noted that $\sqrt{g \cdot H_s}$ is proportional to peak wave phase velocity C_p in fetch-limited conditions. Thus, $\tilde{U}$ has the meaning of the reciprocal of wave age.

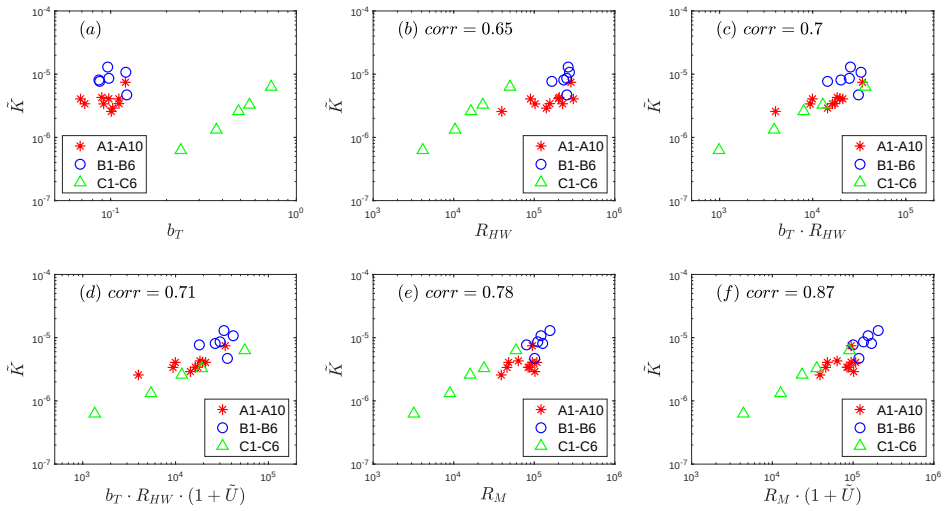

Figure 4.4: Non-dimensional CO_2 gas transfer velocity versus (a) wave breaking probability, (b) Reynolds number (R_{HW}), (c) product of breaking probability and Reynolds number (R_{HW}), (d) product of breaking probability, Reynolds number (R_{HW}) and scaled wind speed, (e) Reynolds number (R_M), (f) product of Reynolds number (R_M) and scaled wind speed

In figure 4.4(a), b_T alone obviously can not unify the results of all experiments. In figure 4.4(b), R_{HW} performs better but the disparity between data sets is still evident. In figure 4.4(c), the product of b_T and R_{HW} is used to signify the importance of both wave breaking

probability and wave breaking related turbulence, and the correlation is improved. As mentioned above, wind also transfers energy into non-breaking waves and creates turbulence at air-side. Considering the indirect role of wind forcing, the scaled wind speed is multiplied as an enhancement factor as $(1+\tilde{U})$ in figure 4.4(d). When the wind forcing approaches zero, the results converge to the no-wind (mechanically generated waves) conditions. The correlation is slightly improved and the parameterization is physically more reasonable. In figure 4.4(e) and (f), R_M alone performs well in unifying the data sets, but the correlation coefficient is further improved from 78% to 87% by multiplying R_M with $(1+\tilde{U})$. It should be mentioned that wind speed (or scaled wind speed) alone is unable to reconcile the results of B1-B6 and C1-C6.

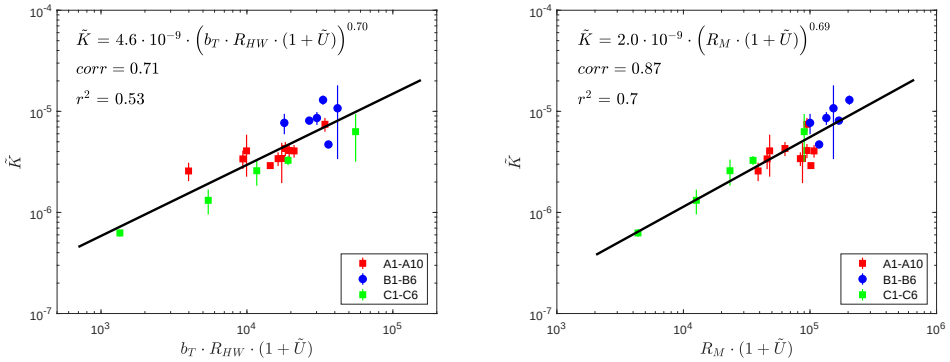

Figure 4.5: The left panel represents the gas transfer velocity parameterized with breaking probability, Reynolds number R_{HW} and wind speed. The right panel represents the gas transfer velocity parameterized with Reynolds number R_M and wind speed. The error bar represents the standard deviation of the mean for CO_2 transfer velocity

The whole expression for gas transfer from the left panel of figure 4.5 is written as in equation (4.7),

$$\tilde{K} = \alpha \cdot (b_T \cdot R_{HW} \cdot (1+\tilde{U}))^{\beta} \tag{4.7}$$

where the fitting parameters α and β are $4.6 \cdot 10^{-9}$ and 0.70, respectively. The correlation is 71% with resulted determination coefficient of 53%. The second expression from right panel in figure 4.5 is written in equation (4.8),

$$\tilde{K} = \alpha \cdot (R_M \cdot (1+\tilde{U}))^{\beta} \tag{4.8}$$

Where the fitting parameters α and β are $2.0 \cdot 10^{-9}$ and 0.69, respectively. The correlation is

computed to be 87% with resulted coefficient of determination to be 70%. Because similar types of wave Reynolds numbers are used as the dominant term in equation (4.7) and (4.8), the power parameter β in both equations are very close.

4.3 Discussion

Considering the fact that water-side dynamic processes have dominant impact on CO_2 gas exchange, we scale k_{600} with the mean wave orbital velocity rather than wind speed in equation (4.3). The orbital velocity is chosen also because water mass moves along with orbital motion. Equation (4.7) is established to highlight the effect of wave breaking for CO_2 gas exchange because the wave breaking is responsible for the production of bubbles and excessive amount of turbulence (Agrawal et al., 1992). b_T and R_{HW} denote the wave breaking rate and corresponding turbulence degree. Equation (4.8) uses another Reynolds number R_M to denote the overall wave-related turbulence. $\tilde{U}$ is proportional to the inverse of wave age, which represents the momentum transfer efficiency from wind to waves. The term $(1+\tilde{U})$ not only improves the correlation in our analysis, but also denotes the indirect impact of wind forcing to the gas exchange.

Similar forms of Reynolds numbers have been developed to denote wind-sea turbulence, such as $R_H = \frac{U_* H_s}{\nu_w}$ and $R_B = \frac{U_*^2}{\nu_w \omega_p}$ in Zhao and Xie (2010) and Brumer et al. (2017a), where ω_p is the peak frequency of ocean waves. The wind forcing in R_H and R_B shares equal or higher significance compared with wave parameters. As mentioned above, the waves and wave breaking rather than wind directly facilitate CO_2 gas exchange. In monochromatic wave experiments (A1-A10), the waves evolve to unsteady state and eventually break without wind ($U_* = 0$), which still promotes the gas transfer rate. Therefore, K_{CO_2} in the equation (4.7) and (4.8) is parameterized mainly on the features of waves. Nonetheless, our formulae need to be further validated by field data.

The breaking event is often accompanied with injection of bubbles which is not parameterized directly in our formula. Bubbles can enhance gas exchange because they increase the turbulence in water and extend air-water contact area. No consensus has been reached on bubble size distribution and behavior during wave breaking. The whitecap coverage which is empirically described by wind speed can be employed to denote bubble plume. Some studies prefer the physically based

method by correlating bubble injection rate (unit m/s) with energy dissipation rate (unit W/m^2) of breaking waves (Fairall et al., 2011; Long et al., 2011). The Reynolds number R_{HW} or R_M in this study is a measure of wave-induced turbulence, so they could possibly also be related to bubble injection rate although further evidence is needed. The wave energy loss of breakers is another parameter that can be correlated with bubbles. However, for the convenience of utilizing field data, wave energy loss is not considered in our formula.

Finally, we summarize the main findings in the laboratory work. The breaking probability with wave height or orbital velocity, energy loss of breakers and wind speed are found to be well correlated with the gas transfer velocity. To parameterize the dependence, formulae are built based on wave properties directly. Mean wave orbital velocity is used to scale CO_2 transfer rate. The breaking probability and wave Reynolds numbers are used as the dominant term to represent wave effect. The scaled wind speed is employed as an enhancement factor.

Chapter 5

Improved parameterization for CO_2 gas transfer based on field observation

5.1 Revised CO_2 gas transfer function with wave breaking

With different wind-wave sea states and sink/source area for gas exchange in the four campaigns, the dependence of CO_2 gas transfer rate on wind and waves can be better understood. The corrected data of wind, wave and CO_2 exchange parameters are used to compute non-dimensional variables for equation 4.3 to 4.8 in section 4.2. From former laboratory experiments, K_{660} is scaled by mean orbital velocity (U_{wm}) of waves and expressed as multiplication of Reynolds number (R_M) and wind enhancement factor in equation 4.8. The breaking probability is combined with Reynolds number (R_{HW}) in equation 4.7 to highlight the roles of breaking waves for the gas transfer rate. In the field observation, the breaking events can be properly identified but the wave height at breaking onset is difficult to be directly estimated from observation. Thus, the R_{HW} in equation 4.7 is replaced with R_M as,

$$\frac{K_{CO_2}}{U_{orb}} = \alpha \cdot \left[b_T \cdot \frac{H_s \cdot U_{orb}}{\nu_w} \cdot \left(1 + \frac{U_\star}{\sqrt{g \cdot H_s}} \right) \right]^{\beta} \cdot (Sc)^{-\frac{1}{2}} \tag{5.1}$$

R_M is found positively correlated with R_{HW} and can used as a proxy of wave breaking induced turbulence. Another motivation to compose equation 5.1 is that the application of breaking probability b_T restrains the gas transfer rate in the global gas flux estimation (see section 6.2).

To test the parameterization of gas transfer velocity from laboratory experiments, the hourly results from the campaign HIWINGS (Blomquist et al., 2017) are further averaged with equidensity bins of 15 points. In figure 5.1, the formula 4.8 is able to collapse the results from laboratory

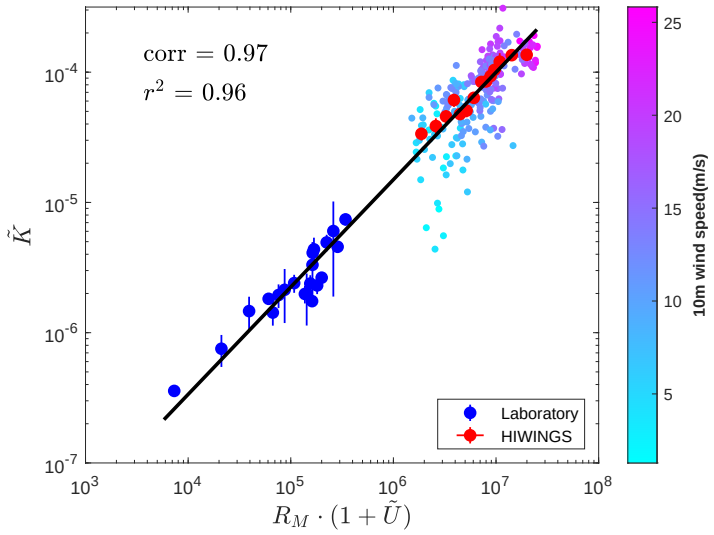

Figure 5.1: Comparison of the gas transfer velocity between laboratory experiments and campaign HIWINGS provided by Blomquist et al. (2017). The wave conditions are calculated by using formula 4.8. The hourly mean of HIWINGS (dots) results are averaged with equidensity bins of 15 points. The binned results (red disks) comply very well with our laboratory data (blue disks). The hourly 10-meter wind speeds ranging from 1-25 m/s for HIWINGS are also mapped on the dots.

experiment (blue disks) and HIWINGS (red disks) very well with high correlation (97%) and coefficient of determination (96%). The hourly mean results by using formula 4.8 for HIWINGS are represented with dots. The 10-meter wind speeds ranging from 1-25 m/s are also mapped on the dots. The wind speed complies with the increasing trend of gas transfer rate but the wind-based formula can not reconcile the measurements of both laboratory and HIWINGS. At low wind speed and mild sea state, there is some scatters for the binned results from hourly data.

On the other hand, formula 5.1 fails to unify the two data sets as in figure 5.2. The gas transfer velocity for HIWINGS is higher than that measured in laboratory experiments while the wave related terms for the two data sets are close. The initial motivation of using breaking probability in the formula is to specify the importance of wave breaking. The results, however, do not support formula 5.1 and we argue that the reason is the lack of bubble-mediated gas transfer in the parameterization. Accompanied with turbulence induced by wave breaking, the bubble injection for slightly soluble gas transfer is considered to be important at open ocean (Wanninkhof et al., 2009; Edson et al., 2011). The bubble size distribution for ocean wave breaking is different from that in

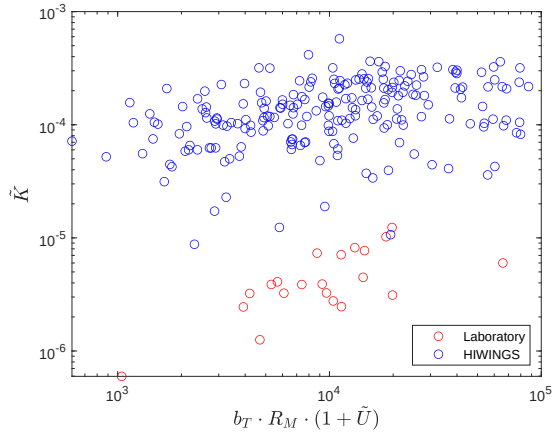

Figure 5.2: Comparison of the results from laboratory experiments (red circles) and HIWINGS (bule circles) by using formula 5.1. It is obvious that equation 5.1 can not reconcile the two data sets.

laboratory because of the magnitude of breakers and chemical property of water (Slauenwhite and Johnson, 1999; Anguelova and Huq, 2018). Thus, in formula 5.1, the bubble effect on gas transfer should also be scaled explicitly.

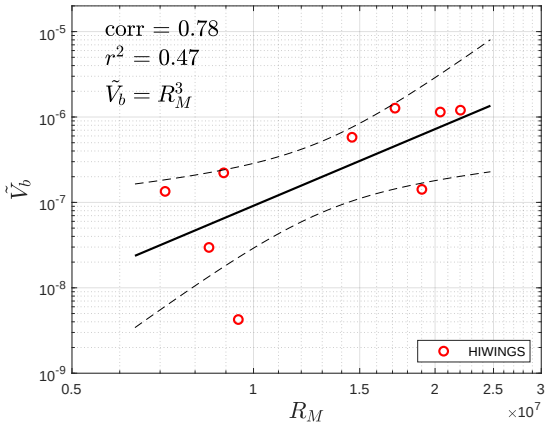

Figure 5.3: Non-dimensional bubble injection rate and Reynolds number R_M in logarithm scale from campaign HIWINGS. A cubic relationship is fitted with correlation of 78% and r-square of 47%. The dashed lines represent 90% confidence intervals.

There are multiple empirical parameterizations in previous studies (Woolf, 2005; Liang et al., 2013; Stanley et al., 2009) in which the injected bubble volume is usually correlated with wind speed. The physical models (Deike et al., 2016; Deane and Stokes, 2002) to describe the bubble size distribution are quite complex in the application for field observation data. From the studies of

Fairall et al. (2011) and Long et al. (2011), the bubble volume can be scaled with wave breaking dissipated energy. Considering that the wave Reynolds number denotes the physical meaning of wave breaking induced turbulence, the bubble volume can be further scaled with R_M. The bubble measurements during HIWINGS are used for the parameterization with R_M. The bubble injection rate (unit m/s) is first made non-dimensional by scaling with wave orbital velocity, following the same method in scaling gas transfer velocity. The non-dimensional bubble injection rate ($\tilde{V}_b$) is then found to be correlated with cubic R_M in figure 5.3, where the dashed curves are 90% confidence intervals. The correlation of $\tilde{V}_b$ and R_M is high (78%) but the coefficient of determination is 47% due to the paucity of data.

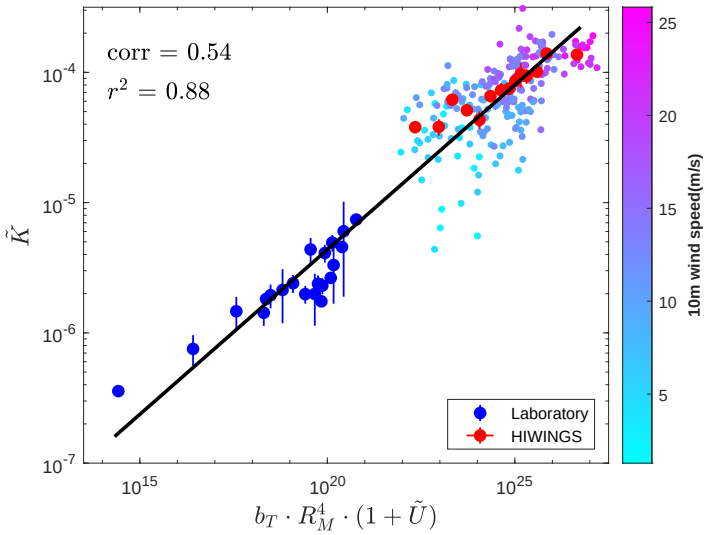

Figure 5.4: Comparison of the results from laboratory experiments and HIWINGS by using formula 5.2. The hourly mean of HIWINGS results (dots) are averaged with equidensity bins of 15 points. The binned results (red disks) comply very well with the laboratory data (blue disks) after incorporating the bubble-mediated gas transfer in the formula. The hourly 10-meter wind speeds ranging from 1-25 m/s for HIWINGS are also mapped on the dots.

The cubic relationship between bubble injection rate and Reynolds number is integrated into equation 5.1 which is rewritten as,

$$\frac{K_{CO_2}}{U_{orb}} = \alpha \cdot \left[b_T \cdot \left(\frac{H_s \cdot U_{orb}}{\nu_w} \right)^4 \cdot \left(1 + \frac{U_\star}{\sqrt{g \cdot H_s}} \right) \right]^\beta \cdot (Sc)^{-\frac{1}{2}} \tag{5.2}$$

where R_M has a total power of 4 in the equation. In figure 5.4, the improved equation 5.2 is able

to collapse the results from laboratory (blue disks) and binned HIWINGS data (red disks) with a high r-square of 88% but a relatively low correlation of 54%. The hourly wave results (dots) computed by formula 5.2 show some scatters at low wind speeds.

The processed CO_2 gas transfer velocity, wind and wave parameters for projects CAPRICOR, DYNAMO and SOGASEX are applied together with HIWINGS and laboratory results in figure 5.5. The field hourly results are all averaged into equidensity bins of 15 points. Panel (a) demonstrates the results by using formula 4.8 which is rewritten in equation 5.3,

$$\frac{K_{CO_2}}{U_{orb}} = \alpha \cdot \left[\frac{H_s \cdot U_{orb}}{\nu_w} \cdot \left(1 + \frac{U_\star}{\sqrt{g \cdot H_s}} \right) \right]^{\beta} \cdot (Sc)^{-\frac{1}{2}} \tag{5.3}$$

The obtained fitting parameter α and β is improved to be $9.57 \cdot 10^{-11}$ and 0.876. The correlation

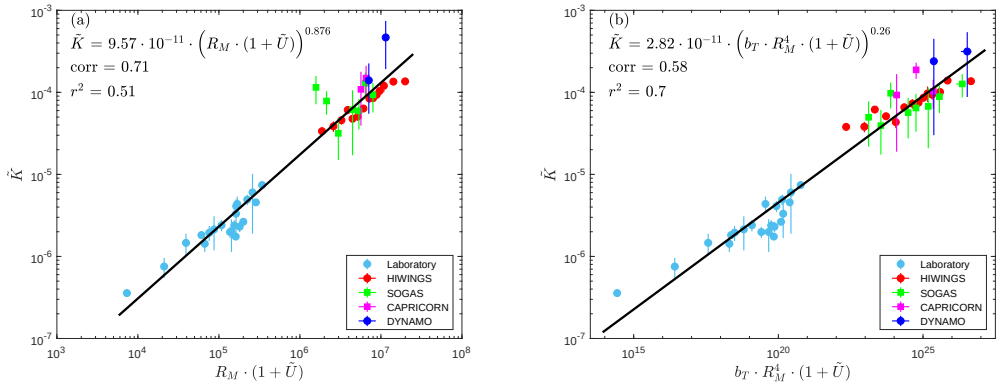

Figure 5.5: The results of laboratory experiments and four field observations. Panel (a) and (b) demonstrate the results using formula 5.3 and 5.2, respectively. The fitted parameterization, correlation coefficient and r-square are presented. The error bars denote the standard deviation of the mean for binned data.

computed from the overall data is 71% with r-square to be 51%. The error bars represent the standard deviation of the mean for the binned data. The data sets are reconciled well by using formula 5.3. The gas transfer from SOGASEX, CAPRICORN and DYNAMO have bigger uncertainties than that of HIWINGS because Licor-7500 CO_2 measurements are unitized for the former three campaigns while Picarro records are employed for HIWINGS. The open path analyzer (Licor-7500) suffers more interferences from environment than close path analyzer (Picarro) as discussed in section 3.4.2. In panel (b), equation 5.2 also collapses the four field data and laboratory results with correlation of 58% and r-square of 70%. The computed fitting coefficient α and β are

$2.82 \cdot 10^{-11}$ and 0.26, respectively. The equation 5.2 performs better than equation 5.3 in terms of reconciling the data sets with higher r-squre, which can be illustrated by the SOGAS results (green squares). The resulted correlation of equation 5.2, however, is less than that of equation 5.3.

5.2 Discussion

The equation 5.2 and 5.3 which are developed based on laboratory experiments considering the wave related mechanisms for air-sea CO_2 gas transfer are capable of collapsing the results from laboratory and field observations. The traditional wind-based formula, however, can not reconcile the lab experiments as discussed in section 4.3 and discrepancies exist in the fitting coefficients of the parameterizations for different field observations (Brumer et al., 2017a; Wanninkhof, 1992). Therefore, the efficiency of wind-only formula is limited by temporal and spacial scales of measurements and can only predict mean behavior of gas transfer based on the data sets. Equation 5.2 and 5.3 are validated by gas transfer measured at different locations of global ocean and may provide the opportunity to extend gas transfer estimates to conditions beyond measurements (e.g. tropical cyclones), although further evidence is needed. Equation 5.3 highlight the effect of all wave components including swells and wind waves while equation 5.2 estimates the gas transfer dominated by breaking waves through the parameter b_T. The swells in the ocean surface can generate turbulence (Babanin, 2006) which may promote the gas exchange (Brumer et al., 2017a). But equation 5.2 would predict zero gas transfer velocity for the conditions without wave breaking. Thus, equation 5.2 is applicable for wave breaking area so that b_T does not statistically approach zero.

The breaking events are often accompanied by whitecapping, making the bubble effect important for gas exchange at open ocean. No consensus has been reached on the bubble size distribution and behavior caused by breaking waves. The wave Reynolds Number R_M in our work which is used to denote wave breaking induced turbulence is also related to the bubble injection rate. However, the cubic dependence of bubble injection rate $\tilde{V}_b$ on R_M may not be precise because the bubble evolution involves with many parameters such as bubble diameter, penetration depth and whitecap coverage. Thus, more bubble measurements from open ocean are needed to validate the relationship in our study. Additionally, the bubble distribution parameterization should be devel-

oped with detailed physical mechanisms in the future such as the jet velocity (Deane and Stokes, 2002)) and breaking severity (Manasseh et al., 2006).

The hourly data in figure 5.1 and 5.4 scatter a bit at low Reynolds number and low wind speeds ($< 5m/s$). This may be caused by other factors such as surfactants at surface which have been found to substantially inhibit the gas transfer (Jähne et al., 1987; Frew, 1997). The dependence of gas transfer on Schmidt number also changes in equations (e.g. equation 5.2) with the existence of surfactants at sea surface. Buoyancy fluxes may also be responsible for the variability at low wind speed (Wanninkhof et al., 2009), which is still difficult to be parameterized without the knowledge of the impact of heat and momentum on gas exchange.

To summarize, the CO_2 gas transfer models developed from laboratory experiments are improved through observations of four field campaigns. The parameterizations (formula 5.2 and 5.3) successfully collapse the measured gas transfer velocity with different wind-sea states from open oceans and laboratory. Bubble effect is found to be correlated with Reynolds number (R_M) from HIWINGS measurements and is explicitly parameterized in equation 5.2. The wave field is one of the main factors dominating the CO_2 gas transfer although other mechanisms at low wind-wave state may be important too.

Chapter 6
Evaluation of CO_2 uptake by global ocean

6.1 Introduction

As reported in IPCC 5th assessment report (Pachauri et al., 2014), the global CO_2 emissions have been dramatically increased due to excessive anthropogenic activities. Thus, the evaluation of the impact of accumulated CO_2 on the global carbon cycle is essential. Since about 26% of atmospheric CO_2 inventory is absorbed by ocean, the ocean environment is severely affected such as the drop of pH by 0.1 for sea water. To date, there is huge uncertainties (up to 50%) in the products of estimations of air-sea CO_2 fluxes over global ocean. This uncertainty is mainly caused by the limited measurements of CO_2 partial pressure in the ocean and air, the parameterization for gas transfer velocity and the deviation of measured air-sea kinetic forcing parameters such as wind speed. In this chapter, the validated parameterizations for the gas transfer velocity are employed to compute the global ocean CO_2 fluxes (section 6.2). The trend of historical air-sea CO_2 fluxes is analyzed and compared with the results from previous researches. The advantages of using our formula are also presented. In section 6.3, the global ocean CO_2 fluxes are projected to the year 2100 for different scenarios (SSP126, SSP245 and SSP585) with CMIP6 data. The projections of the scenarios could provide insights for the evolution of air-sea CO_2 gas exchange in the global carbon system.

6.2 The hindcast of global ocean CO_2 uptake

6.2.1 The data sets of global parameters

The data sets in the present study are monthly averaged and interpolated to global mesh grid from year 1985 to 2017. The original data come from various sources with specified deviations. The atmospheric CO_2 concentration is obtained from GLOBALVIEW plus (GV+) observational CO_2 products from NOAA. Compared with former version of GLOBALVIEW (GV), GV+ comprises about 30 million measurements of actual data while the GV is the derived output based on observations. GV+ is characterized by its nominal hourly time step for all high-frequency measurements (where they are available). The original data with high or low time resolution from providers are reformatted into GV+ framework. The earlier products usually offer daily-mean values based on the subsets of hourly data to represent the large-scale distribution. However, the new data pack is adjusted to hourly product because the selection of criteria of large scale is no longer based on time but on wind speed or other tracers. The data quality flag is also provided for GV+ data, and we use the flag to remove CO_2 measurements that are locally influenced. More detailed information can be referred to Cooperative Global Atmospheric Data Integration Project (2019). A by-product of preparing former GV data is the Marine Boundary Layer (MBL) reference data (Dlugokencky et al., 2015), which is also employed in our study. The measurements of CO_2 data from NOAA are smoothed and extended to be representative of timely consecutive and latitudinal distributed atmospheric CO_2. The uncertainty of the data is also provided to help assess the product.

The GV+ and MBL reference data are used in our study to extract global distribution of atmospheric CO_2. Firstly, the scattered measurements at stations from GV+ data set are binned into monthly and latitudinal by longitudinal ($2.5^\circ \times 2.5^\circ$) boxes. For each spacial box, temporal interpolation is conducted by using the trends extracted from MBL reference data and the measurements in GV+. The linear trend of each month in different years is computed by using the MBL data because there is a seasonal variation of CO_2 concentration. For each month, the GV+ data is used to fill the temporal missing points with the help of computed trend. The same process is repeated for all geographic boxes that contain measurements from GV+. In the end, the gaps of CO_2 concentration at global surface for every month are filled by using spline interpolation. Because the atmospheric (especially latitudinal) mixing is fast, the results after the final spacial

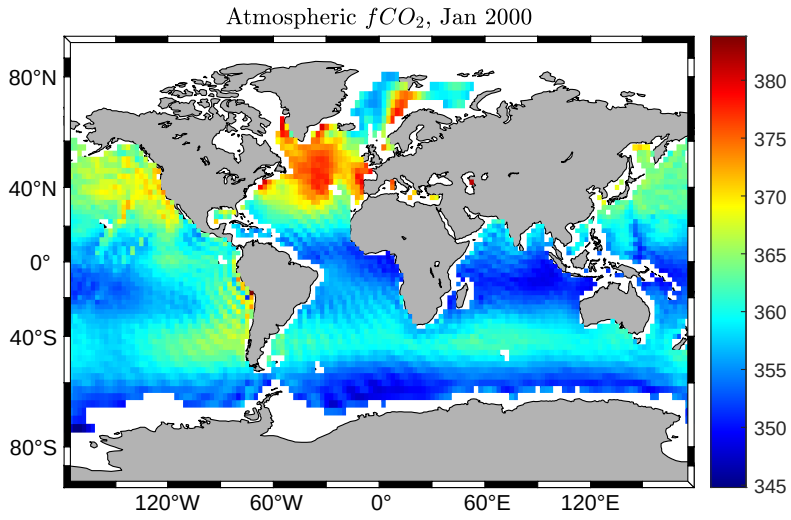

Figure 6.1: The global distribution of monthly mean air side CO_2 fugacity (ppm) in January 2000, excluding the area of Arctic Ocean

interpolation should be able to represent the real atmospheric CO_2 distribution. An alternative convenient way is to directly employ latitudinal MBL reference data to fill the missing bands, which also introduce the uncertainty from MBL data. We do not use the latter method in our study by considering the consistency of using GV+ data. An example of the air side CO_2 fugacity (fCO_{2a}) in January 2000 is shown in figure 6.1.

The water side CO_2 concentration is provided by Jones et al. (2019), in which the Surface ocean CO_2 Atlas (SOCAT) database is interpolated to global grid ($2.5° \times 2.5°$) from 1985 to 2017 based on a statistical gap-filling method. The results with computed uncertainty perform well in comparison with model data and can provide annual global coverage of water side CO_2 fugacity (fCO_{2w}). The SOCAT database is a synthesis of about 25 million points of measurements from ship campaigns where the ship is equipped with equilibrator systems to measure sea surface CO_2 concentration. An alternative to SOCAT data set is the LDEO database (Takahashi et al., 2019), which comprises 13.5 million measurements of surface CO_2 partial pressure over global oceans from year 1957-2018.

To compute the sea surface water viscosity and CO_2 solubility, the database of sea surface

temperature (SST), salinity (SSS) and mean sea level pressure (MSLP) are needed. The original SST data are obtained from satellite observations, which is detailed in Merchant et al. (2019). The specific data set (Good et al., 2019) used in our study is Level 4 Analysis Climate Data Record v2.0 which provides global daily coverage of SST with spacial resolution of 0.05 degree from year 1981 to 2016. The records is the combination of the observational data from the Advanced High Resolution Radiometer (AVHRR) and Along Track Scanning Radiometer (ATSR) SST records, using a data assimilation method to provide SSTs where there are no measurements. The SST data for year 2017 is supplemented with high-quality ERA-5 SST data. ERA-5 is the fifth generation of ECMWF reanalysis for the global weather and ocean. The database provides quantities of ocean-wave and atmospheric data from year 1979 to the present. The global daily MSLP data is also acquired from ERA-5 database with time length from 1985 to 2017. The daily SST and MSLP data are then averaged and interpolated to monthly global $2.5^\circ \times 2.5^\circ$ grid. The original SSS data is obtained from updated World Ocean Atlas 2018 (WOA2018) (Boyer et al., 2018; Zweng et al., 2019) in which the global climatological fields of sea surface water salinity data are provided. The new version of WOA2018 is featured for more oceanographic casts in the database and renewed quality control. The calculation of sea water viscosity follows the equation (22) in Sharqawy et al. (2010) and uses Thermodynamic Equation Of Seawater - 2010 (TEOS-10). The gas solubility of surface sea water is estimated by adopting the empirical equations in Wanninkhof (1992) and Weiss (1974). The Schmidt number of sea water is also computed to correct the calculated CO_2 exchange velocity to standard 20°C ($S_c = 660$).

The 10-meter wind speed, significant wave height and mean wave period data are obtained from ERA-5 database. The wave breaking probability (b_T) data is from the WaveWatchIII model (with ST6 module) output (Liu et al., 2019), in which b_T is calculated using parameterization from Babanin et al. (2001). The WaveWatchIII model is forced with ERA-5 wind speed data for the hindcast of wave fields. It should be mentioned that the resulted CO_2 fluxes barely change if the ERA-5 wave data is replaced with the wave data from WaveWatchIII model.

6.2.2 The historical trend of global ocean CO_2 uptake

The global ocean CO_2 fluxes are computed with the gridded data including the CO_2 partial pressure, wind and wave information. The parameterizations used to calculate gas exchange velocity

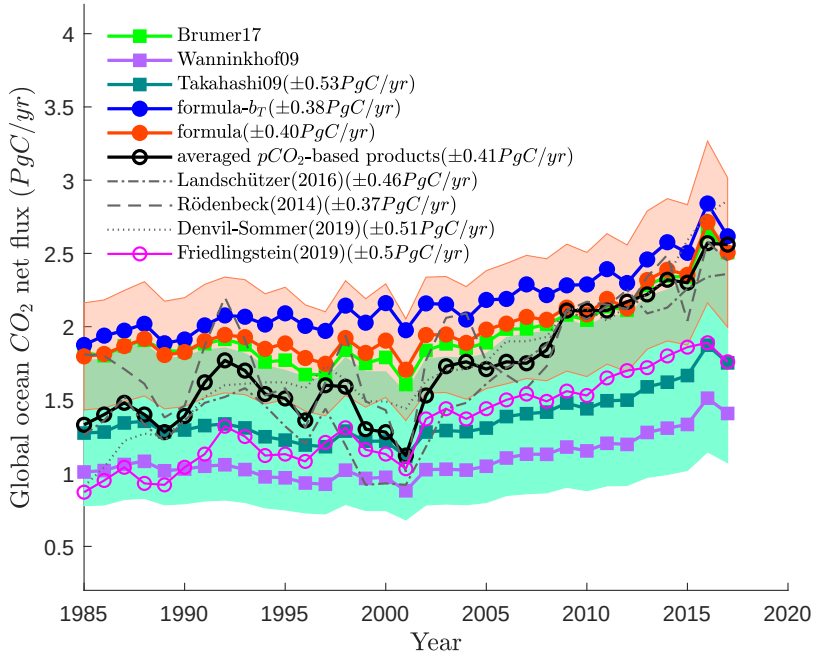

Figure 6.2: The annual global ocean CO_2 uptake. The formula from Brumer et al. (2017a), Wanninkhof et al. (2009), and Takahashi et al. (2009) together with our formula 5.2 and 5.3 are utilized to estimate the global ocean CO_2 uptake. The pCO_2 based products from Landschützer et al. (2016), Rödenbeck et al. (2014), Denvil-Sommer et al. (2019) and the average of the three products are presented. The results of Friedlingstein et al. (2019) are obtained from global models. The red and green shades denote for the uncertainty of results computed by formula 5.3 and formula 2.63 from Takahashi et al. (2009).

are equation 5.2 and 5.3 developed in chapter 5. The annual net ocean CO_2 fluxes (including the riverine flux contribution) at period 1985-2017 are shown in figure 6.2. The positive values of net fluxes represent sink fluxes from atmosphere to ocean. The red and blue solid line with disks are the estimated fluxes by using formula 5.3 and formula 5.2 (with breaking probability (b_T)), respectively. From the results, a general increasing trend is found for global ocean CO_2 uptake. The results of two formulae are in agreement with each other while the fluxes calculated by formula 5.2 is slightly higher than the results of formula 5.3 by about 0.17 PgC/yr. The solid line with green squares represents the fluxes calculated through equation 2.42 (B17) in Brumer et al. (2017a), which agrees very well with the results of our formula 5.3. The solid line with purple squares is computed by using wind-based formula 2.37 (W09) in Wanninkhof et al. (2009) in which the gas transfer velocity is expressed with wind speed of different moments. The solid line with cyan

squares is computed by formula 2.63 (T09) mentioned in Takahashi et al. (2009) in which the gas exchange is in quadratic relationship with wind speed. The W09 and T09 results are obviously lower than estimations of other formulae that use Reynolds numbers. All the estimated results share the similar increasing pattern for decadal trend. The black line with circles is the average of products from three independent researches (Landschützer et al., 2016; Rödenbeck et al., 2014; Denvil-Sommer et al., 2019) based on ocean pCO_2 measurements of SOCAT database (dashed gray lines). These products are also used to evaluate the efficiency of global models reproducing CO_2 fluxes in Friedlingstein et al. (2019). The averaged outputs of models are shown as pink line with circles in the figure after being adjusted with 0.78 PgC/yr for riverine transportation of CO_2. The model results underestimate the CO_2 fluxes of global ocean in comparison with pCO_2 based products (black line with circles). The results of our formulae and B17 overestimate the CO_2 fluxes before year 2003 compared with averaged pCO_2 based products while the decadal variation patterns are similar to each other and the pCO_2 based products are within the uncertainties of formula 5.3 (red shade). After year 2003, our formulae and B17 perform well with reported averaged pCO_2 based products. The T09 and W09 results, on the other hand, generally underestimate the CO_2 fluxes while the computed uncertainties of T09 (blue shade) cover the pCO_2 based results. The T09 estimations are in better agreement with averaged model outputs (pink line with circles).

The discrepancies between studies are evident since the uncertainties of estimations can be up to 50%. By comparing with other researches, our equations are able to give reasonable estimation of global ocean CO_2 flux. Takahashi et al. (2009) employed LDEO pCO_2 data and formula 2.63 to evaluate the global ocean CO_2 uptake at the reference year 2000. The computed net CO_2 uptake is $1.6 \pm 0.9 PgC/yr$ (without considering pre-industrial steady state air-sea CO_2 flux of $+0.4 PgC/yr$) which is close to our estimation of $1.9 \pm 0.40 PgC/yr$ by formula 5.3. Sweeney et al. (2007) employed the formula 2.28 which is close to the formula 2.63 in Takahashi et al. (2009) and give the net CO_2 flux in 1995 as $1.3 \pm 0.5 PgC/yr$. Our estimation by using formula 2.63 is $1.2 \pm 0.5 PgC/yr$ in 1995, which means that the data sets in the present study for the flux estimations are valid. Gruber et al. (2009) estimated a global CO_2 uptake rate at the nominal period between 1995 and 2000 to be $1.4 \pm 0.7 PgC/yr$ and our estimated rate is $1.7 \pm 0.36 PgC/yr$. Taking the riverine transported carbon to be $+0.4 PgC/yr$ as in Takahashi

et al. (2009), the estimations by formula 5.3 and 5.2 in period 2000-2010 are $2.3 \pm 0.36 PgC/yr$ and $2.4 \pm 0.37 PgC/yr$, respectively, which are in agreement with reported $2.3 \pm 0.6 PgC/yr$ in Pachauri et al. (2014) and $2.5 \pm 0.7 PgC/yr$ in Ishidoya et al. (2012). For the period 1990-2000, Keeling and Manning (2014) reported a ocean sink of $2.2 \pm 0.7 PgC/yr$ while our estimation by 5.3 is $2.2 \pm 0.36 PgC/yr$. Although the estimations by our equations are quite close to the results in previous studies, it should be mentioned that the riverine transported carbon can vary from $0.4 PgC/yr$ in Takahashi et al. (2009) to $0.45 - 0.78 PgC/yr$ in Resplandy et al. (2018).

In table 6.1, the annual trends of variables at source and sink area computed by different parameterizations are evaluated. The relative growth rates of all variables at period 1985-2017 are

	formula	formula-b_T	Brumer17	Takahashi09	Wanninkhof09
net flux(sink-source)	+36%	+37%	+35%	+35%	+38%
source flux	+5%	-2%	+8%	+2%	+1%
sink flux	+41%	+35%	+43%	+37%	+39%
$K_{CO_2} \cdot \alpha$	+7%	+9%	+5%	+4%	+4%
$K_{CO_2} \cdot \alpha$ source	+7%	+6%	+6%	+2%	+2%
$K_{CO_2} \cdot \alpha$ sink	+4%	+6%	+3%	+2%	+2%
K_{CO_2}	+8%	+10%	+6%	+5%	+5%
K_{CO_2} source	+11%	+10%	+10%	+7%	+6%
K_{CO_2} sink	+5%	+6%	+4%	+2%	+2%
absolute source area			-6%		
ΔpCO_2			+22%		
ΔpCO_2 source			+14%		
ΔpCO_2 sink			+9%		
α			-0.7%		
α source			-4%		
α sink			+0.5%		
SST			+3%		
SST source			+6%		
SST sink			+0.7%		
SSS			-0.09%		
SSS source			+0.1%		
SSS sink			-0.1%		

Table 6.1: Analysis of decadal trends of variables in the estimation of CO_2 flux of global ocean

linearly fitted and computed. For the net fluxes, the equations used in our study give a similar increasing rate of around 36%. The net fluxes are also divided into fluxes in source area and sink area. The sink fluxes calculated by all equations are rising in the past decades and the growth rate

is quite high compared with that of source fluxes. Only the source fluxes by formula 5.2 slightly decrease, which is mainly because of the shrink of source area about 6%. The gas flux can be expressed as the multiplication of gas transfer velocity (KCO_2), gas solubility (α), partial pressure difference (ΔpCO_2) and area for source or sink. In the period 1985-2017, the net global CO_2 uptake is increasing because the increment for both $KCO_2 \cdot \alpha$ and ΔpCO_2. The elevation of gas exchange velocity indicates that the global wind and waves strengthened during the past decades, which complies with the conclusions in Young et al. (2011). The emissions of anthropogenic CO_2 is responsible for excessive amount of atmospheric CO_2 and the increase of overall ΔpCO_2. Also, the accumulation of atmospheric CO_2 turns part of source area into sink area, which makes the ocean store more carbon. The ΔpCO_2 in source area is also increasing with time which is contradictory to the increased air side CO_2. The reason may be the rise of sea surface temperature in source area (6% compared with 0.7% in sink area) which decreases the CO_2 solubility and ocean capacity for storing CO_2. Takahashi et al. (1993) indicated that the isochemical temperature dependence of sea surface water pCO_2, $\partial lnpCO_2/\partial T$ is about 4.23%($^\circ C^{-1}$). The evident drop of CO_2 solubility (4% compared with slight increase of 0.5% in sink area) intensifies the outgassing of CO_2 in water. The solubility in sink area increases a bit, which is due to the combined influences from SST and SSS.

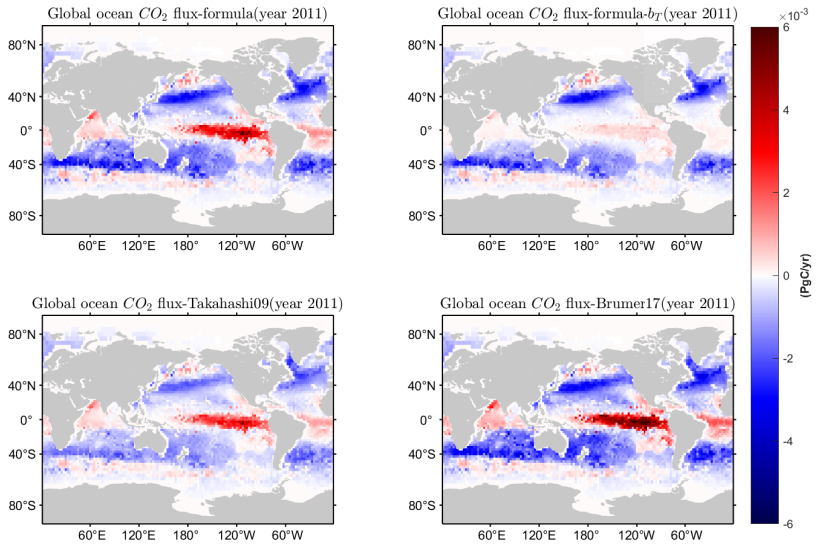

Figure 6.3: The global ocean CO_2 flux distribution in 2011 by different parameterizations.

Figure 6.3 shows the yearly mean global ocean CO_2 flux distribution in 2011 computed by different equations. The ocean source area (red) mainly lies at the tropical area where sea state is relatively mild. The sink area (blue) is mostly in high latitudes around 40° where high wind-wave state is usually recorded. By comparing the results of formula 5.3 (top left) and formula 5.2 (top right), it is obvious that the formula 5.2 gives lower flux estimations especially in source area (about half of source fluxes estimated by formula 5.3), which is also demonstrated in table 6.2. The main reason is that the parameter breaking probability (b_T) in formula 5.2 restrains the gas exchange velocity. Thus, the source and sink fluxes by formula 5.2 are lower than that by formula 5.3 although the net fluxes by the two equations are similar. More measurements are needed in the future to verify the two equations. By using Reynolds number composed with significant

$2011(PgC/yr)$	formula	formula-b_T	Brumer17	Takahashi09	Wanninkhof09
net flux(sink-source)	2.2	2.3	2.1	1.5	1.2
source flux	1.5	0.6	2.1	1.2	1.0
sink flux	3.7	2.9	4.2	2.7	2.2

Table 6.2: global ocean CO_2 fluxes in 2011 computed by different equations.

wave height and 10-meter wind speed in B17, the resulted source and sink fluxes (bottom right in figure 6.3) are higher than the results of our formulae which are composed with wave parameters. Although B17 gives the similar estimations with results of our formulae, the uncertainty of B17 should be higher by using wind parameter (see the analysis in section 6.2.3). The fluxes given by T09 (bottom left in figure 6.3) and W09 are lower in both source and sink area than the results of B17 and our parameterizations.

6.2.3 Uncertainty of the hindcast

The uncertainty of the estimations of global ocean CO_2 flux ranges from $0.37 - 0.53 PgC/yr$ as showed in figure 6.2. The IPCC fifth assessment report (Pachauri et al., 2014) mentions that the uncertainties of calculated global fluxes could be up to $\pm 50\%$ (Wanninkhof et al., 2013) which result from the limited coverage of ΔpCO_2 measurements, the biases of wind forcing and the uncertainties of gas transfer velocity parameterization. The uncertainties of global ocean uptake of CO_2 by using our formulae and T09 equation are listed in table 6.3. The total uncertainty

	flux(formula)	flux(formula-b_T)	flux(Takahashi09)
total uncertainty	20.34%	17.48%	38.86%
ΔpCO_2	14.49%	14.49%	14.49%
parameterization	14.27%	9.37%	30%
wind and wave variables	0.12%	2.78%	20%

Table 6.3: Estimated uncertainties of global ocean uptake of CO_2 by using different parameterizations

is contributed by the error from ΔpCO_2 data, the parameterization for transfer velocity and the wind/wave variables used in parameterization. The computation of uncertainty of ΔpCO_2 follows the procedure in Takahashi et al. (2009). The uncertainties of water side pCO_2 are provided by Jones et al. (2019) after reconstructing decadal global pCO_2 distribution. The annual mean uncertainty of water side pCO_2 is $\pm 13.22\ \mu atm$ for global $2.5^\circ \times 2.5^\circ$ boxes. The valid points of measurements from SOCAT are about 2.4×10^7 which are interpolated into 146905 boxes in 12 months. Hence, the average number of measurements in each box per month is about 13.8 although the actual number could vary significantly among the boxes. The average error of monthly mean seawater pCO_2 is about $\pm 3.56\ \mu atm\ (= 13.22/(13.8)^{1/2})$. The average error of air side pCO_2 is also evaluated as $\pm 0.38\ \mu atm$ through the same method. Therefore, the mean error of ΔpCO_2 is about $\pm 3.58\ \mu atm\ (= (3.56^2 + 0.38^2)^{1/2})$. For different equations, the mean gas transfer velocity and gas solubility are computed, which will be further multiplied by the error of ΔpCO_2 for the proportion of ΔpCO_2 caused uncertainties (14.49%) in the global net fluxes.

There is also uncertainties from the equations of gas transfer velocity. The parameterization based on wind speed is reported as 30% in Takahashi et al. (2009) while using Reynolds number in our study is as less as about 10%. Brumer et al. (2017a) also mentioned the lowered deviations of using Reynolds number compared with using wind-based formula. As assessed in Wanninkhof (1992), biases could be large for wind-based formulae from different researches and the discrepancies of predictions are evident at high wind speed range. The similar situation is also observed in our lab experiments in section 4.2 where the same wind speeds coupled with different wave states certainly result in various gas exchange velocity.

The parameters of wind and waves used in the equations also have uncertainties from measurements. The wind speed products usually are assumed to have an uncertainty of 10% as reported

in Takahashi et al. (2009). But with the improvement of ERA-5 data, the variation for wind measurements may be lowered. The uncertainty of wind after doing square in the equation is therefore 20%. In our formula, we mainly use the wave parameters instead of wind speed. In formula 5.3 the K_{CO_2} is proportional to $\frac{H_s^{2.75}}{T_{02}^{1.88}}$. With reported error for H_s to be 0.026% in ERA-5 database in Bidlot et al. (2019), we assume that T_{02} has the same error. The wind speed in the formula 5.3 is presented as an enhancement factor whose magnitude is about 1% of dominant term. So the combined wind and wave error is computed to be 0.12%. For formula 5.2, introducing the breaking probability (b_T) invokes uncertainty during calculating b_T. In Babanin et al. (2001), various data sets are used for the fitted curve in determining b_T and the estimated uncertainty of the equation is about 11.12%. Together with other variables, the error for variables in equation 5.2 is about 2.78%. The uncertainty for formula B17 is also evaluated to be 8.75% by using wind speed as one of the main constituents in the equation. Therefore, using wave dominated Reynolds number in parameterization can significantly reduce the uncertainties resulted from wind/wave measurements and the fitting coefficients of the equations.

6.3 The projected global ocean CO_2 uptake to year 2100

The future development of global ocean CO_2 uptake is also projected based on gas transfer parameterization and model output for future wind/wave and pCO_2. The climate models of the Coupled Model Intercomparison Projects (CMIP) are widely accepted, the prediction which is also used in the fifth IPCC reports. The sixth generation of CMIP models (CMIP6) are able to simulate global climate change in comprehensive future scenarios. In our study, we employ the future wind and wave data from First Institute of Oceanoghraphy (FIO) ESM v2.0 model results (Song et al., 2020) to project the impact of future global wind and wave on ocean CO_2 flux. FIO ESM v2.0 model integrates several distinct physical processes including the wave-induced vertical mixing, heat flux associated with sea spray and SST diurnal cycle scheme. The model could reproduce the different aspects of the climate system in global warming, surface temperatures, precipitation, and ocean circulation.

There are various socioeconomic assumptions to drive CMIP6 models which are named as Shared Socioeconomic Pathways (SSP). Five pathways are offered in the new SSPs to represent

broad trends of future society. The scenarios used in this study are scenario 126, 245 and 585 which represent a sustainable development (green road), middle road following historical trends and boosted development (highway) based on fossil fuel combustion, respectively. The detailed information for five pathway can be found in Riahi et al. (2017).

In figure 6.4, the future ocean CO_2 uptake is estimated by using formula 5.3 and CMIP6 forecast of wind and waves during the period 2017-2100. In addition, the global air-sea CO_2

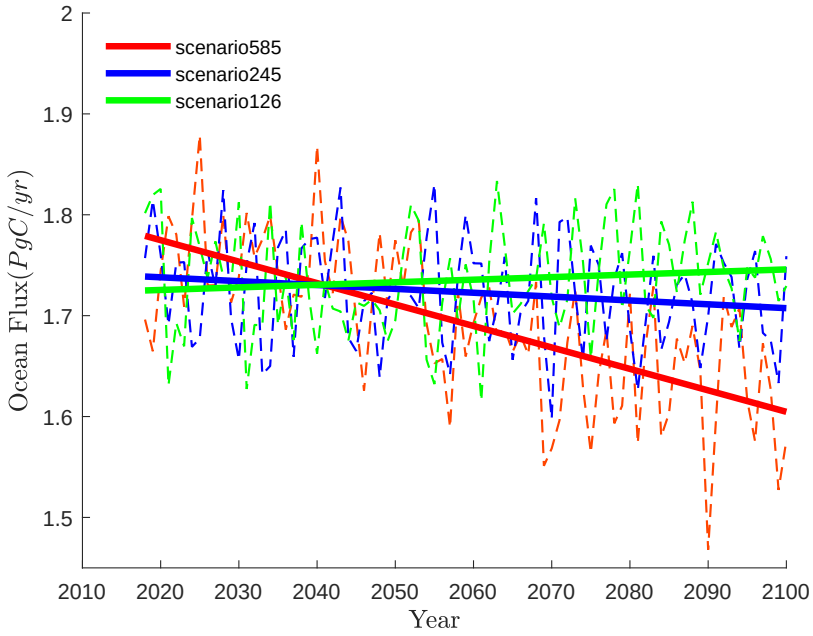

Figure 6.4: The global ocean CO_2 uptake with the predicted future wind and waves. Formula 5.3 is used to compute gas transfer velocity. The global air-sea CO_2 partial pressure, CO_2 solubility distribution is assumed the same as year 2017

partial pressure, CO_2 solubility distribution is assumed the same as year 2017. An obvious drop of CO_2 fluxes in scenario 585 (red line) is found while a slight decline is for scenario 245 (blue line). A slight rise for scenario 126 (green line) is captured. The change of future wind and wave situations should be responsible for the varied trend in different scenarios. As in table 6.4, for scenario SSP585, the significant wave height decreases while mean wave period increases. In formula 5.3, K_{CO_2} is proportional to $\frac{H_s^{2.75}}{T_{02}^{1.88}}$. Hence, an obvious drop of the K_{CO_2} and thus the net flux is found. For scenario SSP245, although H_s grows, the K_{CO_2} still declines a bit due to the increase of T_{02}. For scenario SSP126, the rise of H_s dominates the increasing trend of K_{CO_2}.

The total area change in the table 6.4 is the change of valid area with waves in the future, which mainly happens around the polar area due to the decreased coverage of ice. The area growth in SSP585 is the highest (2.07%) due to the assumption in CMIP6 model that much more fossil fuel is consumed.

	H_s	T_{02}	U_{10}	K_{CO_2}	Area total
SSP585	-1.08%	0.08%	-1.81%	-6.30%	2.07%
SSP245	0.09%	0.32%	-0.81%	-1.87%	1.21%
SSP126	0.47%	0.41%	-0.41%	0.35%	0.69%

Table 6.4: The trend of future wave and wind from CMIP6 model output, and the resulted trends for gas transfer rate.

In addition to future wind and waves, the future ΔpCO_2 data are also considered by using forecast data from NOAA CMIP6 model results (John et al., 2018). The resulted global ocean CO_2 fluxes are showed in the left panel of figure 6.5. The net fluxes for SSP585 tends to increase quite fast while the net fluxes would drop with time for the other two scenarios. The estimation is dominated by the different trend of assumed future CO_2 emissions in CMIP6 model for different SSPs (right panel in figure 6.5). It is obvious that the net flux trend is in high agreement with CO_2 emissions which directly affect the atmospheric CO_2 concentration, ΔpCO_2 and therefore the ocean net uptake of CO_2.

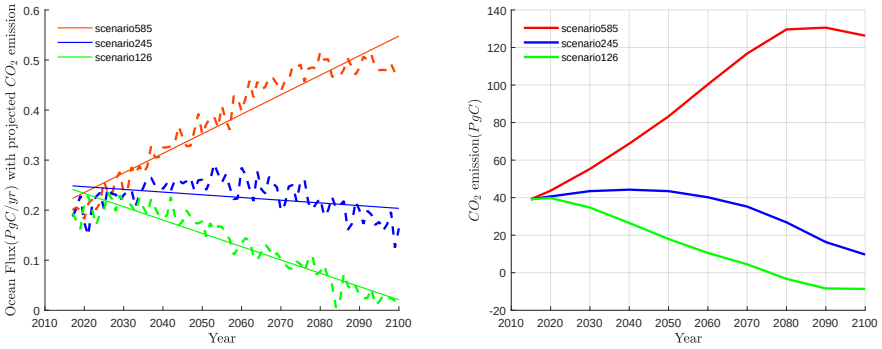

Figure 6.5: The global ocean CO_2 uptake with the change of future wind, waves and ΔpCO_2 (left panel). The assumed future CO_2 emissions in CMIP6 model for different SSPs (right panel).

6.4 Discussion and Conclusion

Through using comprehensive global data sets and our physical parameterizations of CO_2 transfer velocity, the historical global ocean CO_2 fluxes for the past 33 years is reproduced and the results comply with former pCO_2 based researches. Wind only parameterization used in our study for gas transfer velocity is generally underestimating the ocean CO_2 net flux and the uncertainty is higher than that by using formulae with Reynolds number. In figure 6.6, the same ΔpCO_2 and gas solubility distribution data are used from Landschützer et al. (2016) to estimate the CO_2 fluxes only with different parameterizations for gas transfer velocity. The formula 5.3 (red line with

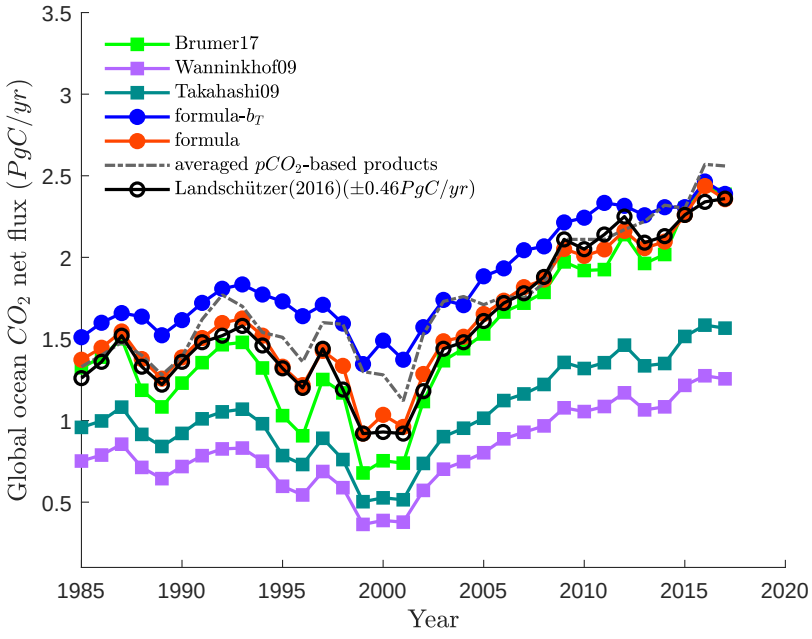

Figure 6.6: The historical global ocean CO_2 uptake with the same ΔpCO_2 distribution provided by Landschützer et al. (2016).

disks) has the best estimation compared with results from Landschützer et al. (2016) (black line with circles). The formula 5.2 (blue line with disks) produces relative high estimations but is close to averaged pCO_2 based products (dashed line) from former studies. Brumer et al. (2017a) scheme (green line with squares) also performs well but may deviate a bit around year 2000. The wind only parameterizations (Takahashi et al., 2009; Wanninkhof et al., 2009) again present smaller net fluxes although the trends comply well with other results. Therefore, the Reynolds number which

represents the wave and wave breaking induced turbulence at sea surface could predict the gas exchange velocity very well and is physically more reasonable.

The difference between formula 5.3 and 5.2 lies in the breaking probability in the parameterization. In figure 6.3, adding b_T in the equation makes the estimations smaller especially in equatorial place where wave breaking rate is low. The source fluxes in equatorial place are usually estimated with high uncertainties considering the fluxes are also affected by El Niño events(Quéré et al., 2003). Hence, further observations are needed to determine the advantage of formula 5.2.

In figure 6.2, the global ocean CO_2 fluxes are generally increasing with a higher growth rate after year 2002. The rising trends of ocean CO_2 uptake and the ocean CO_2 inventory have been supported by many other researches (Khatiwala et al., 2013; Landschützer et al., 2016; Rödenbeck et al., 2014; Wanninkhof et al., 2009). However, there are also studies of regional ocean CO_2 uptake suggesting that ocean CO_2 fluxes may have decreased (Le Quéré et al., 2007; Schuster and Watson, 2007). Although there is high possibility that the global ocean CO_2 inventory has been much increased due to excessive anthropogenic CO_2 emissions, the uncertainties of the predictions in section 6.2.3 which is mainly due to the limited quantity of pCO_2 measurements make it difficult to determine the change rate.

The predictions of future ocean CO_2 fluxes in section 6.3 provide the insight of how the wind and waves may affect the flux (figure 6.4) and the future CO_2 emissions will dominate the trend of ocean uptake (figure 6.5). However, the forecast results are computed with large uncertainties especially in figure 6.5 where the estimated ocean net fluxes have large discrepancies compared with historical tracks. The ΔpCO_2 distribution from CMIP6 model should be responsible for the difference and the ΔpCO_2 data with gas transfer parameterization might not be applicable for direct estimation of global ocean CO_2 fluxes.

To summarize, the developed CO_2 parameterizations based on features of waves and wave breaking are employed to compute the global ocean CO_2 uptake during period 1985-2017. The results comply well with estimations of previous studies. A uniform increasing trend of air-sea CO_2 flux for global ocean is observed. The gas transfer velocity schemes with Reynolds number show distinct advantages compared with traditional wind based parameterizations, such as the reduced uncertainties. The projections of ocean CO_2 fluxes are also computed by using wind and wave data from FIO ESM v2.0 and NOAA CMIP6 model. Different trends are found for the

corresponding scenarios and large uncertainties still remain in the predictions.

Chapter 7
Conclusions and Future Research

The global ocean CO_2 flux estimations are biased by the uncertainties from gas transfer velocity parameterizations. The present work provides a new formula for the gas transfer related directly with ocean waves. We extend the experimental methodology based on previous studies(Ocampo-Torres et al., 1994; Bandstra et al., 2006; Babanin et al., 2010). The CO_2 observation system is designed, prepared, installed at low cost and validated in laboratory. The experiments in the small/big wave flume are successfully conducted. Based on the analysis of experimental data, we for the first time scale the gas transfer rate directly with wave orbital velocity. The non-dimensional gas transfer velocity is further related with wind-sea Reynolds numbers (composed of wave parameters), wave breaking probability and an enhancement factor of wind speed. Compared with previous wind-based formulae, our formula highlights the direct and dominant role of waves and wave breaking instead of wind for the gas transfer. To stress the role of the waves, we note that the dependence of gas transfer on the monochromatic wave breaking forced by wave maker in the flume in absence of wind can not be described by traditional wind formulae in principle. Our parameterization can collapse the data sets well corresponding to various wind and wave conditions.

The laboratory-developed gas transfer formula is further tested with field campaign data. We follow the suggested procedures(Pierrot et al., 2009; Prytherch et al., 2010a; Edson et al., 2011) to correct the observed data, inducing CO_2 gas flux, partial pressure and wave records. With the estimated field gas transfer velocity, the formula 5.3 which comprises the wind-sea Reynolds number and wind-related enhancement factor is able to bring together the laboratory and field results very well. Formula 5.1 with wave breaking probability, however, failed and we argue that it is because the bubble-mediated gas transfer is more significant in ocean than in laboratory.

Therefore, we explicitly parameterized the bubble injection rate with Reynolds number instead of wind speed (Stanley et al., 2009; Liang et al., 2013). After integrating bubble's effect into equation 5.1, the improved formula (equation 5.2) performs well in reconciling the data sets.

The final parameterizations for CO_2 gas transfer velocity are employed for estimation of global ocean CO_2 uptake. Global data sets including ERA-5 wind and waves, wave breaking probability from WaveWatchIII model with ST6 physics, air-sea CO_2 partial pressure based on SOCAT database and ocean SST and salinity are utilized for reproduction of historical annual global ocean CO_2 uptake. Our computed decadal CO_2 flux trend complies well with previous studies(Friedlingstein et al., 2019). In addition, our formulae are found more efficient with reduced uncertainties compared with traditional wind-based parameterizations (Takahashi et al., 2009; Wanninkhof et al., 2009) in the flux estimation. The future CO_2 uptake by ocean is projected by exerting impact of future wind, waves and CO_2 emissions from CMIP6 model under three different scenarios.

In conclusion, the present work build a new parameterization to express CO_2 gas exchange as a function of properties of waves rather than wind directly, and is proved to perform well in the global ocean CO_2 flux estimation. With reduced uncertainties, the results may enhance our understanding of the global carbon cycle and be useful for future policy making.

As is discussed in chapter 5, the bubble-mediated gas transfer is quite important for poorly soluble gas. A physical parameterization of the bubble behavior should be investigated in details so that the gas transfer formula can be further improved. In addition, the accuracy of ocean CO_2 partial pressure distribution should be improved by collecting more observations and developing robust methods for the interpolation to global grid.

Nomenclature

BOM	Bureau of Meteorology
CRDS	Cavity Ring-Down Spectroscopy
CMIP	Coupled Model Intercomparison Project
CO_2	Carbon Dioxide
COARE	Coupled Ocean-Atmosphere Response Experiment
CSIRO	Commonwealth Scientific and Industrial Research Organisation
DIC	total Dissolved Inorganic Carbon
DMS	Dimethyl Sulfide
ECMWF	European Center for Medium-Range Weather Forecasts
ERA-5	ECMWF European ReAnalysis 5
ESM	Earth System Model
FIO	First Institute of Oceanography
GV	Global View database
GV+	Global View plus database
HIWINGS	High Wind Gas exchange Study
HCl	Hydrochloric acid
IPCC	Intergovernmental Panel on Climate Change

IRGA	Infrared gas analyzer
MBL	Marine Boundary Layer
MSLP	Mean Sea Level Pressure
$NaHCO_3$	Sodium bicarbonate
NCAR	National Center for Atmospheric Research
NCEP	National Centers for Environmental Prediction
NDIR	Nondispersive Infrared
NOAA	National Oceanic and Atmospheric Administration
RV	Research Vessel
SOCAT	Surface Ocean CO_2 Atlas
SOGASEX	Southern Ocean Gas Exchange project
SSS	Sea Surface Salinity
SST	Sea Surface Temperature
UTAS	University of Tasmania
WOA	World Ocean Atlas

Bibliography

YC Agrawal, EA Terray, MA Donelan, PA Hwang, AJ Williams, WM Drennan, KK Kahma, and SA Krtaigorodskii. Enhanced dissipation of kinetic energy beneath surface waves. *Nature*, 359 (6392):219–220, 1992.

MD Anguelova and P Huq. Effects of salinity on bubble cloud characteristics. *Journal of Marine Science and Engineering*, 6(1):1, 2018.

WE Asher, BJ Higgins, LM Karle, PJ Farley, CR Sherwood, WW Gardiner, R Wanninkhof, H Chen, T Lantry, and M Steckley. Measurement of gas transfer, whitecap coverage, and brightness temperature in a surf pool: An overview of wabex-93. *This volume*, 1995.

WE Asher, LM Karle, BJ Higgins, PJ Farley, EC Monahan, and IS Leifer. The influence of bubble plumes on air-seawater gas transfer velocities. *Journal of Geophysical Research: Oceans*, 101 (C5):12027–12041, 1996.

WE Asher, LM Karle, and BJ Higgins. On the differences between bubble-mediated air-water transfer in freshwater and seawater. *Journal of marine research*, 55(5):813–845, 1997.

AV Babanin. On a wave-induced turbulence and a wave-mixed upper ocean layer. *Geophysical Research Letters*, 33(20), 2006.

AV Babanin, IR Young, and ML Banner. Breaking probabilities for dominant surface waves on water of finite constant depth. *Journal of Geophysical Research: Oceans*, 106(C6):11659–11676, 2001.

AV Babanin, D Chalikov, IR Young, and I Savelyev. Predicting the breaking onset of surface water waves. *Geophysical research letters*, 34(7), 2007.

AV Babanin, D Chalikov, IR Young, and I Savelyev. Numerical and laboratory investigation of breaking of steep two-dimensional waves in deep water. *Journal of Fluid Mechanics*, 644: 433–463, 2010.

AV Babanin, T Waseda, T Kinoshita, and A Toffoli. Wave breaking in directional fields. *Journal of Physical Oceanography*, 41(1):145–156, 2011.

L Bandstra, B Hales, and T Takahashi. High-frequency measurements of total co 2: Method development and first oceanographic observations. *Marine Chemistry*, 100(1):24–38, 2006.

ML Banner, AV Babanin, and IR Young. Breaking probability for dominant waves on the sea surface. *Journal of Physical Oceanography*, 30(12):3145–3160, 2000.

TG Bell, S Landwehr, SD Miller, WJ Bruyn, AH Callaghan, B Scanlon, B Ward, MX Yang, and ES Saltzman. Estimation of bubble-mediated air–sea gas exchange from concurrent dms and co 2 transfer velocities at intermediate–high wind speeds. *Atmospheric Chemistry and Physics*, 17 (14):9019–9033, 2017.

ML Bender, DT Ho, MB Hendricks, R Mika, MO Battle, PP Tans, TJ Conway, B Sturtevant, and N Cassar. Atmospheric o2/n2 changes, 1993–2002: Implications for the partitioning of fossil fuel co2 sequestration. *Global Biogeochemical Cycles*, 19(4), 2005.

TB Benjamin and JE Feir. The disintegration of wave trains on deep water part 1. theory. *Journal of Fluid Mechanics*, 27(3):417–430, 1967.

JR Bidlot, G Lemos, and A Semedo. Era5 reanalysis and era5-based ocean wave hindcast. 2019. URL `http://www.waveworkshop.org/16thWaves/Presentations/R1%20Wave_Workshop_2019_Bidlot_et_al.pdf`.

B Blomquist, BJ Huebert, CW Fairall, L Bariteau, JB Edson, JE Hare, and WR McGillis. Advances in air-sea co2 flux measurement by eddy correlation. *Boundary-Layer Meteorology*, 152, 03 2014. doi: 10.1007/s10546-014-9926-2.

BW Blomquist, SE Brumer, CW Fairall, BJ Huebert, CJ Zappa, IM Brooks, M Yang, L Bariteau, J Prytherch, JE Hare, et al. Wind speed and sea state dependencies of air-sea gas transfer: Re-

sults from the high wind speed gas exchange study (hiwings). *Journal of Geophysical Research: Oceans*, 122(10):8034–8062, 2017.

EJ Bock, T Hara, NM Frew, and WR McGillis. Relationship between air-sea gas transfer and short wind waves. *Journal of Geophysical Research: Oceans*, 104(C11):25821–25831, 1999.

TP Boyer, HE Garcia, RA Locarnini, MM Zweng, AV Mishonov, JR Reagan, KA Weathers, OK Baranova, D Seidov, and IV Smolyar. World ocean atlas 2018. 2018.

SE Brumer, CJ Zappa, BW Blomquist, CW Fairall, A Cifuentes-Lorenzen, JB Edson, IM Brooks, and BJ Huebert. Wave-related reynolds number parameterizations of co2 and dms transfer velocities. *Geophysical Research Letters*, 44(19):9865–9875, 2017a.

SE Brumer, CJ Zappa, IM Brooks, H Tamura, SM Brown, BW Blomquist, CW Fairall, and A Cifuentes-Lorenzen. Whitecap coverage dependence on wind and wave statistics as observed during so gasex and hiwings. *Journal of Physical Oceanography*, 47(9):2211–2235, 2017b.

JG Canadell, C Le Quéré, MR Raupach, CB Field, ET Buitenhuis, P Ciais, TJ Conway, NP Gillett, RA Houghton, and G Marland. Contributions to accelerating atmospheric co2 growth from economic activity, carbon intensity, and efficiency of natural sinks. *Proceedings of the national academy of sciences*, 104(47):18866–18870, 2007.

D Chalikov and S Rainchik. Coupled numerical modelling of wind and waves and the theory of the wave boundary layer. *Boundary-layer meteorology*, 138(1):1–41, 2011.

D Chalikov and D Sheinin. *Numerical modeling of surface waves based on principal equations of potential wave dynamics*. US Department of Commerce, National Oceanic and Atmospheric Administration, National Weather Service, National Centers for Environmental Protection, 1996.

D Chalikov and D Sheinin. Modeling extreme waves based on equations of potential flow with a free surface. *Journal of Computational Physics*, 210(1):247–273, 2005.

H Chen, J Winderlich, C Gerbig, A Hoefer, CW Rella, ER Crosson, AD Van Pelt, J Steinbach, O Kolle, V Beck, et al. High-accuracy continuous airborne measurements of greenhouse gases (co2 and ch4) using the cavity ring-down spectroscopy (crds) technique. 2010.

Cooperative Global Atmospheric Data Integration Project. Multi-laboratory compilation of atmospheric carbon dioxide data for the period 1957-2018; obspack-co2-1-globalviewplus-v5.0-2019-08-12, 2019. URL `http://www.esrl.noaa.gov/gmd/ccgg/obspack/data.php?id=obspack-co2-1-GLOBALVIEWplus-v5.0-2019-08-12`.

PV Danckwerts. Significance of liquid-film coefficients in gas absorption. *Industrial & Engineering Chemistry*, 43(6):1460–1467, 1951.

SP De Szoeke, JB Edson, JR Marion, CW Fairall, and L Bariteau. The mjo and air–sea interaction in toga coare and dynamo. *Journal of Climate*, 28(2):597–622, 2015.

EL Deacon. Gas transfer to and across an air-water interface. *Tellus*, 29(4):363–374, 1977.

GB Deane and MD Stokes. Scale dependence of bubble creation mechanisms in breaking waves. *Nature*, 418(6900):839, 2002.

L Deike, WK Melville, and S Popinet. Air entrainment and bubble statistics in breaking waves. *Journal of Fluid Mechanics*, 801:91–129, 2016.

A Denvil-Sommer, M Gehlen, M Vrac, and C Mejia. Lsce-ffnn-v1: the reconstruction of surface ocean pco2. 2019.

EJ Dlugokencky, KA Masarie, PM Lang, and PP Tans. Noaa greenhouse gas reference from atmospheric carbon dioxide dry air mole fractions from the noaa esrl carbon cycle cooperative global air sampling network. *Data Path: ftp://aftp. cmdl. noaa. gov/data/tracegases/co2/flask/surface/(last access: 1 September 2017)*, 2015.

MA Donelan, J Hamilton, and WH Hui. Directional spectra of wind-generated ocean waves. *Philosophical Transactions of the Royal Society of London. Series A, Mathematical and Physical Sciences*, 315(1534):509–562, 1985.

SC Doney, B Tilbrook, S Roy, N Metzl, C Le Quéré, M Hood, RA Feely, and D Bakker. Surface-ocean co2 variability and vulnerability. *Deep Sea Research Part II: Topical Studies in Oceanography*, 56(8-10):504–511, 2009.

JB Edson, CW Fairall, L Bariteau, Christopher J Zappa, A Cifuentes-Lorenzen, Wade R McGillis, S Pezoa, JE Hare, and D Helmig. Direct covariance measurement of co2 gas transfer velocity

during the 2008 southern ocean gas exchange experiment: Wind speed dependency. *Journal of Geophysical Research: Oceans*, 116(C4), 2011.

CW Fairall, JE Hare, JB Edson, and W McGillis. Parameterization and micrometeorological measurement of air–sea gas transfer. *Boundary-Layer Meteorology*, 96(1-2):63–106, 2000.

CW Fairall, EF Bradley, JE Hare, AA Grachev, and JB Edson. Bulk parameterization of air–sea fluxes: Updates and verification for the coare algorithm. *Journal of climate*, 16(4):571–591, 2003.

CW Fairall, MX Yang, L Bariteau, JB Edson, D Helmig, W McGillis, S Pezoa, JE Hare, B Huebert, and B Blomquist. Implementation of the coupled ocean-atmosphere response experiment flux algorithm with co2, dimethyl sulfide, and o3. *Journal of Geophysical Research: Oceans*, 116(C4), 2011.

GE Fortescue and JRA Pearson. On gas absorption into a turbulent liquid. *Chemical Engineering Science*, 22(9):1163–1176, 1967.

NM Frew. The role of organic films in air-sea gas exchange. *The sea surface and global change*, pages 121–172, 1997.

NM Frew, EJ Bock, U Schimpf, T Hara, H Haußecker, JB Edson, WR McGillis, RK Nelson, SP McKenna, BM Uz, et al. Air-sea gas transfer: Its dependence on wind stress, small-scale roughness, and surface films. *Journal of Geophysical Research: Oceans*, 109(C8), 2004.

P Friedlingstein, M Jones, M O'sullivan, R Andrew, J Hauck, G Peters, W Peters, J Pongratz, S Sitch, C Le Quéré, et al. Global carbon budget 2019. *Earth System Science Data*, 11(4): 1783–1838, 2019.

A Galchenko, AV Babanin, D Chalikov, IR Young, and TW Hsu. Modulational instabilities and breaking strength for deep-water wave groups. *Journal of Physical Oceanography*, 40(10): 2313–2324, 2010.

A Galchenko, V Babanin, D Chalikov, IR Young, and BK Haus. Influence of wind forcing on modulation and breaking of one-dimensional deep-water wave groups. *Journal of Physical Oceanography*, 42(6):928–939, 2012.

S.A. Good, O. Embury, C.E. Bulgin, and J. Mittaz. Esa sea surface temperature climate change initiative (sst-cci): Level 4 analysis climate data record, version 2.0. centre for environmental data analysis, 22 august 2019. doi:10.5285/aced40d7cb964f23a0fd3e85772f2d48., 2019. URL http://dx.doi.org/10.5285/aced40d7cb964f23a0fd3e85772f2d48.

N Gruber, M Gloor, SE Mikaloff Fletcher, SC Doney, S Dutkiewicz, MJ Follows, M Gerber, AR Jacobson, F Joos, K Lindsay, et al. Oceanic sources, sinks, and transport of atmospheric co2. *Global biogeochemical cycles*, 23(1), 2009.

B Hales, D Chipman, and T Takahashi. High-frequency measurement of partial pressure and total concentration of carbon dioxide in seawater using microporous hydrophobic membrane contactors. *Limnology and Oceanography: Methods*, 2(11):356–364, 2004.

W Henry. Iii. experiments on the quantity of gases absorbed by water, at different temperatures, and under different pressures. *Philosophical Transactions of the Royal Society of London*, 93: 29–274, 1803.

R Higbie. The rate of absorption of a pure gas into a still liquid during short periods of exposure. *Trans. AIChE*, 31:365–389, 1935.

DT Ho, CJ Zappa, WR McGillis, LF Bliven, B Ward, JWH Dacey, P Schlosser, and MB Hendricks. Influence of rain on air-sea gas exchange: Lessons from a model ocean. *Journal of Geophysical Research: Oceans*, 109(C8), 2004.

DT Ho, CS Law, MJ Smith, P Schlosser, M Harvey, and P Hill. Measurements of air-sea gas exchange at high wind speeds in the southern ocean: Implications for global parameterizations. *Geophysical Research Letters*, 33(16), 2006.

S Ishidoya, S Aoki, D Goto, T Nakazawa, S Taguchi, and P Patra. Time and space variations of the o2/n2 ratio in the troposphere over japan and estimation of the global co2 budget for the period 2000–2010. *Tellus B: Chemical and Physical Meteorology*, 64(1):18964, 2012.

K Iwano, N Takagaki, R Kurose, and S Komori. Mass transfer velocity across the breaking air–water interface at extremely high wind speeds. *Tellus B: Chemical and Physical Meteorology*, 65(1):21341, 2013.

CMJ Jacobs, WIM Kohsiek, and WA Oost. Air–sea fluxes and transfer velocity of co2 over the north sea: results from asgamage. *Tellus B*, 51(3):629–641, 1999.

AR Jacobson, SE Mikaloff Fletcher, N Gruber, JL Sarmiento, and M Gloor. A joint atmosphere-ocean inversion for surface fluxes of carbon dioxide: 1. methods and global-scale fluxes. *Global Biogeochemical Cycles*, 21(1), 2007.

B Jahne, KO Münnich, and U Siegenthaler. Measurements of gas exchange and momentum transfer in a circular wind-water tunnel. *Tellus*, 31(4):321–329, 1979.

B Jähne, KO Münnich, R Bösinger, A Dutzi, W Huber, and P Libner. On the parameters influencing air-water gas exchange. *Journal of Geophysical Research: Oceans*, 92(C2):1937–1949, 1987.

B Jähne, P Libner, R Fischer, T Billen, and EJ Plate. Investigating the transfer processes across the free aqueous viscous boundary layer by the controlled flux method. *Tellus B: Chemical and Physical Meteorology*, 41(2):177–195, 1989.

JG John, C Blanton, C McHugh, A Radhakrishnan, K Rand, H Vahlenkamp, C Wilson, NT Zadeh, P Gauthier, JP Dunne, R Dussin, LW Horowitz, P Lin, S Malyshev, V Naik, J Ploshay, L Silvers, C Stock, M Winton, and YJ Zeng. Noaa-gfdl gfdl-esm4 model output prepared for cmip6 scenariomip ssp126, 2018. URL `https://doi.org/10.22033/ESGF/CMIP6.8684`.

SD Jones, C Le Quéré, C Rödenbeck, AC Manning, and A Olsen. Update to the Data and Code archive for the interpolation of surface ocean carbon dioxide, 2019. URL `https://doi.org/10.1594/PANGAEA.898196`.

RF Keeling. On the role of large bubbles in air-sea gas exchange and supersaturation in the ocean. *Journal of Marine Research*, 51(2):237–271, 1993.

RF Keeling and AC Manning. Studies of recent changes in atmospheric o2 content. Elsevier, 2014.

SP Khatiwala, T Tanhua, SE Mikaloff Fletcher, M Gerber, SC Doney, HD Graven, N Gruber, GA McKinley, A Murata, AF Ríos, et al. Global ocean storage of anthropogenic carbon. *Biogeosciences*, 10(4):2169–2191, 2013.

KE Krall and B Jähne. First laboratory study of air-sea gas exchange at hurricane wind speeds. *Ocean Science*, 10(2):257, 2014.

KE Krall, AW Smith, N Takagaki, and B Jähne. Air–sea gas exchange at wind speeds up to 85 m s-1. *Ocean Science*, 15(6), 2019.

VP Krasitskii. On reduced equations in the hamiltonian theory of weakly nonlinear surface waves. *Journal of Fluid Mechanics*, 272:1–20, 1994.

JC Lamont and DS Scott. An eddy cell model of mass transfer into the surface of a turbulent liquid. *AIChE Journal*, 16(4):513–519, 1970.

P Landschützer, N Gruber, DCE Bakker, and U Schuster. Recent variability of the global ocean carbon sink. *Global Biogeochemical Cycles*, 28(9):927–949, 2014.

P Landschützer, N Gruber, and DCE Bakker. Decadal variations and trends of the global ocean carbon sink. *Global Biogeochemical Cycles*, 30(10):1396–1417, 2016.

C Le Quéré, C Rödenbeck, ET Buitenhuis, TJ Conway, R Langenfelds, A Gomez, C Labuschagne, M Ramonet, T Nakazawa, N Metzl, et al. Saturation of the southern ocean co2 sink due to recent climate change. science, 316 (5832): 1735–1738. *Cited on*, page 7, 2007.

L Lenain and WK Melville. Measurements of the directional spectrum across the equilibrium saturation ranges of wind-generated surface waves. *Journal of Physical Oceanography*, 47(8): 2123–2138, 2017.

JH Liang, C Deutsch, JC McWilliams, B Baschek, PP Sullivan, and D Chiba. Parameterizing bubble-mediated air-sea gas exchange and its effect on ocean ventilation. *Global Biogeochemical Cycles*, 27(3):894–905, 2013.

JS Lim, M Park, Jinbok Lee, and Jeongsoon Lee. Validation of spectroscopic gas analyzer accuracy using gravimetric standard gas mixtures: impact of background gas composition on co 2 quantitation by cavity ring-down spectroscopy. *Atmospheric Measurement Techniques*, 10(12): 4613, 2017.

PS Liss. Processes of gas exchange across an air-water interface. In *Deep Sea Research and Oceanographic Abstracts*, volume 20, pages 221–238. Elsevier, 1973.

PS Liss and L Merlivat. Air-sea gas exchange rates: Introduction and synthesis. In *The role of air-sea exchange in geochemical cycling*, pages 113–127. Springer, 1986.

QX Liu, WE Rogers, AV Babanin, IR Young, L Romero, S Zieger, FL Qiao, and CL Guan. Observation-based source terms in the third-generation wave model wavewatch iii: Updates and verification. *Journal of Physical Oceanography*, 49(2):489–517, 2019.

MS Long, WC Keene, DJ Kieber, DJ Erickson, and H Maring. A sea-state based source function for size-and composition-resolved marine aerosol production. *Atmospheric Chemistry and Physics*, 11(3):1203–1216, 2011.

R Manasseh, AV Babanin, C Forbes, K Rickards, I Bobevski, and A Ooi. Passive acoustic determination of wave-breaking events and their severity across the spectrum. *Journal of Atmospheric and Oceanic Technology*, 23(4):599–618, 2006.

WR McGillis, JB Edson, JE Hare, and CW Fairall. Direct covariance air-sea co2 fluxes. *Journal of geophysical research: Oceans*, 106(C8):16729–16745, 2001.

WR McGillis, JB Edson, CJ Zappa, JD Ware, SP McKenna, EA Terray, JE Hare, CW Fairall, W Drennan, M Donelan, et al. Air-sea co2 exchange in the equatorial pacific. *Journal of Geophysical Research: Oceans*, 109(C8), 2004.

WK Melville. The role of surface-wave breaking in air-sea interaction. *Annual review of fluid mechanics*, 28(1):279–321, 1996.

L Memery and L Merlivat. Modelling of gas flux through bubbles at the air-water interface. *Tellus B: Chemical and Physical Meteorology*, 37(4-5):272–285, 1985.

CJ Merchant, O Embury, CE Bulgin, T Block, GK Corlett, E Fiedler, SA Good, J Mittaz, NA Rayner, D Berry, et al. Satellite-based time-series of sea-surface temperature since 1981 for climate applications. *Scientific data*, 6(1):1–18, 2019.

SD Miller, C Marandino, and ES Saltzman. Ship-based measurement of air-sea co2 exchange by eddy covariance. *Journal of Geophysical Research: Atmospheres*, 115(D2), 2010.

EC Monahan and MC Spillane. The role of oceanic whitecaps in air-sea gas exchange. In *Gas transfer at water surfaces*, pages 495–503. Springer, 1984.

PD Nightingale, G Malin, CS Law, AJ Watson, PS Liss, MI Liddicoat, J Boutin, and RC Upstill-Goddard. In situ evaluation of air-sea gas exchange parameterizations using novel conservative and volatile tracers. *Global Biogeochemical Cycles*, 14(1):373–387, 2000.

FJ Ocampo-Torres, MA Donelan, N Merzi, and F Jia. Laboratory measurements of mass transfer of carbon dioxide and water vapour for smooth and rough flow conditions. *Tellus B: Chemical and Physical Meteorology*, 46(1):16–32, 1994.

RK Pachauri, MR Allen, VR Barros, J Broome, W Cramer, R Christ, JA Church, L Clarke, Q Dahe, P Dasgupta, et al. *Climate change 2014: synthesis report. Contribution of Working Groups I, II and III to the fifth assessment report of the Intergovernmental Panel on Climate Change*. Ipcc, 2014.

D Pierrot, C Neill, K Sullivan, R Castle, R Wanninkhof, H Lüger, T Johannessen, A Olsen, RA Feely, and CE Cosca. Recommendations for autonomous underway pco2 measuring systems and data-reduction routines. *Deep Sea Research Part II: Topical Studies in Oceanography*, 56(8-10):512–522, 2009.

J Prytherch, MJ Yelland, RW Pascal, BI Moat, I Skjelvan, and CC Neill. Direct measurements of the co2 flux over the ocean: Development of a novel method. *Geophysical Research Letters*, 37 (3), 2010a.

J Prytherch, MJ Yelland, RW Pascal, BI Moat, I Skjelvan, and MA Srokosz. Open ocean gas transfer velocity derived from long-term direct measurements of the co2 flux. *Geophysical Research Letters*, 37(23), 2010b.

CL Quéré, O Aumont, L Bopp, P Bousquet, P Ciais, R Francey, M Heimann, CD Keeling, RF Keeling, H Kheshgi, et al. Two decades of ocean co2 sink and variability. *Tellus B: Chemical and Physical Meteorology*, 55(2):649–656, 2003.

L Resplandy, RF Keeling, C Rödenbeck, BB Stephens, S Khatiwala, KB Rodgers, MC Long, L Bopp, and PP Tans. Revision of global carbon fluxes based on a reassessment of oceanic and riverine carbon transport. *Nature Geoscience*, 11(7):504–509, 2018.

T Rhee, PD Nightingale, DK Woolf, G Caulliez, P Bowyer, and MO Andreae. Influence of energetic wind and waves on gas transfer in a large wind–wave tunnel facility. *Journal of Geophysical Research: Oceans*, 112(C5), 2007.

K Riahi, DP Van Vuuren, E Kriegler, J Edmonds, BC O'neill, S Fujimori, N Bauer, K Calvin, R Dellink, O Fricko, et al. The shared socioeconomic pathways and their energy, land use, and greenhouse gas emissions implications: an overview. *Global Environmental Change*, 42: 153–168, 2017.

C Rödenbeck, DCE Bakker, N Metzl, A Olsen, C Sabine, N Cassar, F Reum, RF Keeling, and M Heimann. Interannual sea–air co2 flux variability from an observation-driven ocean mixed-layer scheme. *Biogeosciences*, 11:4599–4613, 2014.

CL Sabine, RA Feely, N Gruber, RM Key, K Lee, JL Bullister, R Wanninkhof, CSl Wong, DWR Wallace, B Tilbrook, et al. The oceanic sink for anthropogenic co2. *science*, 305(5682):367–371, 2004.

R Sander. Compilation of henry's law constants (version 4.0) for water as solvent. *Atmospheric Chemistry & Physics*, 15(8), 2015.

JL Sarmiento and ET Sundquist. Revised budget for the oceanic uptake of anthropogenic carbon dioxide. *Nature*, 356(6370):589–593, 1992.

U Schuster and AJ Watson. A variable and decreasing sink for atmospheric co2 in the north atlantic. *Journal of Geophysical Research: Oceans*, 112(C11), 2007.

U Schuster, A Hannides, L Mintrop, and A Körtzinger. Sensors and instruments for oceanic dissolved carbon measurements. *Ocean Science*, 5:547–558, 2009.

MH Sharqawy, JH Lienhard, and SM Zubair. Thermophysical properties of seawater: a review of existing correlations and data. *Desalination and water treatment*, 16(1-3):354–380, 2010.

DE Slauenwhite and BD Johnson. Bubble shattering: Differences in bubble formation in fresh water and seawater. *Journal of Geophysical Research: Oceans*, 104(C2):3265–3275, 1999.

AV Soloviev and P Schlüssel. Parameterization of the cool skin of the ocean and of the air-ocean gas transfer on the basis of modeling surface renewal. *Journal of Physical Oceanography*, 24 (6):1339–1346, 1994.

ZY Song, Y Bao, Q Shu, YJ Song, XD Yang, and FL Qiao. Simulated long-term monthly ocean surface waves parameters from fio-esm v2.0 cmip6 experiments for past, present, and future climate research, Mar 2020. URL `https://figshare.com/collections/Simulated_long-term_monthly_ocean_surface_waves_parameters_from_FIO-ESM_v2_0_CMIP6_experiments_for_past_present_and_future_climate_research/4819503/1`.

RHR Stanley, WJ Jenkins, DE Lott, and SC Doney. Noble gas constraints on air-sea gas exchange and bubble fluxes. *Journal of Geophysical Research: Oceans*, 114(C11), 2009.

C Sweeney, E Gloor, AR Jacobson, RM Key, G McKinley, JL Sarmiento, and R Wanninkhof. Constraining global air-sea gas exchange for co2 with recent bomb 14c measurements. *Global Biogeochemical Cycles*, 21(2), 2007.

T Takahashi, J Olafsson, JG Goddard, DW Chipman, and SC Sutherland. Seasonal variation of co2 and nutrients in the high-latitude surface oceans: A comparative study. *Global Biogeochemical Cycles*, 7(4):843–878, 1993.

T Takahashi, SC Sutherland, R Wanninkhof, C Sweeney, RA Feely, DW Chipman, B Hales, G Friederich, F Chavez, C Sabine, et al. Climatological mean and decadal change in surface ocean pco 2, and net sea–air co 2 flux over the global oceans. *Deep Sea Research Part II: Topical Studies in Oceanography*, 56(8):554–577, 2009.

T Takahashi, SC Sutherland, and A Kozyr. Global ocean surface water partial pressure of co2 database: Measurements performed during 1957–2018 (version 2018). 2019.

J Thomson, MS Schwendeman, SF Zippel, S Moghimi, J Gemmrich, and WE Rogers. Wave-breaking turbulence in the ocean surface layer. *Journal of Physical Oceanography*, 46(6):1857–1870, 2016.

A Toffoli, A Babanin, M Onorato, and T Waseda. Maximum steepness of oceanic waves: Field and laboratory experiments. *Geophysical Research Letters*, 37(5), 2010.

T Tokoro, H Kayanne, A Watanabe, K Nadaoka, H Tamura, K Nozaki, K Kato, and A Negishi. High gas-transfer velocity in coastal regions with high energy-dissipation rates. *Journal of Geophysical Research: Oceans*, 113(C11), 2008.

W Tsai and KK Liu. An assessment of the effect of sea surface surfactant on global atmosphere-ocean co2 flux. *Journal of Geophysical Research: Oceans*, 108(C4), 2003.

MP Tulin and T Waseda. Laboratory observations of wave group evolution, including breaking effects. *Journal of Fluid Mechanics*, 378:197–232, 1999a.

D Turk, CJ Zappa, CS Meinen, JR Christian, DT Ho, AG Dickson, and WR McGillis. Rain impacts on co2 exchange in the western equatorial pacific ocean. *Geophysical Research Letters*, 37(23), 2010.

R Wanninkhof. Relationship between wind speed and gas exchange over the ocean. *Journal of Geophysical Research: Oceans*, 97(C5):7373–7382, 1992.

R Wanninkhof and WR McGillis. A cubic relationship between air-sea co2 exchange and wind speed. *Geophysical Research Letters*, 26(13):1889–1892, 1999.

R Wanninkhof, JR Ledwell, and WS Broecker. Gas exchange-wind speed relation measured with sulfur hexafluoride on a lake. *Science*, 227:1224–1227, 1985.

R Wanninkhof, W Asher, and E Monahan. The influence of bubbles on air–water gas exchange: Results from gas transfer experiments during wabex-93. In *Selected Papers from the Third International Symposium on Air–Water Gas Transfer*, pages 239–253, 1995.

R Wanninkhof, WE Asher, DT Ho, C Sweeney, and WR McGillis. Advances in quantifying air-sea gas exchange and environmental forcing. 2009.

R Wanninkhof, GH Park, T Takahashi, RA Feely, JL Bullister, and SC Doney. Changes in deep-water co2 concentrations over the last several decades determined from discrete pco2measurements. *Deep Sea Research Part I: Oceanographic Research Papers*, 74:48–63, 2013.

T Waseda and MP Tulin. Experimental study of the stability of deep-water wave trains including wind effects. *Journal of Fluid Mechanics*, 401:55–84, 1999b.

AJ Watson, RC Upstill-Goddard, and PS Liss. Air–sea gas exchange in rough and stormy seas measured by a dual-tracer technique. *Nature*, 349(6305):145–147, 1991.

EK Webb, GI Pearman, and R Leuning. Correction of flux measurements for density effects due to heat and water vapour transfer. *Quarterly Journal of the Royal Meteorological Society*, 106 (447):85–100, 1980.

A Weiss, J Kuss, G Peters, and B Schneider. Evaluating transfer velocity-wind speed relationship using a long-term series of direct eddy correlation co 2 flux measurements. *Journal of Marine Systems*, 66(1):130–139, 2007.

RF Weiss. Carbon dioxide in water and seawater: the solubility of a non-ideal gas. *Marine chemistry*, 2(3):203–215, 1974.

DK Woolf. Bubbles and their role in gas exchange. *The sea surface and global change*, 1997.

DK Woolf. Parametrization of gas transfer velocities and sea-state-dependent wave breaking. *Tellus B*, 57(2):87–94, 2005.

DK Woolf and SA Thorpe. Bubbles and the air-sea exchange of gases in near-saturation conditions. *Journal of Marine Research*, 49(3):435–466, 1991.

IR Young. *Wind generated ocean waves*, volume 2. Elsevier, 1999.

IR Young, S Zieger, and AV Babanin. Global trends in wind speed and wave height. *Science*, 332 (6028):451–455, 2011.

VE Zakharov. Stability of periodic waves of finite amplitude on the surface of a deep fluid. *Journal of Applied Mechanics and Technical Physics*, 9(2):190–194, 1968.

CJ Zappa, WE Asher, and AT Jessup. Microscale wave breaking and air-water gas transfer. *Journal of Geophysical Research: Oceans*, 106(C5):9385–9391, 2001.

CJ Zappa, PA Raymond, EA Terray, and WR McGillis. Variation in surface turbulence and the gas transfer velocity over a tidal cycle in a macro-tidal estuary. *Estuaries*, 26(6):1401–1415, 2003.

CJ Zappa, WE Asher, AT Jessup, J Klinke, and SR Long. Microbreaking and the enhancement of air-water transfer velocity. *Journal of Geophysical Research: Oceans*, 109(C8), 2004.

CJ Zappa, WR McGillis, PA Raymond, JB Edson, EJ Hintsa, HJ Zemmelink, JWH Dacey, and DT Ho. Environmental turbulent mixing controls on air-water gas exchange in marine and aquatic systems. *Geophysical Research Letters*, 34(10), 2007.

RE Zeebe and DA Wolf-Gladrow. *CO2 in seawater: equilibrium, kinetics, isotopes*. Number 65. Gulf Professional Publishing, 2001.

HJ Zemmelink, WWC Gieskes, W Klaassen, WJ Beukema, HW de Groot, HJW de Baar, EJ Hintsa, WR McGillis, and JWH Dacey. Relaxed eddy accumulation measurements of the sea-to-air transfer of dimethylsulfide over the northeastern pacific. *Journal of Geophysical Research: Oceans*, 109(C1), 2004.

DL Zhao and L Xie. A practical bi-parameter formula of gas transfer velocity depending on wave states. *Journal of oceanography*, 66(5):663–671, 2010.

DL Zhao, Y Toba, Y Suzuki, and S Komori. Effect of wind waves on air–sea gas exchange: proposal of an overall co2 transfer velocity formula as a function of breaking-wave parameter. *Tellus B*, 55(2):478–487, 2003.

MM Zweng, JR Reagan, D Seidov, TP Boyer, RA Locarnini, HE Garcia, AV Mishonov, OK Baranova, K Weathers, CR Paver, and I Smolyar. World ocean atlas 2018-salinity. 2, 2019.